nature portfolio

https://doi.org/10.1038/s41586-022-05011-6

Supplementary information

Tandem electrocatalytic N_2 fixation via proton-coupled electron transfer

In the format provided by the authors and unedited

Supplementary Information for

Tandem electrocatalytic N_2 fixation via proton-coupled electron transfer

Pablo Garrido-Barros, Joseph Derosa, Matthew J. Chalkley[†] & and Jonas C. Peters*

Division of Chemistry and Chemical Engineering, California Institute of Technology; Pasadena, CA 91125, USA.

[†]Present address: Department of Pharmaceutical Chemistry, University of California, San Francisco, CA, USA

Correspondence to: jpeters@caltech.edu

Table of Contents:

2-4 S1. Electrochemical set-up for CPC experiments

5-6 S2. Kinetic analysis from cyclic voltammetry

7-13 S3. Ammonia quantification

14-16 S4. Electrocatalysis using **W**$(N_2)_2$ under original conditions

17-24 S5. Optimization of N_2RR conditions using **W**$(N_2)_2$

25-35 S6. Control experiments for electrocatalytic N_2RR

36 S7. H_2 quantification

37-38 S8. Post-electrolysis analysis

39-41 S9. Protonation of **W**$(N_2)_2$

42-46 S10. Chemical PCET reactions

47-55 S11. Mechanistic analysis via Cyclic Voltammetry

56-57 S12. Rotating Ring Disk Electrode (RRDE) experiments

58-62 S13. Nature of the PCET step

63-73 S14. Electrochemical analysis of N_2RR catalysts

74-76 S15. References

S1. Methods:

General methods. All manipulations were carried out using standard Schlenk or glovebox techniques under an N_2 or Ar atmosphere as specified. Solvents were deoxygenated and dried by thoroughly sparging with N_2 followed by passage through an activated alumina column in a solvent purification system by SG Water, USA LLC. Subsequently, the solvents were further dried and stored under N_2 atmosphere inside a glove box with molecular sieves obtained from Sigma Aldrich that were activated at 200ºC overnight under vacuum. Non-halogenated solvents were tested with sodium benzophenone ketyl in tetrahydrofuran (THF) in order to confirm the absence of oxygen and water. Deuterated d_6-DMSO solvent (D, 99.9% with a purity of 99.5%) was purchased from Cambridge Isotope Laboratories, Inc., and use as received. Isotope labelled $^{15}N_2$ gas cylinder was purchased from Cambridge Isotope Laboratories, Inc., NLM-363-1-LB, PSO #:21A-0223, Lot #: I-24583/A R0664758.

N_2 gas in a NEXUS glovebox (Vacuum Atmospheres Company) was purified by a Nexus modular purification system. The purity of N_2 gas was assessed via colorimetric, gas chromatography and NMR methods, with regard to NH_3, N_2O, NO_2^- and NO_3^- impurities.

Cobaltocenium hexafluorophosphate ($[Cp_2Co][PF_6]$), triflic acid, ferrocene, silver triflate, tetrabutylammonium tetrafluoroborate ($[TBA][BF_4]$; TBA = tetra-*N*-butylammonium), lithium perchlorate ($[Li][ClO_4]$), tosic acid (TsOH) were all used as purchased from Sigma Aldrich. [Li][OTf] (OTf = trifluoromethanesulfonate) and $[Li][NTf_2]$ (NTf_2 = bis(trifluoromethanesulfonyl)imide) were also obtained from Sigma Aldrich and further dried under vacuum at 100 ºC for 120 h prior use. Tetrabutylammonium hexafluorophosphate ($[TBA][PF_6]$) from Sigma Aldrich was recrystallized from ethanol prior to use. Silver triflate (AgOTf) was purchased from Strem and used without further purification. The absence of any detectable NH_4^+, NO_3^- or NO_2^- impurities in the electrolyte solution coming from either solvent, electrolyte or acid was analyzed by subjecting the solutions to NH_4^+ detection via ^{1}H-NMR spectroscopy and NO_2^-/NO_3^- detection via the Griess method (*vide infra*). Whenever water was specified as solvent, deionized water OmniSolv (Supelco, Sigma Aldich) was used to prepare the solutions.

* Cited literature for the preparation of known inorganic compounds:

$(Cp)Co(Cp^N)$,[1] $[(Cp)Co(Cp^N)][OTf]$,[1] $[(Cp)Co(Cp^{NH})][OTf]_2$,[1] $[(dppe)_2W(N_2)_2]$,[2] $[(dppe)_2W(NNH_2)(OTs)]$,[3] $[(dppe)_2W(N)(N_3)]$,[4] $[(dppe)_2Mo(N_2)_2]$,[5] $[(PPh_2Me)_4Mo(N_2)_2]$,[6] $[Mo(N_2)_2(PNP)]_2(\mu\text{-}N_2)$,[7] $[Mo(I)_3(PNP)]$,[8] $(P_3Si)Os(N_2)$,[9] $[(P_3B)Fe]^+$,[10] $(P_3Si)Fe(N_2)$,[11] $[Na][BAr^F{}_4]$ ($BAr^F{}_4$ = $B(3,5\text{-}(CF_3)_2\text{-}C_6H_3)_4$),[12] and TsOD[13] were synthesized as described previously.

Reagents for the Griess method for NO_2^- quantification were purchased from Sigma Aldrich and include: sulphanilamide, HCl solution (32 wt.%), and N-1-naphthylenthylenediamine dihydrochloride. Two solutions where prepared for the colorimetric method according to the literature procedure[14]: the first one containing 0.1 g of sulphanilamide in 1 mL HCl solution, adjusting the final volume to 10 mL with deionized water; the second contains 10 mg of N-1-naphthylenthylenediamine dihydrochloride in 10 mL of deionized water. Both solutions were stored in amber bottle and refrigerated. For NO_3^- quantification, a solution containing 0.02 wt.% VCl_3 in 6 M HCl was also employed to quantitatively reduce NO_3^- to NO_2^-.

^{1}H-NMR spectra were recorded with a Varian 400 MHz spectrometer and chemical shifts are reported in ppm relative to tetramethylsilane, using ^{1}H resonances from residual solvent as internal standards. ^{31}P NMR spectra were also recorded with Varian 400 MHz and referenced to the H_3PO_4 signal. For detection of NH_4^+, 1,3,5-trimethoxybenzene was employed as an internal standard, purchased from Sigma Aldrich and used as received; a solution of 8 M H_2SO_4 (98%, Thermo Fischer Scientific) in d_6-DMSO was employed to control the final pH of the NMR sample.[15]

UV-vis measurements were taken on a Cary 50 UV-visible spectrophotometer using a 1 cm quartz cell sealed with a Teflon stopcock.

Gas chromatography coupled to a thermal conductivity detector (GC-TCD) was performed in the Environmental Analysis Center (Caltech) using a HP 5890 Series II instrument with N_2 as the carrier gas for H_2 detection. A calibration curve was determined by direct injection of known volumes of H_2. GC-TCD was also employed to detect for possible contamination of N_2O in the $^{14}N_2$ and $^{15}N_2$ gas supply, using helium as the carrier gas. Calibration was determined by direct injection of known volumes of N_2O.

X-ray photoelectron spectroscopy was employed for analysis of the BDD working electrode used in the CPC experiments. We used a Kratos AXIS Ultra XPS instrument (Molecular Materials Resource Center, Caltech) with an X-ray source consisting of a monochromatic Al K_α line at 1486.6 eV, with 0.2 eV resolution at the full width half maximum. XPS results were analyzed using CasaXPS, Casa Software Ltd. The XPS instrument was calibrated to the Au $4f_{7/2}$ peak at 84 eV. Samples were calibrated to the adventitious carbon peak at 284.5 eV.

Electrochemistry. A CHI instruments 600B and a Biologic VSP potentiostat were used for all electrochemical data collection.

Cyclic voltammetry (CV) experiments were carried out in a one-compartment three-electrode cell using a boron doped diamond (BDD) disk as the working electrode (3 mm diameter), a Pt disk as the counter electrode, and a Ag/AgOTf (5 mM) reference electrode. Details for the CVs are noted as they appear. For all measurements IR compensation was applied accounting for 85% of the total resistance. The resistance has been estimated using the ZIR functionality of Biologic potentiostats that performs potentiostatic electrochemical impedance spectroscopy at a single high frequency value. All the reported potentials are referenced to the ferrocenium/ferrocene couple ($Fc^{+/0}$) used as an external standard.

Controlled potential electrolyses (CPEs) were carried out in a gas-tight, two-compartment or H-cell equipped with a frit to separate anodic from cathodic chambers (Fig. S1). This cell also features two necks, one in each compartment, sealed using a septum that allows for bubbling of different gasses other than the $^{14}N_2$, such as Argon and $^{15}N_2$, needed in control experiments. Either a BDD plate (dimensions 1x1 cm) or a high surface area reticulated vitreous carbon foam was employed as the working electrode, a Ag/AgOTf (5 mM) as the reference electrode, and a Zn plate as the sacrificial counter electrode. In a typical experiment, 6 mL of solvent containing 0.2-0.1 M of the specified electrolyte and the tosic acid was added to the electrochemical cell, 3 mL per compartment. For experiments including the catalysts, the cathodic chamber was also charged with the corresponding amount of **Co**(III,N)$^+$ mediator and **W**$(N_2)_2$ (or other N_2RR catalyst), or both were taken from concentrated stock solutions (1 mg/mL). The electrochemical cell was assembled inside an N_2 glove box in which the CPC experiment was also performed. The potential applied

during the CPC experiment was set to −1.35 V vs $Fc^{+/0}$ according to the peak current observed for the catalytic wave from previous CVs. The solution was stirred throughout the CPC experiment.

The BDD disk electrode for cyclic voltammetry was polished using a PK-3 polishing kit with 6 µm diamond (Biologic). The BDD plate electrodes were pre-treated according to literature procedures.[16] The Zn counter electrode was polished with a stainless steel sponge, washed repeatedly with water and acetone and vacuum dried. BDD plate electrodes were purchased from IKA (Electrode 0.7 BDD, Ident. No: 00440003932).

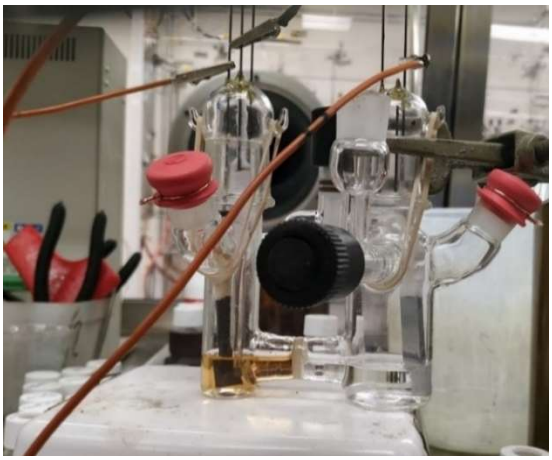

Figure S1. Gas-tight, two-compartment electrochemical cell setup employed in the CPC experiments. It is composed of two Kontes valves, two 14/24 necks closed by septa fastened with copper-wire, and two 24/40 necks for the incorporation of the electrodes that are connected to the potentiostat leads via crossing tungsten wires.

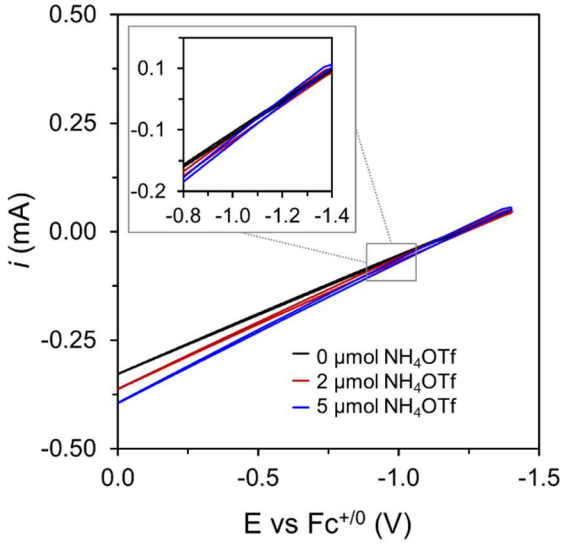

Figure S2. CVs of the Zn electrode employed as sacrificial counter electrode in the CPC experiments in 0.2 M [TBA][BF_4] THF solution containing different concentrations of NH_4OTf and 50 mM TsOH, using a GC plate counter electrode to determine maximum operating current densities.

S2. Kinetic analysis from cyclic voltammetry:

For kinetic analysis via cyclic voltammetry, a multielectron/multiproton electrocatalytic process can be simplified to an EC_{cat} mechanism involving an electrode-mediated electron transfer process (E) coupled to a catalytic chemical reaction (C_{cat}), which will reflect a convolution of the elementary chemical steps of catalysis.[17] For an EC_{cat} process under pure kinetic conditions, an ideal S-shape response would be obtained featuring a current intensity in the catalytic plateau (i_{cat}) described by **Eq. S1**. In this equation, n_e is the number of electrons involved in the catalytic cycle, F is the Faraday constant, S is the area of the electrode, D_{cat} is the diffusion coefficient of the catalyst and k_{obs} is the observed kinetic constant of the catalytic process which will reflect a convolution of the kinetically relevant steps of catalysis and will follow a mathematical expression depending on the rate law. Therefore, the intensity of the catalytic plateau should increase linearly with the concentration of the catalysts, C_{cat}^0, and with the square root of k_{obs} that in turns incorporate the concentration of the substrates involved in the rate determining steps.

$$i_{cat} = n_e F S C_{cat}^0 \sqrt{D_{cat}} \sqrt{k_{obs}} \quad \textbf{(Eq. S1)}$$

In the present case of tandem catalysis, each of the coupled catalytic cycles (PCET and N_2RR) will provide a catalytic current according to **Eq. S1** that will depend on their specific mechanism. The multielectron/multiproton character of this overall process and the interplay between both catalytic cycles complicate obtaining an exact analytical solution, and the overall observed current will be a convolution of the current for each of the catalytic cycles.

For a proposed mechanism where the mediator reduces certain intermediates of the N_2RR cycle via a rate determining PCET, with the rest of electron transfers happening at the electrode, the expression for the catalytic current due to PCET is going to depend linearly on the concentration of the mediator ([Co]) and on the square root of the **W** catalyst concentration ([W]), **Eq. S3**. At the same time, the catalytic current associated to the N_2RR cycle, assuming that the intermediates can be reduced by the PCET mediator or directly at the electrode followed by further protonation TsOH in solution, the observed catalytic current will increase linearly with [W] and with $k_{obs}(N_2RR)^{1/2}$, **Eq. S4**, which in turn will have a positive dependence on [Co] due to a rate limiting PCET, and possibly on [TsOH], according to the relative rate of protonation steps, **Eq. S5**.

$$i_{obs} = i_{cat}(PCET) + i_{cat}(N_2RR) \quad \textbf{(Eq. S2)}$$

$$i_{cat}(CPET) = FS[Co]\sqrt{D_{Co}} \sqrt{k_{PCET}[W]} \quad \textbf{(Eq. S3)}$$

$$i_{cat}(N_2RR) = n_e F S[W]\sqrt{D_{Co}} \sqrt{k_{obs}(N_2RR)} \quad \textbf{(Eq. S4)}$$

$$k_{obs}(N_2RR) = f([Co], [TsOH]) \quad \textbf{(Eq. S5)}$$

In order to obtain preliminary information about the rate law for the tandem catalytic process and support our proposals, we have examined how changes in the concentration of the different components affect the behavior of the i_{cat} during CV experiments. Herein, we are evaluating i_{cat} as the maximum current of the electrocatalytic wave obtained from background-corrected CVs as its behavior approached the S-shape expected from an ideal electrocatalytic response in the pure kinetic regime (*vide infra*).

The kinetic isotope effect, *KIE*, can be determined by evaluating k_{obs} for the reaction in the presence of protio-acid, TsOH, and deutero-acid, TsOD and comparing them as in **Eq. S6**. As aforementioned, the complications in obtaining the mathematical expression for this tandem electrocatalytic system preclude calculation of meaningful k_{obs} values. However, as deduced from **Eq. S1**, i_{cat} is proportional to the square root of k_{obs} for a simplified EC_{cat} mechanism describing our more complex system, so we have estimated a value for *KIE* from the ratio between the i_{cat} values observed in the presence of each acid.

$$KIE = \frac{k_{obs}\,(\,^{1}H)}{k_{obs}\,(\,^{2}H)} = \frac{[i_{cat}\,(\,^{1}H)]^{2}}{[i_{cat}\,(\,^{2}H)]^{2}} \qquad \textbf{(Eq. S6)}$$

S3. Ammonia quantification via ^{1}H-NMR

S3.1 ^{1}H-NMR quantification:

Upon completion of CPC experiments, excess of acid (twice as much as the theoretical amount of ammonia produced) was added through the septum with a syringe in order to quench all possible free ammonia in solution as NH_4^+. Subsequently, the cell was place in a cold well at −78 ºC using a dry ice/acetone bath in order to condense possible evaporated ammonia in the headspace. After 10 min at this temperature, the electrochemical cell was brought to room temperature and allowed to stir for another 10 min in the presence of the excess acid. The solution was then transferred with a pipette into a Schlenk tube; the cell was subsequently washed with more solvent that was also collected into the same tube. The tube was tightly sealed with a Kontes cap, brought out of the glove box and placed into liquid N_2 allowing 10 min for the entire solution to freeze. Once frozen, the Schlenk tube was opened and 2 equivalents of sodium *tert*-butoxide (NaO^tBu) base per mol of total acid (initial acid loading plus quenching acid) were slowly delivered in the form a 0.25 M MeOH solution, leaving 5 min at liquid nitrogen temperature for equilibration. Afterwards, the headspace of the tube was evacuated to constant pressure and the tube was closed and brought to room temperature, stirring for 10 min to react all the NH_4^+ with the added base to liberate NH_3. At the same time, in a different tube, 2 mL of a 2.0 M HCl solution in diethyl ether was prepared. In the next step the NH_3 solution was vacuum transferred to the ethereal HCl solution to remove non-volatile components of the reaction mixture, including the catalysts, the electrolyte, the resulting sodium tosylate (NaOTs) and the excess of NaO^tBu. The resultant solution (NH_3 and ethereal HCl) was allowed to react for 10 min at room temperature and then evaporated to dryness, affording NH_4Cl.

Sample preparation for quantification via ^{1}H-NMR methods involves extracting the solid NH_4Cl after work up with 0.5 mL of 1 mM TMB in d_6-DMSO. To this solution, 10 μL of 8 M H_2SO_4 solution in d_6-DMSO were added (0.2 M final concentration) to ensure constant acidic conditions of the resulting sample and minimize variations due to different proton activities of the resulting sample.[15,18] Analysis of the total amount of NH_3 produced after isolation via vacuum transfer overcomes some of the challenges associated with low ammonia concentrations or interferences of the electrolyte solution in the quantification methods when direct sampling from the electrolyte solution is employed for the analysis.[19] Moreover, the amounts of NH_3 produced in the present work are well above those of background levels (section S6). Nonetheless, appropriate control experiments have been carried out in order to verify the source of the generated NH_3 as a result of electrocatalytic N_2RR (section S6).

Despite its high selectivity for NH_4^+ detection, ^{1}H-NMR spectroscopy has proven to be challenging for accurate quantification due to the interplay between d1, T1 and the proton exchange-induced loss of coherence in determining the intensity of the NMR peak, and their different response to changes in the sample concentration and proton concentration.[15] This can cause absolute, quantitative NMR (qNMR), based on direct integration with respect to an internal standard with a known concentration, frequently result in over- or underestimation of the total NH_4^+.[18] Therefore, ^{1}H-NMR analysis of NH_4^+ via relative quantification using a calibration curve and an internal standard is preferred as a reliable method for fast determination.

We have employed this method using TMB as an internal standard. In order to obtain a calibration curve, a stock solution of NH_4Cl (1mg/mL) in 1 mM TMB in d_6-DMSO solution was prepared. From that stock solution, different volume aliquots were diluted with the same 1 mM TMB in d_6-DMSO solution up to a total volume of 0.5 mL, resulting in standard samples with differing concentrations of NH_4Cl. To each of those solutions, 10 µL of 8 M H_2SO_4 in d_6-DMSO were added to obtain a constant and controlled proton concentration in the final sample, preventing possible errors in the calibration associated with different degrees of acidity in different samples. ^{1}H-NMR spectra of these standard samples afforded the calibration curve via integration of the 4 protons of the NH_4^+ peak (N_{NH4+}) in the range 7.3-6.9 ppm relative to the 3 aryl protons of TMB (N_{TMB}) at around 6.1 ppm according to **Eq. S7**, where I, C, and N are the integral, concentration and number of protons respectively for each component.

$$C_{NH_4^+} = \frac{I_{NH_4^+} N_{TMB}}{I_{TMB} N_{NH_4^+}} C_{TMB} \quad \textbf{(Eq. S7)}$$

^{1}H-NMR spectra obtained from the standard samples are shown in Figure S3 and S5 and resulting calibration plots are shown in Figure S4 and S6. Two calibration plots were prepared using two different concentrations of internal standard (TMB) of 1 mM and 5 mM respectively. A similar procedure was followed to prepare the calibration plot for $^{15}NH_4^+$ used in the $^{15}N_2$ labelled experiments, and the results are shown in Figure S7 and S8. In both cases, a reliable linear fit was obtained with $R^2 > 0.99$.

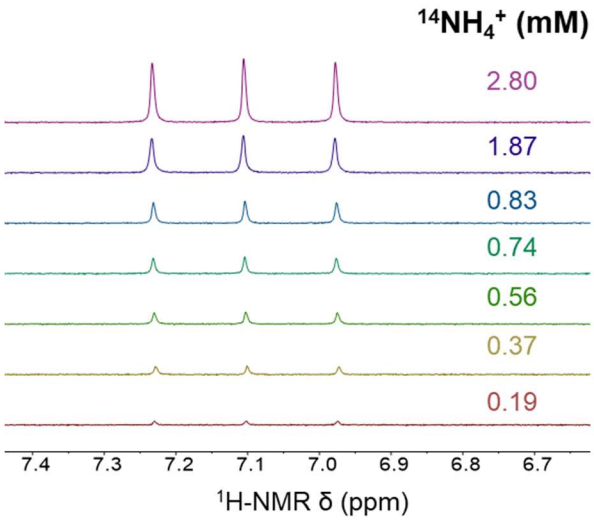

Figure S3. ^{1}H-NMR spectra of standard samples containing different concentrations of NH_4Cl in 1mM TMB d_6-DMSO solution.

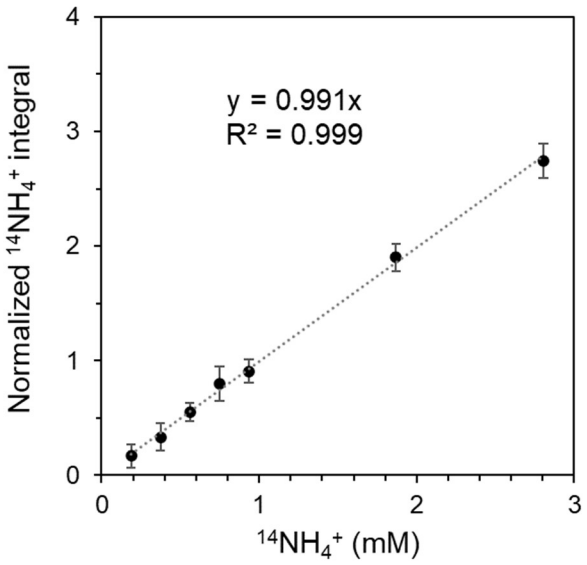

Figure S4. Calibration curve according to **Eq. S7** for the ^{1}H-NMR spectra of standard $^{14}NH_4Cl$ samples presented in Figure S3. The normalized integral was obtained by integration of the triplet in the 7.3-6.9 ppm region corresponding to the 4 protons of $^{14}NH_4^+$ relative to the integration of the singlet at 6.1 ppm corresponding to the 3 aryl protons of TMB (1 mM concentration). For each concentration point, an average of 3 independent measurements is shown together with the error bars.

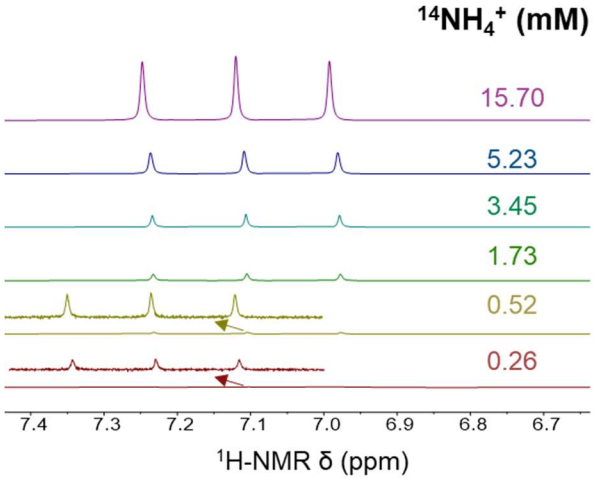

Figure S5. ^{1}H-NMR spectra of standard samples containing different concentrations of NH_4Cl in 5mM TMB d_6-DMSO solution. For the spectra of 0.52 and 0.26 mM NH_4Cl, a magnification of the NH_4^+ peaks is included.

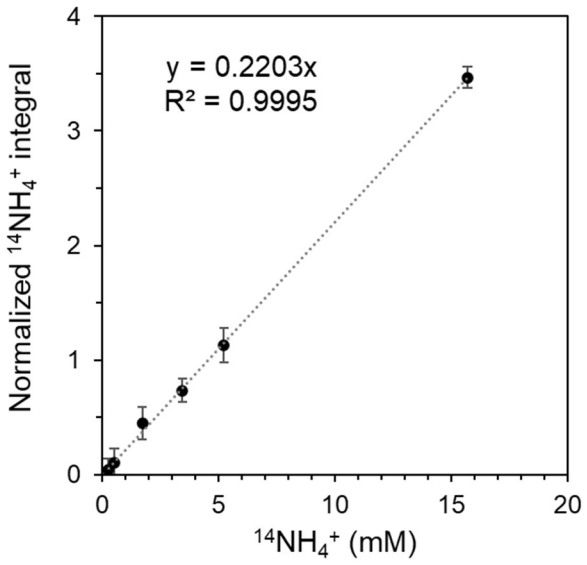

Figure S6. Calibration curve according to **Eq. S7** for the ^{1}H-NMR spectra of standard $^{14}NH_4Cl$ samples presented in Figure S5. The normalized integral was obtained by integration of the triplet in the 7.3-6.9 ppm region corresponding to the 4 protons of $^{14}NH_4^+$ relative to the integration of the singlet at 6.1 ppm corresponding to 3 aryl protons of TMB (5 mM concentration). For each concentration point, an average of 3 independent measurements is shown together with the error bars.

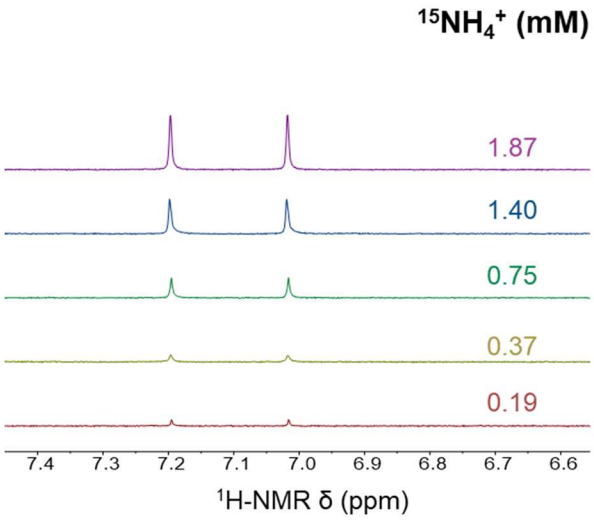

Figure S7. ^{1}H-NMR spectra of standard samples containing different concentrations of $^{15}NH_4Cl$ in 1mM TMB d_6-DMSO solution.

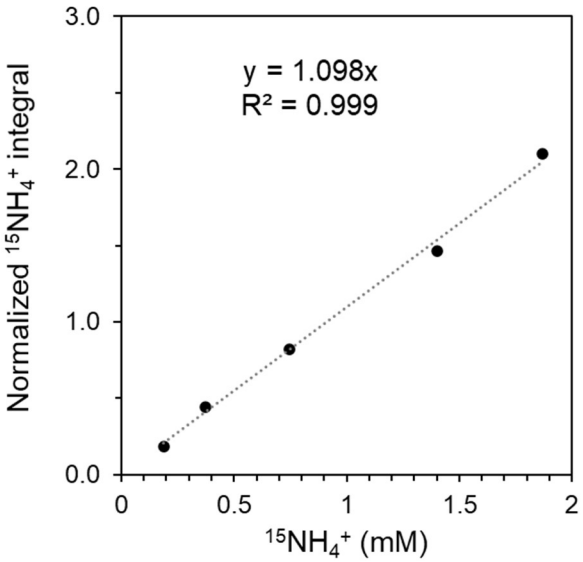

Figure S8. Calibration curve according to **Eq. S7** for the ^{1}H-NMR spectra of standard $^{15}NH_4Cl$ samples presented in Figure S7. The normalized integral was obtained by integration of the doublet in the 7.3-6.9 ppm region corresponding to the 4 protons of $^{15}NH_4^+$ relative to the integration of the singlet at 6.1 ppm corresponding to 3 aryl protons of TMB (1 mM concentration).

Several methodologies have also been reported to minimize issues associated with absolute NH_4^+ quantification via an internal standard, which consider variables from sample preparation to internal standard selection and specific ^{1}H-NMR sequences in order to improve the accuracy and detection limit. One promising approach is based on selective excitation of protons from the NH_4^+, as reported by Jaramillo and coworkers.[19] They employ the Frequency-Selective pulse Gradient Spin Echo (selgspe) sequence that selectively excite the protons with NMR signals in a small region centered where the NH_4^+ appear (~7.1 ppm). While this method still involves longer acquisition times than the NMR method described previously based on calibration plots, it minimizes the proton solvent signals as one of the primary challenges for NH_4^+ detection and generates strong NH_4^+ signals, thereby providing one of the highest sensitivities for quantitation. The concentration of NH_4Cl was determined by integration of the area below the NH_4^+ peaks compared to that of the internal standard. We employed TMB which is compatible for quantification via both previous calibration plots and this selective excitation method as shown in Figure S9 due to the proximity of the three aryl peaks of TMB to the NH_4^+ region. Calculation of the concentration of standard samples of NH_4Cl was performed by both direct quantitative integrations relative to the internal standard (Figure S11) and by generation of a calibration plot (Figure S10). As evidenced by the results, this method offers a means for both absolute quantification via direct comparison to the internal standard peak added in known concentration and quantification by the use of the calibration curve. Results from application of this method were consistent with those obtained from the previous approach.

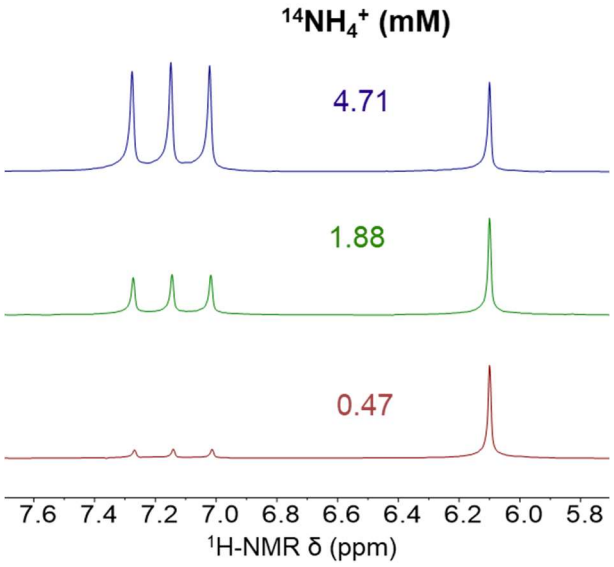

Figure S9. ^{1}H-NMR spectra of standard samples containing different concentrations of NH_4Cl in 1mM TMB d_6-DMSO solutions using Frequency-Selective pulse Gradient Spin Echo.

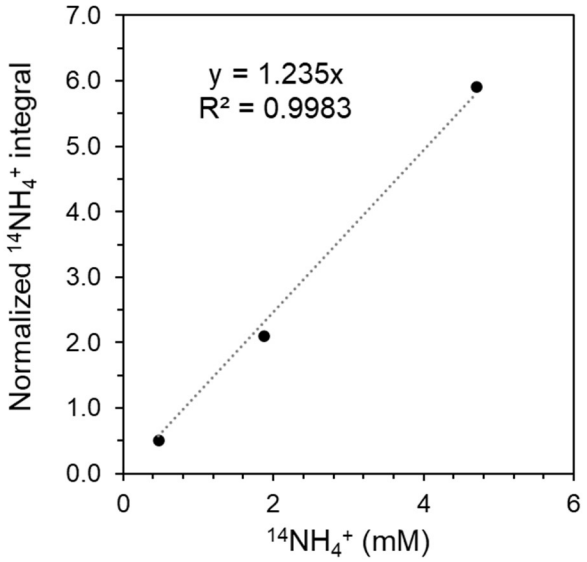

Figure S10. Calibration curve according to **Eq. S7** for the ^{1}H-NMR spectra of standard $^{14}NH_4Cl$ samples presented in Figure S9. The normalized integral was obtained by integration of the triplet in the 7.3-6.9 ppm region corresponding to the 4 protons of $^{14}NH_4^+$ relative to the integration of the singlet at 6.1 ppm corresponding to 3 aryl protons of TMB (1 mM concentration).

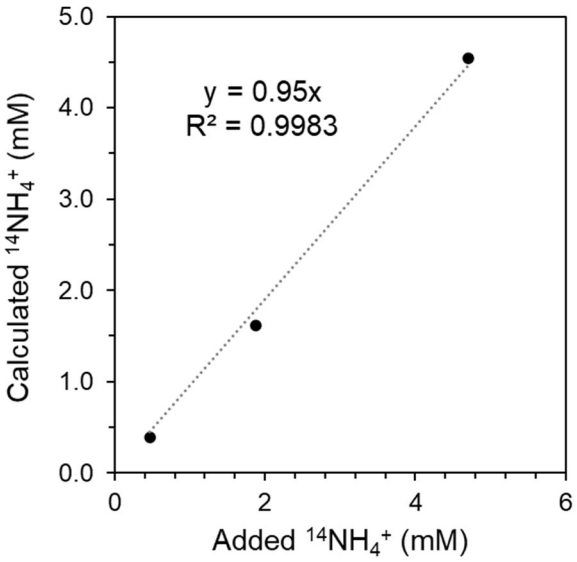

Figure S11. Plot of the calculated NH_4^+ amount via absolute quantification with internal standard versus the amount of NH_4Cl added to the sample. The high correlation with $R^2 > 0.99$ reflects the adequacy of this method for direct quantitative NMR determination of NH_4^+.

S3.2 Faradaic Efficiency:

The Faradaic efficiency (FE) was calculated considering the total charge passed during the CPC experiments (Q), the number of electrons involved in the formation of one molecule of NH_3 ($n_e = 3$), the Faraday constant (F) and the mols of NH_3 produced (N_{NH3}), following **Eq. 8**:

$$FE = \frac{N_{NH}}{\frac{Q}{n_e F}} \qquad \textbf{(Eq. 8)}$$

S4. Electrocatalysis using $W(N_2)_2$ under original conditions

As reported by Becker and coworkers,[5] previous attempted experiments to render the **W**$(N_2)_2$ system electrocatalytic for N_2RR by CPC in the presence of acid employed glassy carbon as a working electrode, among other electrodes, THF as solvent, [TBA][BF_4] as electrolyte (TBA = tetra-*N*-butylammonium) and tosic acid (TsOH) as proton source. We performed control electrocatalytic experiments using related conditions so as to compare results from the tandem PCET-N_2RR approach presented in this work, with these previous approaches.

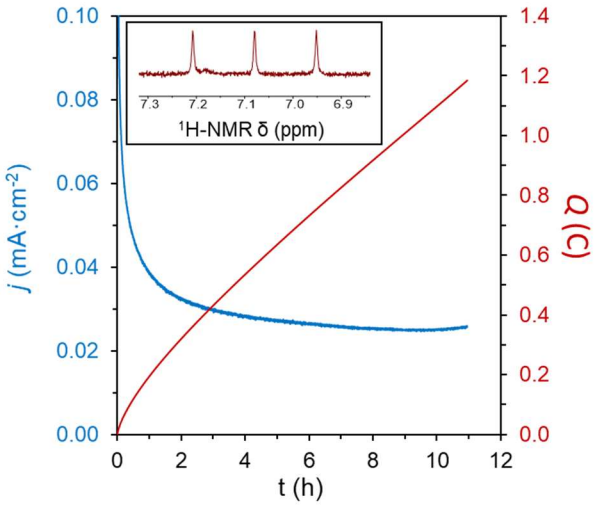

Figure S12. Current and charge profile for a CPC at −1.35 V vs $Fc^{+/0}$ in 0.2 M [TBA][BF_4] THF solution containing 0.05 mM **Co**(III,N)$^+$, 0.05 mM **W**$(N_2)_2$ and 5 mM TsOH, using a GC plate working electrode. **Inset**: Quantification of generated NH_3 via ^{1}H-NMR spectroscopy.

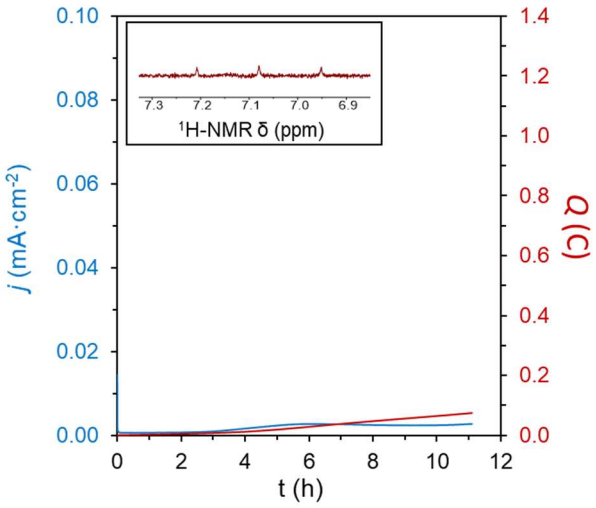

Figure S13. Current and charge profile for a CPC at −1.35 V vs $Fc^{+/0}$ in 0.2 M [TBA][BF_4] THF solution containing 0.05 mM **W**$(N_2)_2$ and 5 mM TsOH, using a GC plate working electrode. **Inset**: Quantification of generated NH_3 via ^{1}H-NMR spectroscopy.

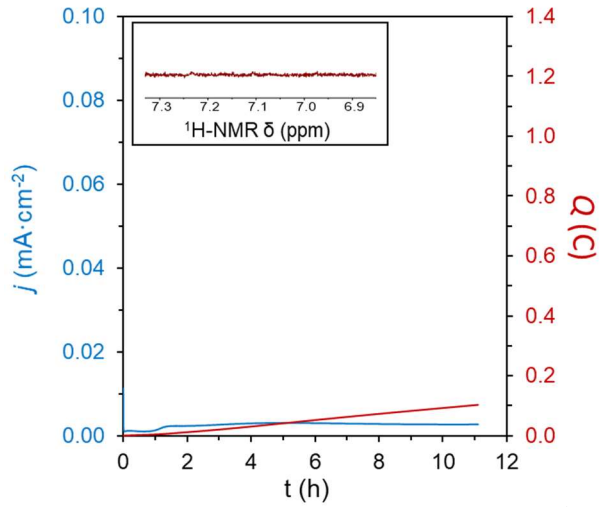

Figure S14. Current and charge profile for a CPC at −1.35 V vs $Fc^{+/0}$ in 0.2 M [TBA][BF_4] THF solution containing and 5 mM TsOH, using a GC plate working electrode. **Inset**: Quantification of generated NH_3 via ^{1}H-NMR spectroscopy.

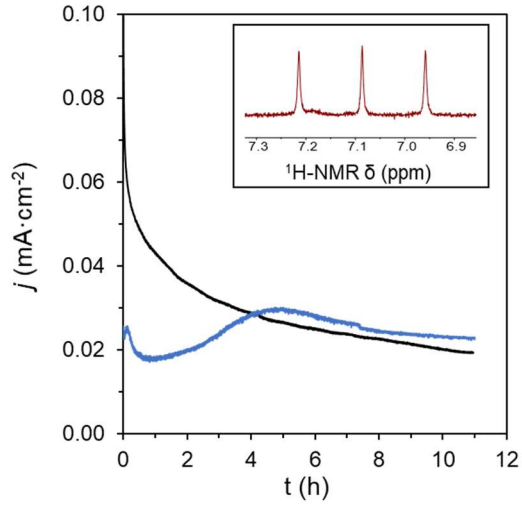

Figure S15. Current and charge profile for two consecutive CPC at −1.35 V vs $Fc^{+/0}$ in 0.2 M [TBA][BF_4] THF solution containing initially 0.05 mM **Co**(III,N)$^+$, 0.05 mM **W**(N_2)$_2$ and 5 mM TsOH, using a GC plate working electrode. After the first CPC (black trace), an extra 100 equiv of TsOH were added through a septum as a concentrated THF solution, and the second CPC was initiated (blue trace). **Inset**: Quantification of generated NH_3 via ^{1}H-NMR spectroscopy.

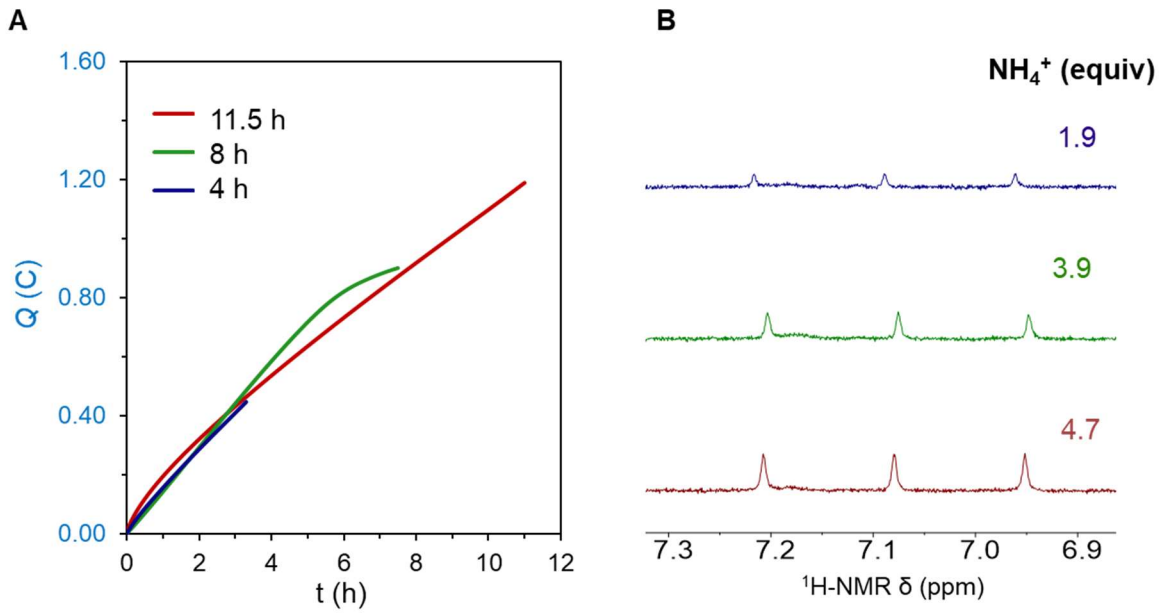

Figure S16. (**A**) Charge profile for three different CPCs at −1.35 V vs $Fc^{+/0}$ in 0.2 M [TBA][BF_4] THF solution containing 0.05 mM **Co**(III,N)$^+$, 0.05 mM **W**(N_2)$_2$ and 5 mM TsOH, using a GC plate working electrode. The three CPC experiments were stopped at different times to confirm that the produced NH_3 is coming from the electrocatalytic process. (**B**) Quantification of generated NH_3 via ^{1}H-NMR spectroscopy.

S5. Optimization of N_2RR conditions using $W(N_2)_2$:

Following initial confirmation of N_2RR by our tandem approach using conditions originally employed in previous reports by Becker and coworkers,[5] we canvassed different conditions to optimize the production of ammonia. These conditions included the use of different working electrodes, acid concentrations, electrolytes, solvent, and surface areas for the working electrode, as they may influence in electrocatalytic processes in general, and in previous attempts to electrochemical and chemical N_2RR by W and Mo complexes in particular.

Working electrode: GC electrode was initially employed by Becker and coworkers in their electrochemical studies of $\mathbf{W}(N_2)_2$ system.[5] However, as previously explored by our group, BDD can attenuate the background hydrogen evolution reaction at the surface of the electrode in the presence of TsOH. This is shown in Figure S17, where CV of both electrodes in the presence of acid are plotted, obtaining comparatively higher background currents with GC. Consistently higher equiv of NH_3 and Faradaic efficiencies were obtained when BDD was used in the CPC experiments compared to GC (entry 1 and 2 in Table S1).

Acid concentration: The acid concentration has a direct influence on background electrocatalytic HER at the electrode, as shown in Figure S18. As demonstrated by entry 2-5 in Table S1, increasing the acid concentration increases the total production of ammonia, as expected from a higher availability of H^+, but the Faradaic efficiency drops as a consequence of the relative rate of background HER, increasing more than the rate of N_2RR.

Electrolyte: Initial studies toward electrocatalytic N_2RR using $\mathbf{W}(N_2)_2$ and analogous $\mathbf{Mo}(N_2)_2$ species employed [TBA][BF_4] electrolyte. However, it has been shown that protonation of $\mathbf{W}(N_2)_2$ using HBF_4 generates the corresponding (F)$\mathbf{W}(NNH_2)_2$ hydrazido complex due to abstraction of a F^- anion; this species requires a very strong cathodic potential to reduce it and features slow F^- dissociation required to proceed in the N_2RR cycle;[5,20] under our catalytic conditions with [TBA][BF_4] and TsOH, this species is also formed (Figure S19). Moreover, $M(X)(N_2)$ species (X = Cl^-, I^-) can further disproportionate to form the decomposition product $\mathbf{M}(X)_2$ whose reduction to initial $M(N_2)_2$ requires a strongly reducing potential.[21] Therefore, we have explored other electrolytes featuring weak coordinating anions to prevent those issues. Furthermore, we have considered the Li^+ salts of those anions as they generally feature high conductivity, and the use of Lewis acids has been shown to have favorable effect in the further activation of N_2RR intermediates.[22] One of the electrolytes fulfilling both aspects, also employed in the initial work by Pickett and coworkers, is [Li][ClO_4], featuring a very high conductivity and with a ClO_4^- anion that is very weakly coordinating. However, it is also known that ClO_4^- can lead to the oxidation of reduced W and Mo complexes resulting in the formation of off cycle, oxo species that provides one possible explanation for catalyst degradation in the presence of acid. This possibility is supported under our conditions in the presence of tosic acid by ^{31}P-NMR and UV-vis (Fig S20 and S21).[23] Therefore, we studied electrolytes based on non-coordinating and chemically inert anions such as OTf^-, NTf_2^- and $BAr^F{}_4^-$. In the case of [Li][OTf], the resulting conductivity of the electrolyte solution is very low, potentially due to formation of ion pairs in solutions that prevent ionic conductivity as previously studied.[24] In contrast, [Na][$BAr^F{}_4$] and [Li][NTf_2] lead to highly conductive electrolytes with very similar CV responses of the in situ formed hydrazido species (OTs)$\mathbf{W}(NNH_2)_2$, with redox potentials of around −2.0 V vs $Fc^{+/0}$, 200 mV lower than in

the case of (F)**W**(NNH_2)$_2$ (Figure S22). Our studies showed higher and more efficient production of ammonia using [Na][BAr^F_4] (entry 9 in Table S1), and especially with [Li][NTf_2] (entry 11 in Table S1).

Solvent: Many of our electrochemical and spectroscopic data has been performed in THF due to the predominance of this solvent in previous reports using W and the other catalysts, and its use in various other N_2RR (electro)catalytic systems, providing a means of direct cross-comparison. Moreover, thermodynamic and kinetic data regarding these systems are usually reported in the same solvent. However, we have found that the use of DME provides slightly better yields than THF (e.g., 11.5 vs 10.0 equiv of NH_3 in a direct comparison, entry 11 and 12 in Table S1). We suspect that this is due to unproductive reactions of THF under acidic and reducing conditions in the long CPC experiments.

Catalyst:electrode surface ratio: In order to optimize the electrode/catalyst interphase, minimize the time of CPC, and increase the catalytic current, the use of a high surface area electrode was pursued. We explored the use of GC foam as a high surface area electrode. To minimize the potential consumption of ammonia due to the oxidation process at the counter electrode the concentration of catalyst was further lowered to 0.01 mM, leading to relatively lower catalytic currents. In this case, a higher number of equiv are obtained (entry 16 in Table S1) per catalyst, highlighting the potential benefit of larger electrode/catalyst interfaces, shorter electrolysis times, and lower catalyst concentrations.

Cell set-up: The sacrificial Zn anode was also substituted by a GC electrode, thus performing solvent oxidation as the anodic reaction (entry 17 in Table S1). However, lower yields for ammonia were observed, consistent with its partial oxidation at the GC anode. In order to explore the potential crossover of ammonia through the frit of the two-compartment cell, a known amount of NH_4OTf (1.5 μmol) was dissolved in the electrolyte solution and placed into the working compartment of the electrochemical cell. Fresh electrolyte solution without NH_4OTf was also placed in the counter compartment, and the system was then hermetically sealed and allowed to stir for 5.5 h. After this time, the total NH_4OTf concentration in both the working and the counter compartments was analyzed independently, resulting in 0.72 and 0.35 μmol respectively, indicating that over time some of the ammonia crosses over the frit to the counter compartment where it could be oxidized. Moreover, the difference between the total amount of ammonia quantified (1.07 μmol) versus the initially added (1.5 μmol) is consistent with previous observations that ammonia can strongly adsorb on the cell and/or the frit, leading to underestimation.[25,26] In order to address these challenges, a further experiment was performed using a two-compartment cell with a SELEMION membrane as a separator. SELEMION is an anion exchange membrane that could in principle prevent the pass of cations such as NH_4^+ as well as its significant adsorption. Consistent with this hypothesis, CPC using this set up produced slightly increased yields of ammonia (entry 18 in Table S1). However, the low conductivities, typical from the use of selective ion exchange membranes in organic solvents, results in significantly lower initial current densities of -0.015 mA vs -0.10 mA achieved using a frit separator.

Table S1. Conditions explored for the CPC experiments together with the NH_3 produced and FE.

Entry	Working/Counter Electrode	Solvent	Electrolyte	[W] (mM)	[Co] (mM)	[TsOH] (mM)	NH_3 (equiv/W)	FE (%)
1	GC/Zn	THF	[TBA][BF_4]	0.05	0.05	5.0	4.7	17.8
2	BDD/Zn	THF	[TBA][BF_4]	0.05	0.05	5.0	5.6	20.5
3	BDD/Zn	THF	[TBA][BF_4]	0.05	0.05	2.5	4.6	33.2
4	BDD/Zn	THF	[TBA][BF_4]	0.05	0.05	10.0	6.5	9.4
5	BDD/Zn	THF	[TBA][BF_4]	0.05	0.05	25.0	7.2	5.2
6	BDD/Zn	THF	[TBA][BF_4]	0.05	0.13	5.0	6.7	24.3
7	BDD/Zn	THF	[TBA][BF_4]	0.05	0.25	5.0	7.0	25.5
8	BDD/Zn	THF	[Li][ClO_4]	0.05	0.05	5.0	6.5	23.4
9	BDD/Zn	THF	[Na][$BAr^F{}_4$]	0.05	0.05	5.0	8.7	31.3
10	BDD/Zn	THF	[Li][OTf]	0.05	0.05	5.0	7.3	26.4
11	BDD/Zn	THF	[Li][NTf_2]	0.05	0.05	5.0	10.0	36.3
12	BDD/Zn	DME	[Li][NTf_2]	0.05	0.05	5.0	11.5	45.1
13	BDD/Zn	DME	[Li][NTf_2]	0.05	0.05	10.0	15.3	27.7
14	BDD/Zn	DME	[Li][NTf_2]	0.05	0	5.0	0.8	3.0
15	BDD/Zn	DME	[Li][NTf_2]	0	0.05	5.0	-	-
16	GC foam/Zn	DME	[Li][NTf_2]	0.01	0.01	5.0	39.5	42.9
17	BDD/GC	DME	[Li][NTf_2]	0.05	0.05	5.0	8.1	30.5
18*	BDD/GC	DME	[Li][NTf_2]	0.05	0.05	5.0	12.8	50.6

*A two-compartment cell was employed with a SELEMION membrane separating both compartments.

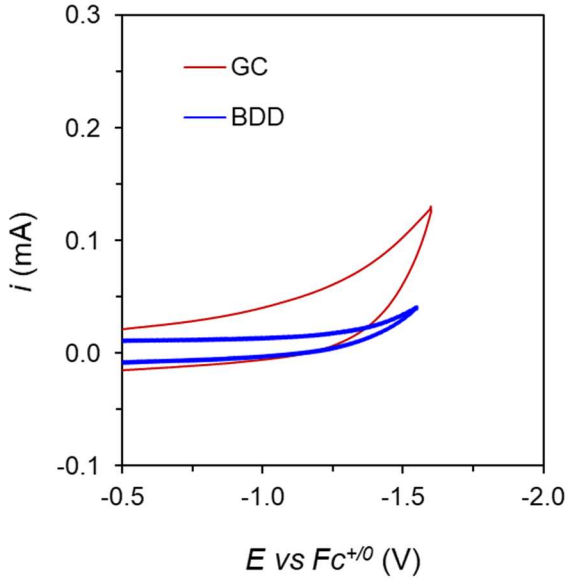

Figure S17. CV at 100 $mV \cdot s^{-1}$ in 0.2 M [TBA][BF_4] THF solution containing and 50 mM TsOH, using either a GC (red) or a BDD (blue) plate working electrode.

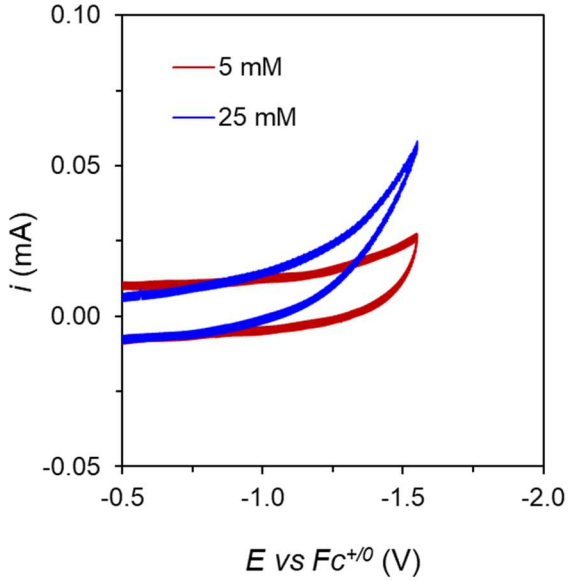

Figure S18. CV at 100 $mV \cdot s^{-1}$ in 0.2 M [TBA][BF_4] THF solution containing different concentrations of TsOH and using a BDD plate working electrode. The increase of current with TsOH concentration reflects an increase in the background HER, which in turn has an influence in the Faradaic efficiency obtained from CPC experiments.

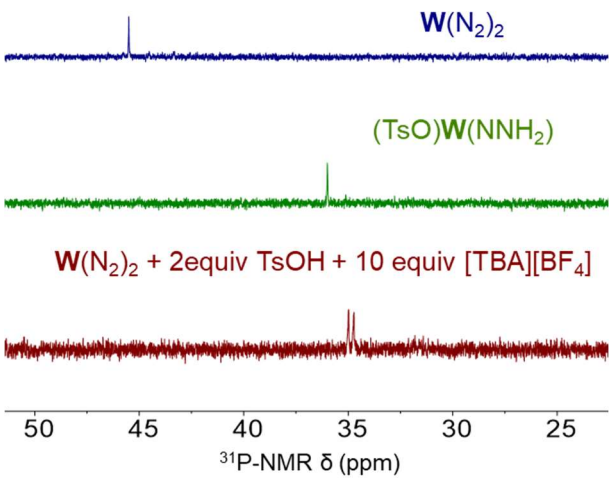

Figure S19. ^{31}P-NMR spectra of a THF solution containing **W**$(N_2)_2$ (blue trace), (OTs)**W**$(NNH_2)^+$ (green trace), and **W**$(N_2)_2$ with 2 equiv of TsOH and 10 equiv [TBA][BF_4] as the electrolyte (red trace). The latter shows that protonation of the **W**$(N_2)_2$ in the presence of BF_4^- leads to a hydrazido species distinct from (OTs)**W**$(NNH_2)^+$. The doublet resonance observed is diagnostic for a fluoride complex and this result is hence most consistent with the formation of the known complex (F)**W**$(NNH_2)^+$ instead of (OTs)**W**$(NNH_2)^+$.[27]

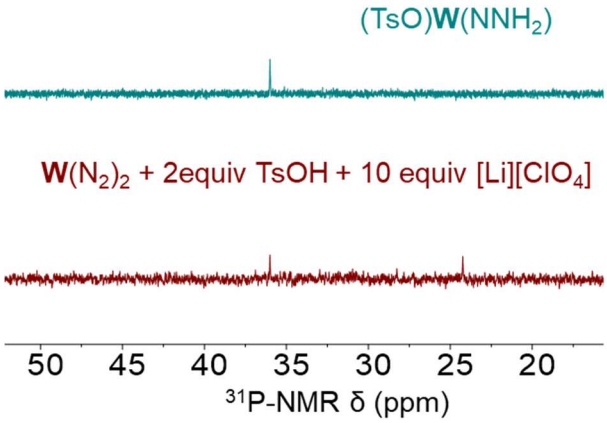

Figure S20. ^{31}P-NMR spectra of a THF solution containing (OTs)**W**$(NNH_2)^+$ (blue trace) and **W**$(N_2)_2$ with 2 equiv of TsOH and 10 equiv [Li][ClO_4] (red trace). The latter shows the partial formation of (OTs)**W**$(NNH_2)^+$, together with a second species that we tentatively assign to a previously reported W-trans-dioxo species, based on a previous report.[23] This experiment underscores that perchlorate can be non-innocent during electrocatalysis with [Li][ClO_4] as the electrolyte.

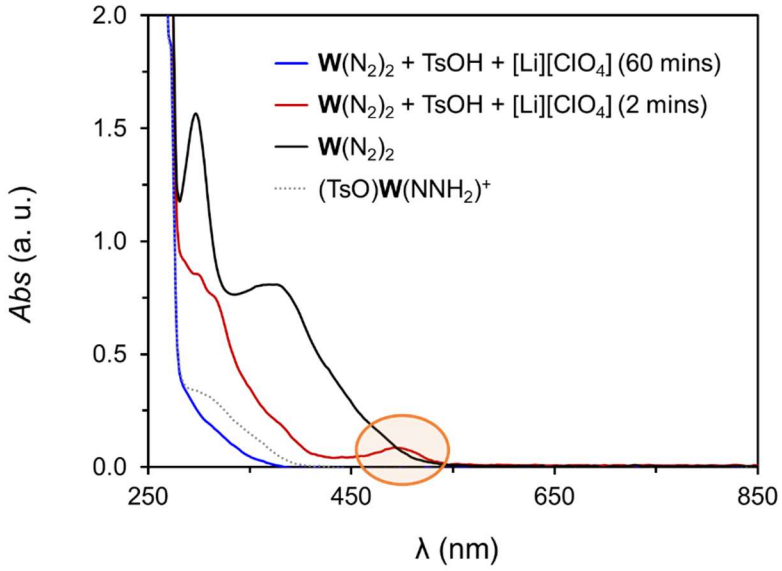

Figure S21. UV-vis spectra of a THF solution containing 0.05 mM (OTs)**W**$(NNH_2)^+$ (dashed gray trace), 0.05 mM **W**$(N_2)_2$ (black trace), and 0.05 mM **W**$(N_2)_2$ with 2 equiv of TsOH, and 10 equiv [Li][ClO_4] after 2 mins (red trace) and 60 mins (blue trace) of reaction. The absorption band at around 500 nm in the red trace supports the formation of the W-oxo species, consistent with literature reports,[23] which is unstable and disappears after 60 min of reaction time, leading to lower concentrations of the hydrazido species as compared with a UV-vis sample containing a similar initial concentration of pure (OTs)**W**$(NNH_2)^+$ in THF (gray trace). This experiment underscores that perchlorate can be non-innocent during electrocatalysis with [Li][ClO_4] as the electrolyte.

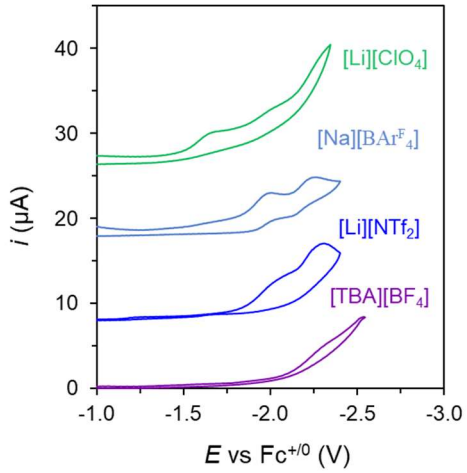

Figure S22. CV at 100 $mV \cdot s^{-1}$ of a THF solution containing 0.05 mM **W**$(N_2)_2$ and 2 equiv of TsOH for the in situ formation of (TsO)**W**$(NNH_2)^+$ using different electrolytes: [Li][ClO_4], [Na][$BAr^F{}_4$], [Li][NTf_2] and [TBA][BF_4]. A BDD disk was used as the working electrode.

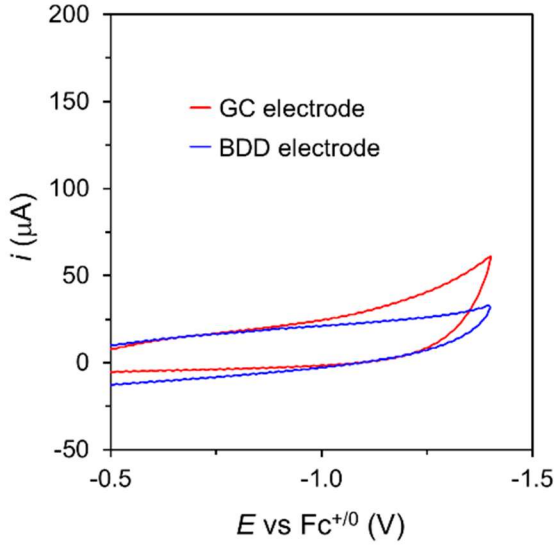

Figure S23. CV at 100 $mV \cdot s^{-1}$ in 0.1 M [Li][NTf_2] DME solution containing 5 mM TsOH, using either a GC (red) or a BDD (blue) plate working electrode.

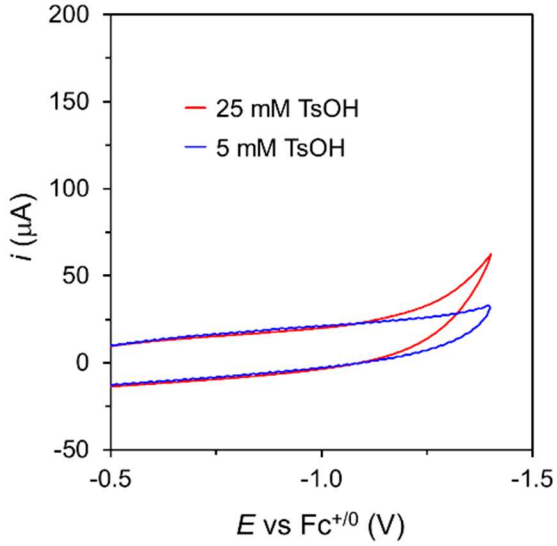

Figure S24. CV at 100 $mV \cdot s^{-1}$ in 0.1 M [Li][NTf_2] DME solution containing either 5 mM (blue trace) or 25 mM (red trace) TsOH, using a BDD plate working electrode.

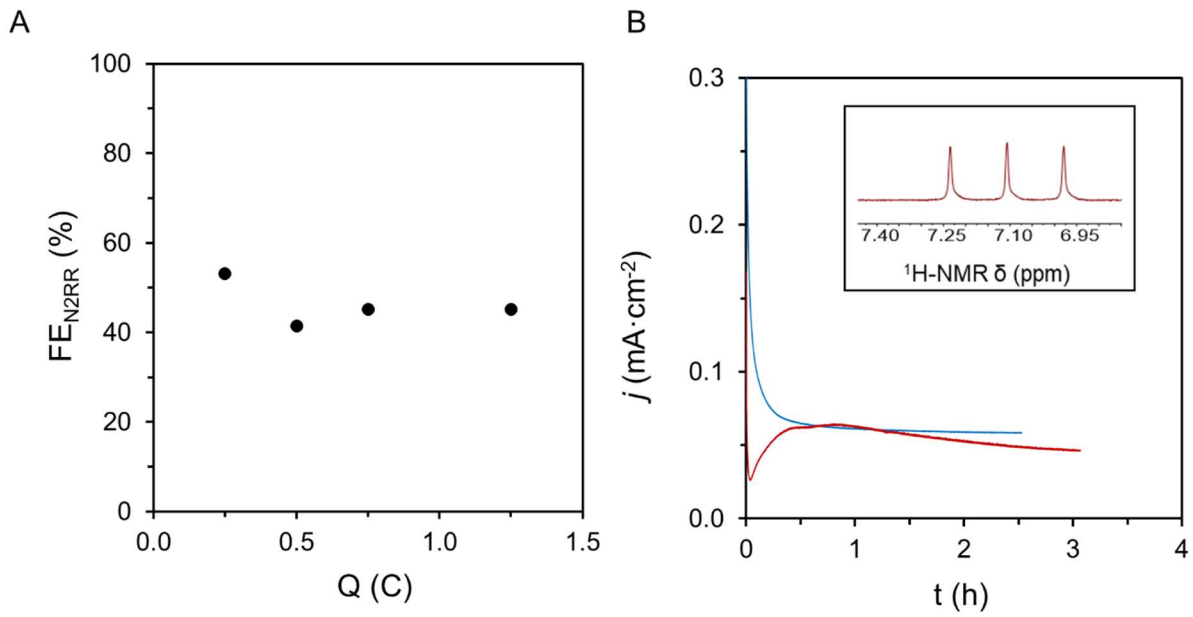

Figure S25. (A) FE for NH_3 generation obtained after different CPC experiments using 0.05 mM $W(N_2)_2$ and 0.05 mM $Co(III,N)^+$ catalysts at -1.35 V in a DME electrolyte solution with 0.1 M [Li][NTf_2] and 5 mM TsOH that have been stopped at different total charge passed. (B) Current and charge profile for two consecutive CPC at −1.35 V vs $Fc^{+/0}$ in 0.1 M [Li][NTf_2] DME solution containing initially 0.05 mM **Co**(III,N)$^+$, 0.05 mM **W**$(N_2)_2$ and 5 mM TsOH, using a BDD plate working electrode. After the first CPC (blue trace), an extra 100 equiv of TsOH were added through a septum as a concentrated DME solution, and the second CPC was initiated (red trace). **Inset**: Quantification of generated NH_3 via ^{1}H-NMR spectroscopy, resulting in 17.3 equiv of NH_3.

S6. Control experiments for electrocatalytic N_2RR:

In order to verify that the produced ammonia derives solely from the electrocatalytic reduction of N_2 by the tandem co-catalytic system, several CPC control experiments were performed to evaluate any possible source of NH_3 contamination, or any other N-containing species as the substrate, for the generation of NH_3. In addition, the content of other N-containing impurities like N_2O, NO_x, NO_2^- and NO_3^-, were probed quantitatively using appropriate analytical methods. These results, summarized below, unequivocally verify atmospheric N_2 as the substrate.

S6.1. Control experiment under Argon atmosphere:

The electrochemical cell was set up as in a typical experiment in a N_2-filled glove box containing the two co-catalysts, the electrolyte solution, the acid, and the three electrodes. Subsequently, the gas-tight cell was brought outside the box and both compartments were bubbled with Argon gas through the septa for 30 mins in order to displace all the N_2. After that time, a CPC was run at −1.35 V vs $Fc^{+/0}$ as usual (Figure 23). When the CPC was finished, excess of tosic acid (100 equiv dissolved in 1 mL of DME) was added through the septa with a syringe in order to quench all possible free ammonia in solution as NH_4^+. Subsequently, the cell was placed in a dry ice/acetone bath at −78 ºC to condense possible evaporated ammonia in the headspace. After 10 min at this temperature, the electrochemical cell was brought to room temperature and allowed to stir for another 10 min in the presence of the excess acid. Finally, the cell was opened, and the electrolyte solution was treated as previously described for quantification of ammonia. The total ammonia produced during this experiment was below 0.1 equiv (< 10 nmol). This experiment provides evidence against contamination of NH_3 in the electrochemical set up, as well as the absence of any other N-containing species that can act as an N-source for the generation of ammonia upon reduction, such as the [Li][NTf_2], or NO_2^- or NO_3^- in the electrolyte solution.

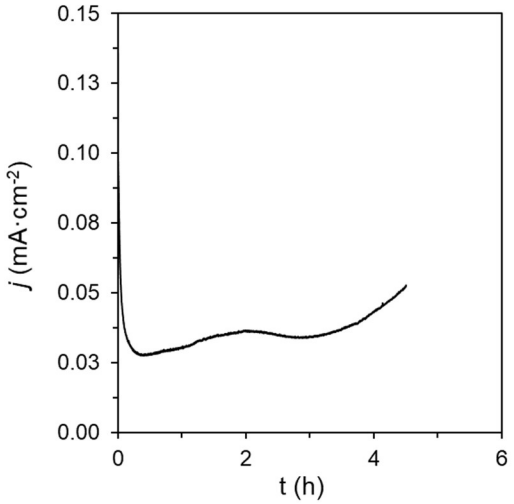

Figure S26. Current profile for a CPC at −1.35 V vs $Fc^{+/0}$ in 0.1 M [Li][NTf_2] DME solution containing 0.05 mM **Co**(III,N)$^+$, 0.05 mM **W**(N_2)$_2$ and 5 mM TsOH, under Argon atmosphere using a BDD plate working electrode.

S6.2 Control experiment using $^{15}N_2$ atmosphere:

The electrochemical cell was set up as in a typical experiment in a N_2-filled glove box containing the two co-catalysts, the electrolyte solution, the acid, and the three electrodes. The gas-tight cell was brought outside the box and both compartments were bubbled with Argon gas through the septa for 30 mins in order to make sure all the $^{14}N_2$ was displaced, as evidenced in previous control experiment under Argon atmosphere. Subsequently, the cell was then bubbled with $^{15}N_2$ for 5 mins to substitute the Ar, and then left to equilibrate for 5 more mins under the $^{15}N_2$ atmosphere. After that time, a CPC was run at −1.35 V vs $Fc^{+/0}$ using the typical procedure (Figure S27). When the CPC was finished, an excess of tosic acid (twice as much as theoretical $^{15}NH_3$ produced) was added through the septa with a syringe in order to quench all possible free $^{15}NH_3$ in solution as $^{15}NH_4^+$. Subsequently, the cell was placed in a dry ice/acetone bath at −78 ºC in order to condense possible evaporated ammonia in the headspace. After 10 min at this temperature, the electrochemical cell was brought to room temperature and allowed to stir for another 10 min in the presence of the excess acid. Finally, the cell was opened, and the electrolyte solution was treated as previously described for quantification of ammonia. This experiment provides evidence against contamination of $^{14}NH_3$ in the electrochemical set up, as well as the absence of any other N-containing species that could act as N-source for the generation of ammonia upon reduction such as N_2O, NO_x gasses in the gas supply, or [Li][NTf_2], NO_2^-, or NO_3^- in the electrolyte solution.

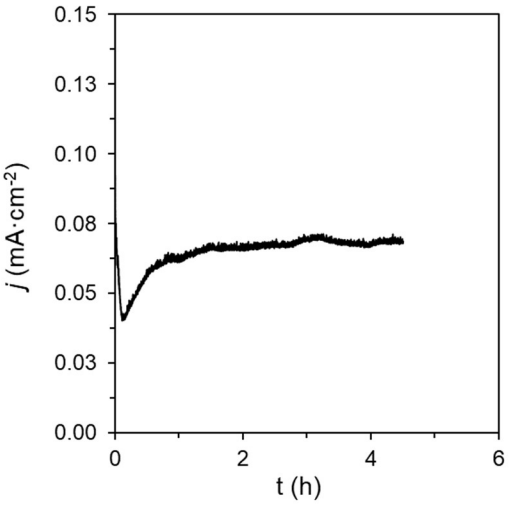

Figure S27. Current profile for a CPC at −1.35 V vs $Fc^{+/0}$ in 0.1 M [Li][NTf_2] DME solution containing 0.05 mM **Co**(III,N)$^+$, 0.05 mM **W**(N_2)$_2$ and 5 mM TsOH, under $^{15}N_2$ atmosphere using a BDD plate working electrode.

S6.3 Control experiment in the absence of catalysts:

In order to further support that the source of produced ammonia is the electrochemical reduction of N_2 by the tandem co-catalytic system, instead of any NH_3 contamination or direct reduction of N_2O, NO_x, [Li][NTf_2], NO_2^- or NO_3^- at the electrode, a CPC was also performed in the absence of **Co**(III,N)$^+$ and **W**$(N_2)_2$ (Figure S28).

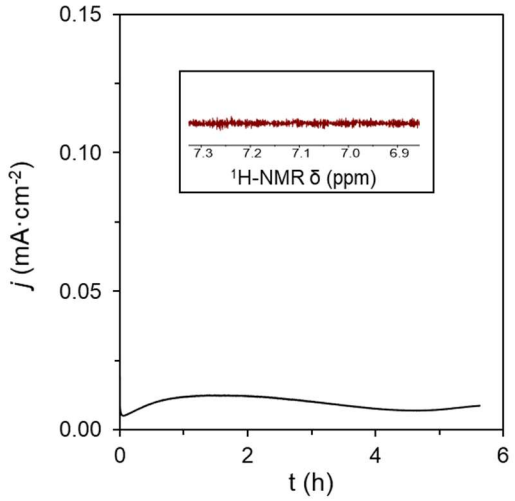

Figure S28. Current profile for a CPC at −1.35 V vs $Fc^{+/0}$ in 0.1 M [Li][NTf_2] DME solution containing 5 mM TsOH, under $^{14}N_2$ atmosphere using a BDD plate working electrode. **Inset**: Quantification of NH_3 via ^{1}H-NMR under previous conditions.

S6.4 Quantification of N_2O impurities in the N_2 gas supply via GC-TCD:

The content of N_2O in the N_2 gas supplies for both $^{14}N_2$ and $^{15}N_2$ was determined by gas chromatography coupled to a thermal conductivity detector (GC-TCD). The method employed included a detector temperature of 250 ºC, inlet temperature of 150 ºC, and an oven maximum temperature of 275 ºC. Calibration of the N_2O signal was performed by injecting pure N_2O gas and a standard mixture of N_2 containing 1 ppm of N_2O using a gas-tight Hamilton syringe. Under these conditions, an N_2O signal appears at a retention time of 6.8 mins.

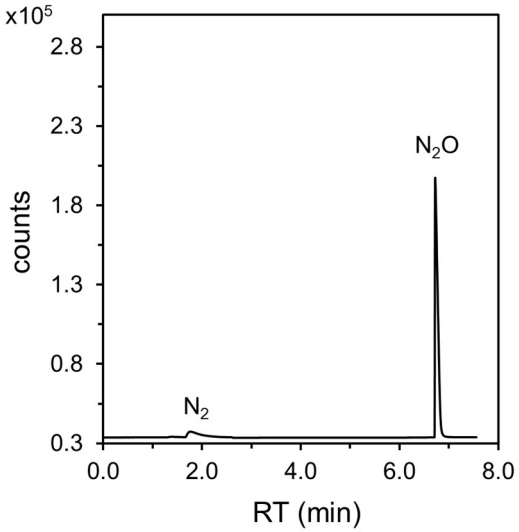

Figure S29. Gas chromatogram of an injection of N_2O gas for determination of the retention time. The peak at around 1.8 mins correspond to trace N_2 gas.

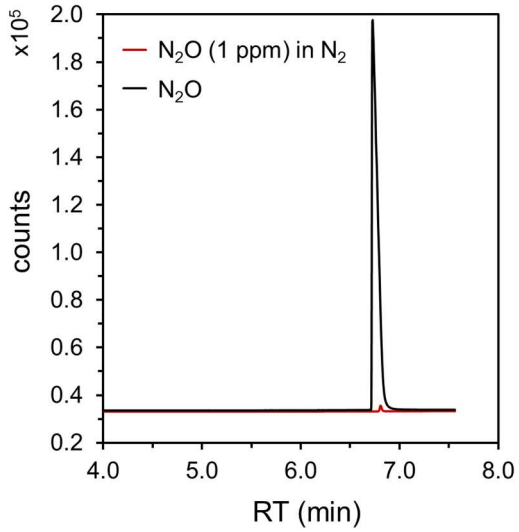

Figure S30. Gas chromatogram of an injection of N_2O gas (black trace) and a mixture of N_2 with 1 ppm of N_2O for calibration of the area.

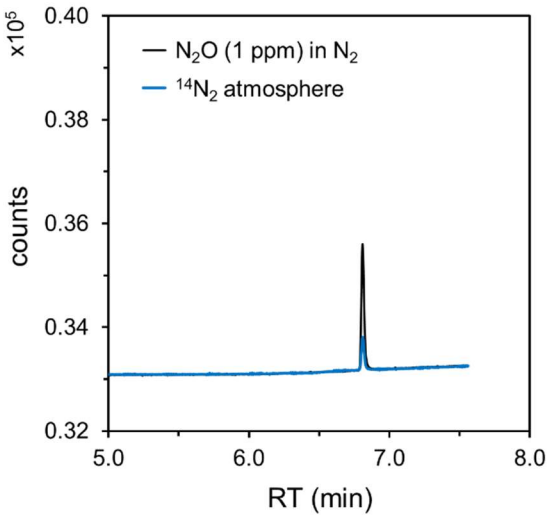

Figure S31. Gas chromatogram of an injection of a mixture of N_2 with 1 ppm of N_2O (black trace) and the $^{14}N_2$ gas from the glove box employed for the N_2RR experiments (blue trace).

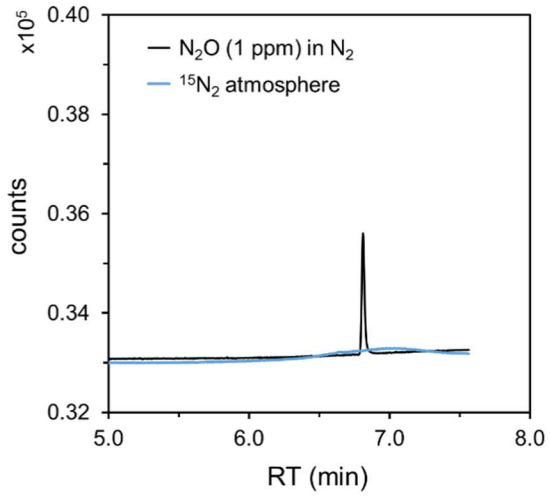

Figure S32. Gas chromatogram of an injection of a mixture of N_2 with 1 ppm of N_2O (black trace) and the $^{15}N_2$ gas from the gas cylinder employed for the control N_2RR experiment (blue trace).

S6.5 Quantification of NO_x impurities in the N_2 gas supply via the Griess method:

Determination of the NO_x impurities in the gas supplies was performed by their conversion to NO_2^- and NO_3^- in basic media and quantification of the latter by the Griess method.[14] Specifically, the electrochemical cell exposed to either $^{14}N_2$ or $^{15}N_2$ atmosphere employed in the N_2RR experiments was filled with 6 mL of 0.1 M KOH aqueous solution left stirring over 2 h. Any NO_x impurity is assumed to be quantitatively converted into NO_2^- or NO_3^- in this basic solution, and these compounds can in turn be quantified using the Griess spectrophotometric method with the color development solutions described in Methods. This was done by sampling 500 μL of the KOH trap solution and adding 500 μL of a 0.1 M HCl aqueous solution, 25 μL of the sulphanilamide solution and 25 μL of the N-1-naphtylethylenediamine dihydrochloride solution. The resulting mixture was incubated for 20 min at room temperature and subsequently the UV-vis spectrum was obtained in a 1 cm quartz cuvette. Absorption at 550 nm enables evaluation of the NO_2^- content upon calibration. For the calibration plots, standard solutions containing different concentrations of $NaNO_2$ in 0.1 M KOH were subjected to the same color development procedure. For quantification of NO_3^-, the solution used in the quantification of NO_2^- was reacted with 50 μL of a vanadium(III) chloride (VCl_3) solution in 6 M aqueous HCl and incubated at 60 ºC during 25 mins in order to quantitatively reduce the NO_3^- to NO_2^-. After that time, the solution was brought to room temperature and the absorption spectrum was again obtained for evaluation of the band at 550 nm. No significant content of NO_x impurities was found in either $^{14}N_2$ or $^{15}N_2$ gas supplies corresponding to the amounts of NH_3 produced in this work, supporting N_2 as the sole source of NH_3.

Calibration plots were performed for both NO_2^- and NO_3^- using their corresponding sodium salts as standard samples and preparing solutions in a range of relevant concentrations. Both calibration plots were linear with $R^2 > 0.99$, and the regression lines were employed for direct, quantitative determination of the NO_2^- and NO_3^- content in the different samples to analyze.

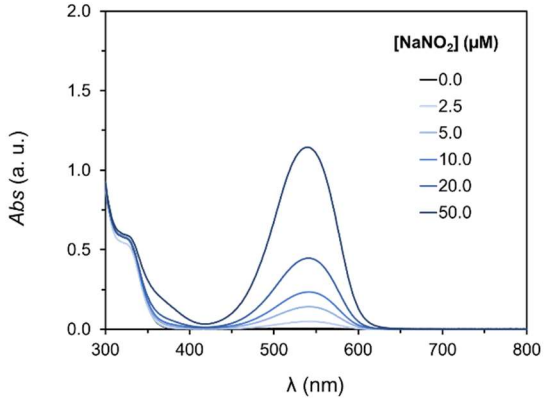

Figure S33. UV-vis spectra of solutions containing different concentrations of $NaNO_2$ for calibration purposes subjected to the previously described protocol for quantification based on the Griess method.

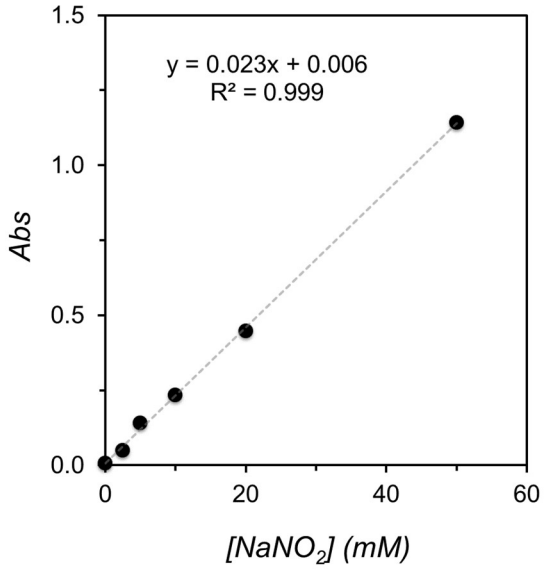

Figure S34. Calibration plot of the Griess analysis for NO_2^- with the corresponding linear regression.

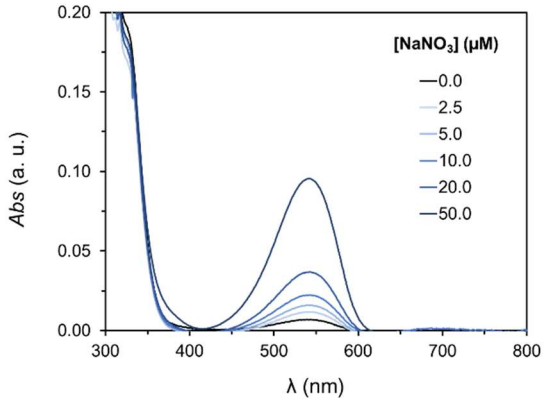

Figure S35. UV-vis spectra of solutions containing different concentrations of $NaNO_3$ for calibration purposes subjected to the previously described protocol for quantification based on the Griess method.

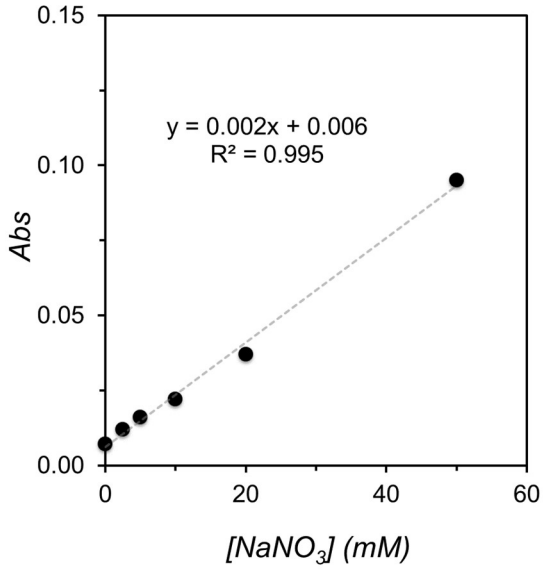

Figure S36. Calibration plot of the Griess analysis for NO_3^- with the corresponding linear regression.

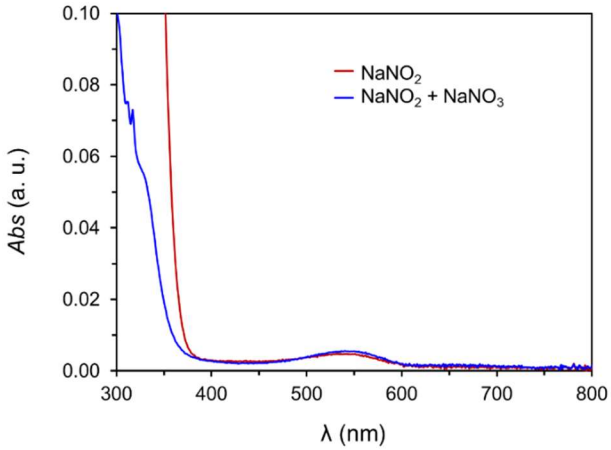

Figure S37. UV-vis spectra for the Griess analysis of a 0.1 M KOH solution exposed to the $^{14}N_2$ gas employed in the N_2RR CPC experiments for the determination of the NO_2^- and NO_3^- deriving from NO_x impurities. The content of $NO_2^- + NO_3^-$ is below 0.2 nmol based on the calibration plots.

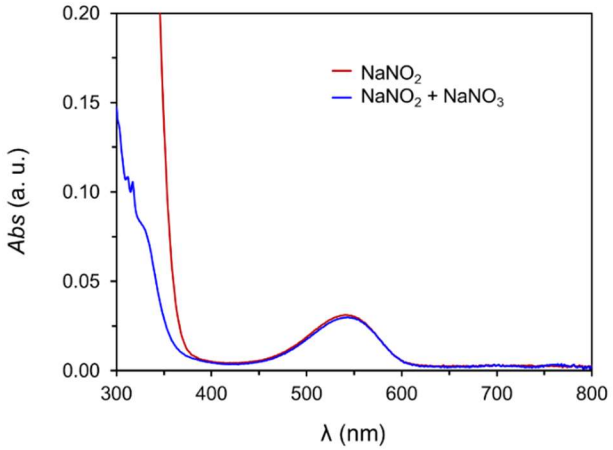

Figure S38. UV-vis spectra for the Griess analysis of a 0.1 M KOH solution exposed to the $^{15}N_2$ gas employed in the control N_2RR CPC experiments for the determination of the NO_2^- and NO_3^-deriving from NO_x impurities. The content of NO_2^- + NO_3^- is below 2.1 nmol based on the calibration plots.

S6.6 Quantification of NO_2^- and NO_3^- impurities in the electrolyte via Griess method:

The content of NO_2^- and NO_3^- impurities in the electrolyte solution was also determined using the Griess method and the calibration plots previously obtained. For that, THF and DME solutions containing either 0.2 M [TBA][BF_4] or 0.1 M [Li][NTf_2] and 5 mM TsOH were prepared under $^{14}N_2$ atmosphere in a glove box following similar procedure as in the CPC experiments. The solution was stirred for 2 h and the Griess method was performed as detailed above. The amount of NO_2^- or NO_3^- impurities were trace from the electrolyte solutions and insignificant relevant to the amounts of NH_3 produced in this work, supporting along with other controls that N_2 as the sole source of NH_3 produced.

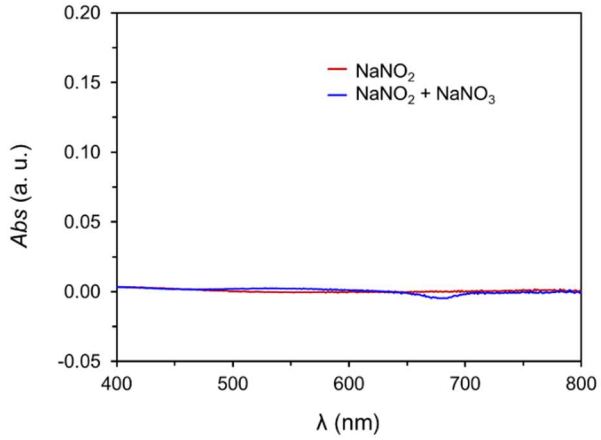

Figure S39. UV-vis spectra for the Griess analysis of a THF solution containing 0.2 M [TBA][BF_4] and 5 mM TsOH, as employed in the CPC experiments, for the determination of the NO_2^- (red trace) and NO_3^- (blue trace). The content of NO_2^- + NO_3^- is below 0.1 nmol based on the calibration plots.

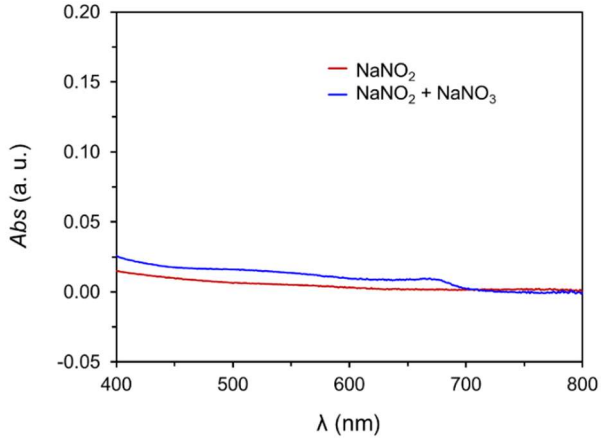

Figure S40. UV-vis spectra for the Griess analysis of a THF solution containing 0.1 M [Li][NTf_2] and 5 mM TsOH, as employed in the CPC experiments, for the determination of the NO_2^- (red trace) and NO_3^- (blue trace). The content of NO_2^- + NO_3^- is below 0.1 nmol based on the calibration plots.

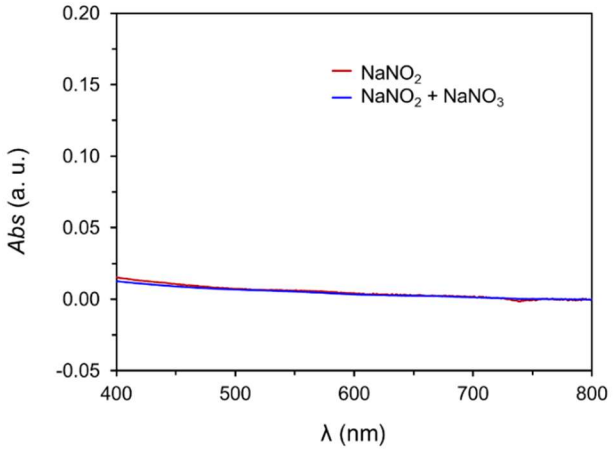

Figure S41. UV-vis spectra for the Griess analysis of a DME solution containing 0.1 M [Li][NTf_2] and 5 mM TsOH, as employed in the CPC experiments, for the determination of the NO_2^- (red trace) and NO_3^- (blue trace). The content of NO_2^- + NO_3^- is below 0.1 nmol based on the calibration plots.

S7. H_2 analysis:

Once the CPC experiment is finished, the headspace is analyzed for H_2 via gas chromatography with a thermal conductivity detector (GC-TCD) using a 100 µL Hamilton syringe to sample the headspace and to inject into the GC-TCD.

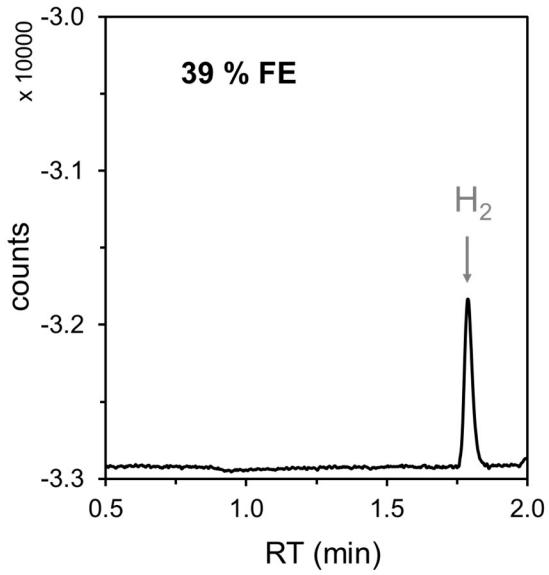

Figure S42. GC-TCD chromatogram of the headspace after CPC at −1.35 V vs $Fc^{+/0}$ of a solution containing 0.1 M [Li][NTf_2], 5 mM TsOH 0.05 mM $Co(III,N)^+$ and 0.05 mM $W(N_2)_2$.

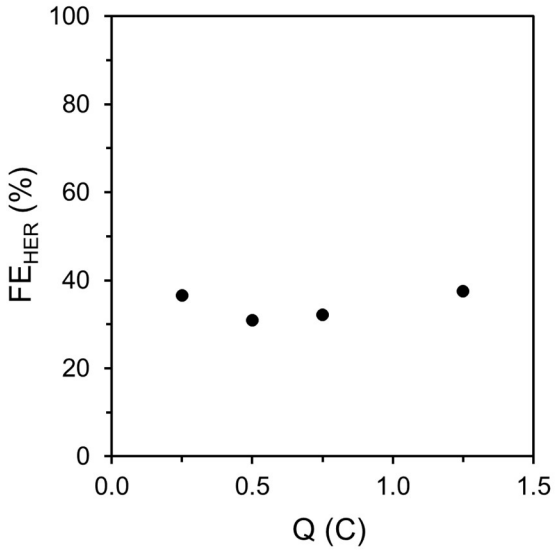

Figure S43. FE for H_2 generation obtained after different CPC experiments using 0.05 mM $W(N_2)_2$ and 0.05 mM $Co(III,N)^+$ catalysts at -1.35 V in a DME electrolyte solution with 0.1 M [Li][NTf_2] and 5 mM TsOH that have been stopped at different total charge passed.

S8. Post-CPC analysis:

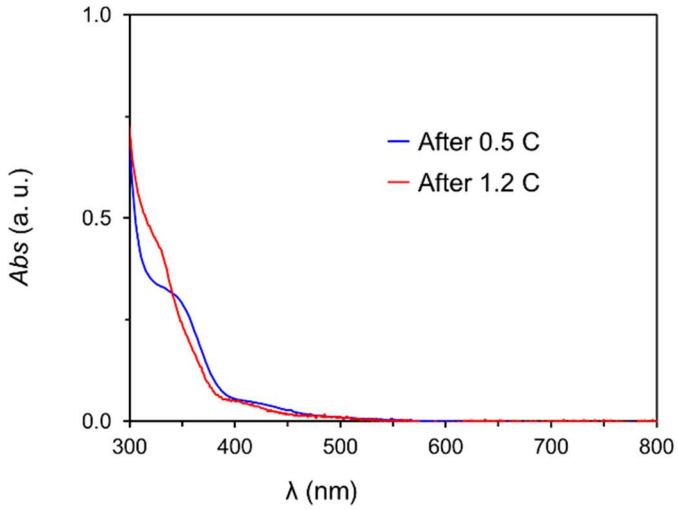

Figure S44. UV-vis analysis of the electrolyte solution during a CPC experiment after either 0.5 C or 1.2 C have passed. In these experiments, 2 ml of electrolyte solution were rapidly transfer to a gas-tight UV-vis cuvette under N_2 atmosphere and the spectrum was obtained (aprox. 15 s of delay).

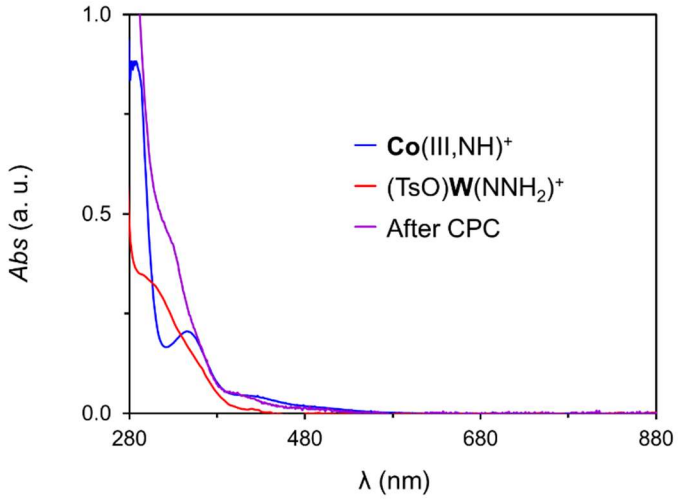

Figure S45. UV-vis analysis of a DME solution containing 0.1 M [Li][NTf_2], 5 mM TsOH and: (A) 0.05 mM $Co(III,N)^+$; (B) 0.05 mM $(TsO)W(NNH_2)^+$; (C) 0.05 mM $Co(III,N)^+$ and $(TsO)W(NNH_2)^+$ after a CPC experiment at -1.35 V.

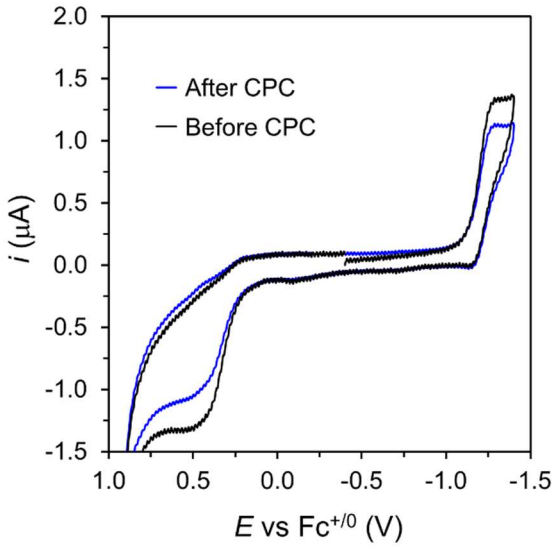

Figure S46. CV analysis of the electrolyte solution before and after a CPC experiment using $W(N_2)_2$ and $Co(III,N)^+$ catalysts at -1.35 V in THF containing 0.1 M [Li][NTf_2].

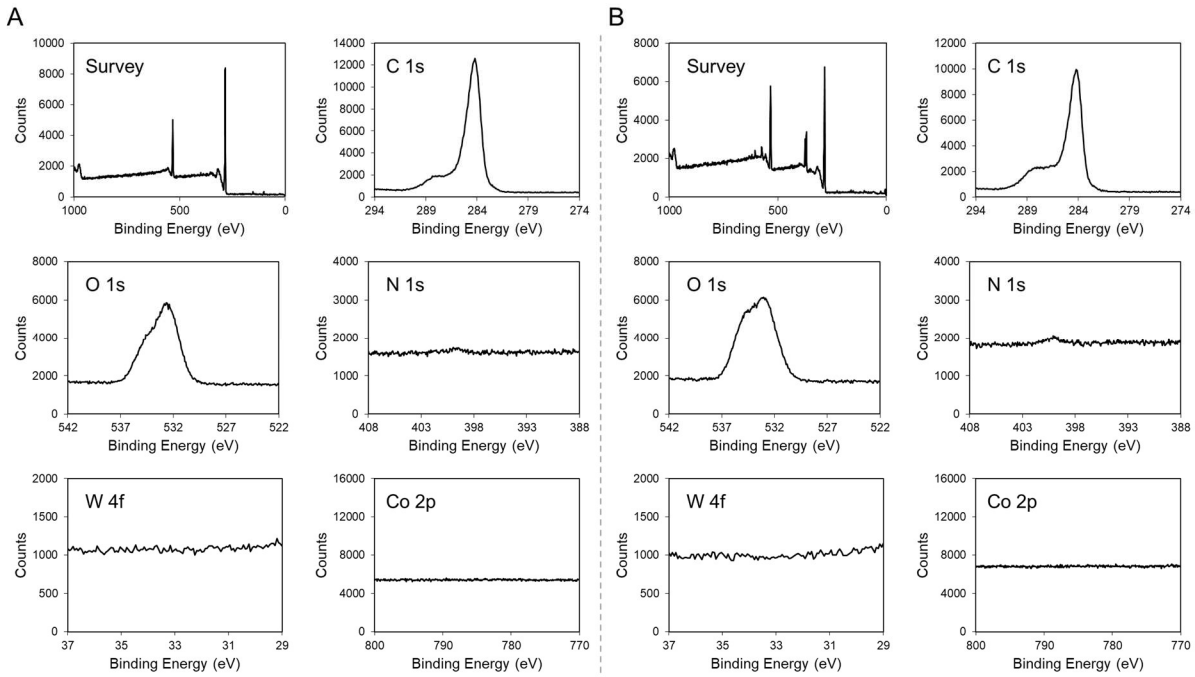

Figure S47. XPS analysis of the BDD electrode (A) before and (B) after a CPC experiment using 0.05 mM $W(N_2)_2$ and 0.05 mM $Co(III,N)^+$ catalysts at -1.35 V in a DME electrolyte solution with 0.1 M [Li][NTf_2] and 5 mM TsOH.

S9. Protonation of $W(N_2)_2$:

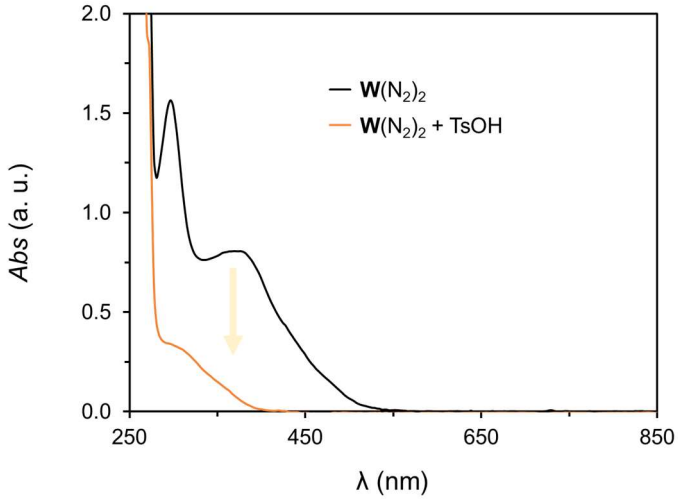

Figure S48. UV-vis spectra of a THF solution containing 0.05 mM **W**$(N_2)_2$ before (black trace) and after (yellow trace) addition of 100 equiv of TsOH for the quantitative formation of the hydrazido intermediate (TsO)**W**$(NNH_2)^+$.

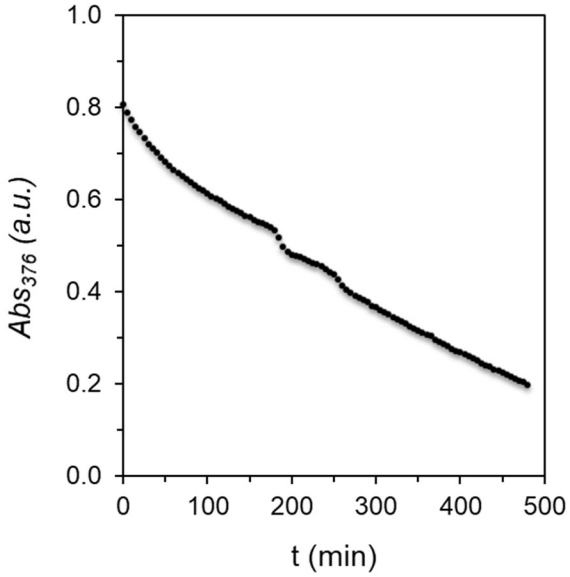

Figure S49. Time evolution of the absorption at 376 nm of a THF solution containing 0.05 mM **W**$(N_2)_2$ after addition of 100 equiv of TsOH for the quantitative formation of the hydrazido intermediate (TsO)**W**$(NNH_2)^+$.

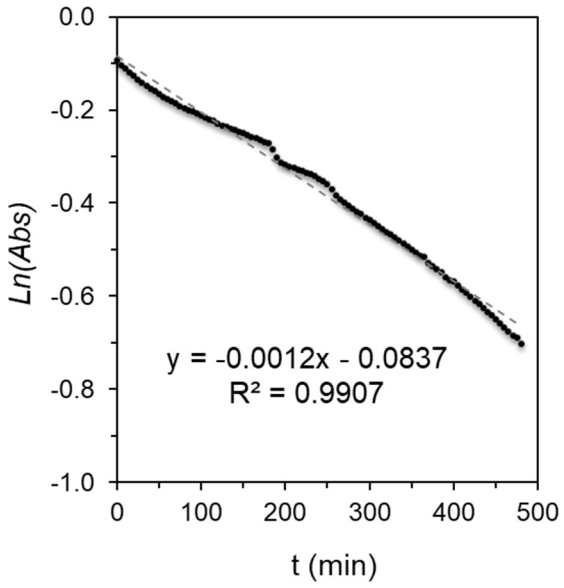

Figure S50. Plot of the natural logarithm of the absorption at 376 nm versus time of a THF solution containing 0.05 mM **W**$(N_2)_2$ after addition of 100 equiv of TsOH for the quantitative formation of the hydrazido intermediate (TsO)**W**$(NNH_2)^+$. The plot reflects a pseudo first order reaction with a k_{obs} of 0.0012 min^{-1} for the protonation of the dinitrogen complex, consistent with previous work studying these protonation steps.[28]

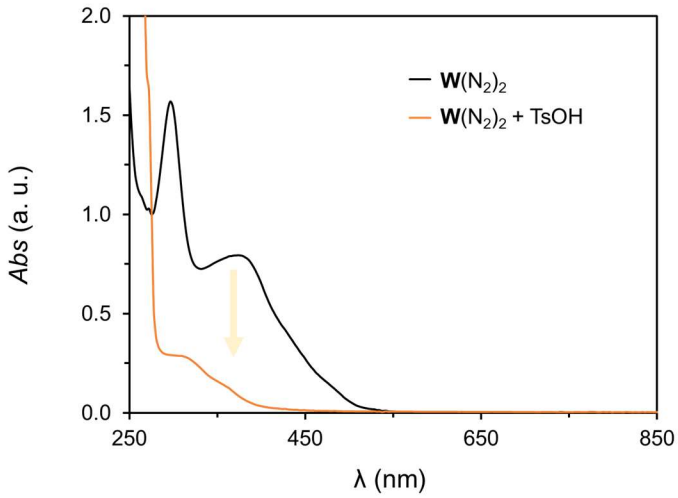

Figure S51. UV-vis spectra of a THF solution containing 0.1 M [Li][NTf_2] and 0.05 mM **W**$(N_2)_2$ before (black trace) and after (yellow trace) addition of 100 equiv of TsOH for the quantitative formation of the hydrazido intermediate (TsO)**W**$(NNH_2)^+$.

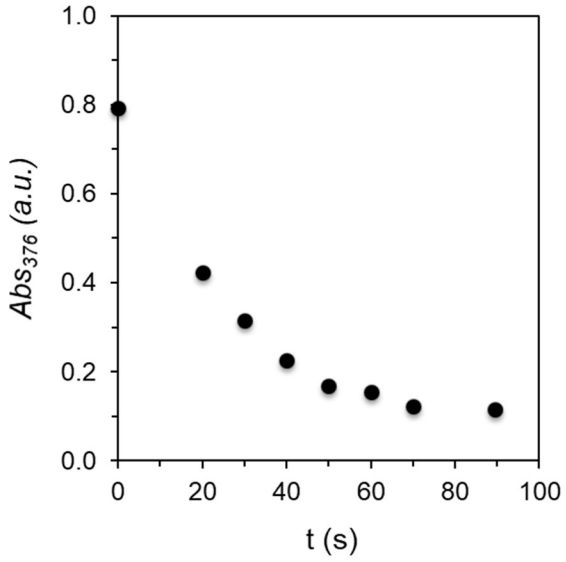

Figure S52. Time evolution of the absorption at 376 nm of a THF solution containing 0.1 M [Li][NTf_2] and 0.05 mM **W**(N_2)$_2$ after addition of 100 equiv of TsOH for the quantitative formation of the hydrazido intermediate (TsO)**W**(NNH_2)$^+$.

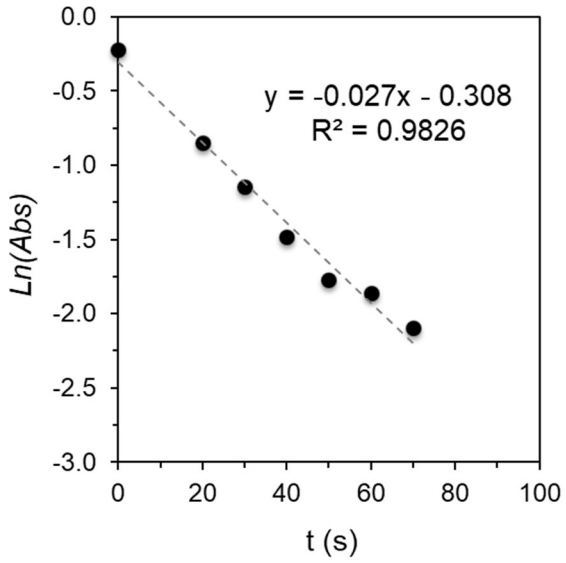

Figure S53. Plot of the natural logarithm of the absorption at 376 nm versus time of a THF solution containing 0.1 M [Li][NTf_2], 0.05 mM **W**(N_2)$_2$ after addition of 100 equiv of TsOH for the quantitative formation of the hydrazido intermediate (TsO)**W**(NNH_2)$^+$. The plot reflects a pseudo first order reaction with a k_{obs} of 0.027 s^{-1} for the protonation of the dinitrogen complex, consistent with its influence in the overall rate of catalysis and the observed partial order in acid. The faster rate than observed with [TBA][BF_4] is consistent with a potential role of the [Li][NTf_2] in activating the dinitrogen complex and/or stabilizing the hydrogen bonded intermediates.[29]

S10. Chemical PCET reactions:

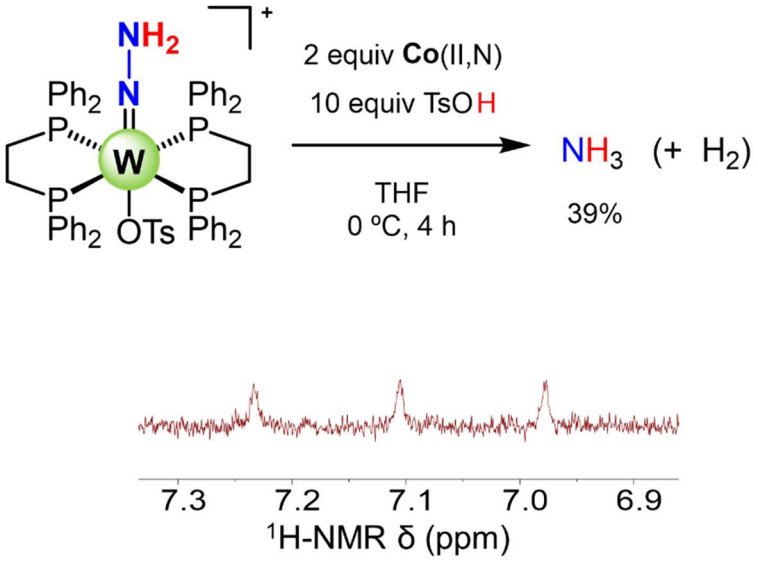

Figure S54. Chemical reaction of 0.5 mM (TsO)**W**$(NNH_2)^+$ in THF with 2 equiv **Co**(II,N) in the presence of excess acid and the corresponding ^{1}H-NMR spectrum after work up for the quantification of NH_3 produced. These results show the capability of **Co**$(II,NH)^+$, formed after rapid protonation of **Co**(II,N), to reduce the (TsO)**W**$(NNH_2)^+$ intermediate, leading to the formation of ammonia.

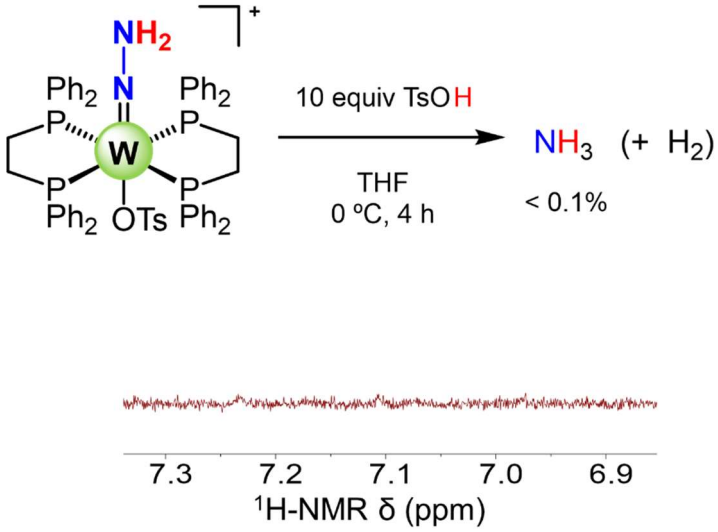

Figure S55. Chemical reaction of 0.5 mM (TsO)**W**$(NNH_2)^+$ in THF with excess acid in the absence of the **Co**(II,N) mediator and the corresponding ^{1}H-NMR spectrum after work up for the quantification of NH_3 produced (< 3%). These results show the absence of significant reactivity between the (TsO)**W**$(NNH_2)^+$ intermediate and acid leading to the formation of ammonia. The trace NH_3 observed may arise from a disproportionation reaction, for example where a tungsten complex serves as a source of electrons.[30]

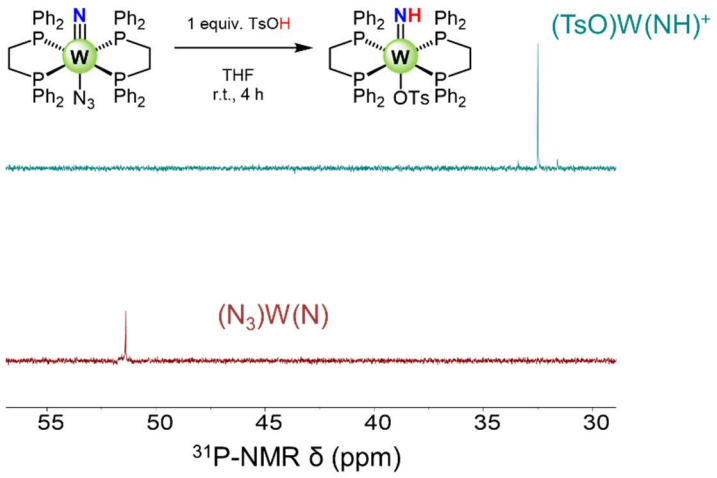

Figure S56. ^{31}P-NMR spectrum of 0.5 mM (N_3)**W**(N) in THF before (red trace) and after (blue trace) addition of 1 equiv TsOH, showing the formation of the imido intermediate (X)**W**$(NH)^+$ (X = OTs or N_3).

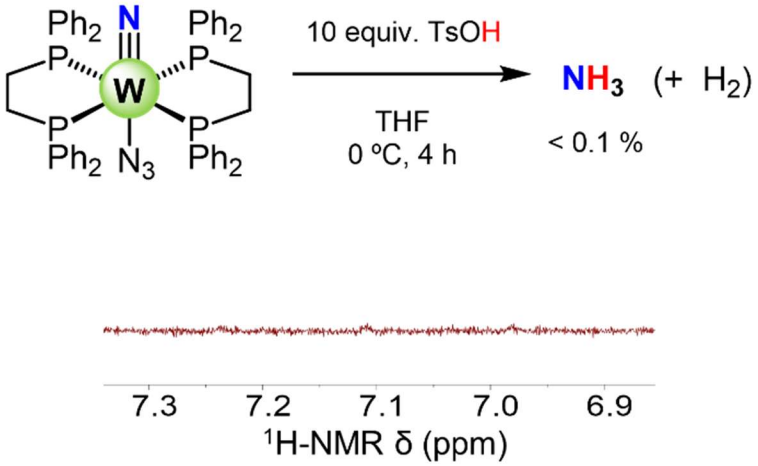

Figure S57. Chemical reaction of 0.5 mM (N_3)**W**(N) in THF with excess acid in the absence of the **Co**(II,N) mediator and the corresponding ^{1}H-NMR spectrum after work up for the quantification of NH_3 produced (< 3%). These results show the absence of significant reactivity between the (TsO)**W**$(NH)^+$ intermediate, formed by in situ protonation of (N_3)**W**(N), and acid leading to the formation of ammonia. The trace NH_3 observed my arise from a disproportionation reaction, for example where a tungsten complex serves as a source of electrons. [28]

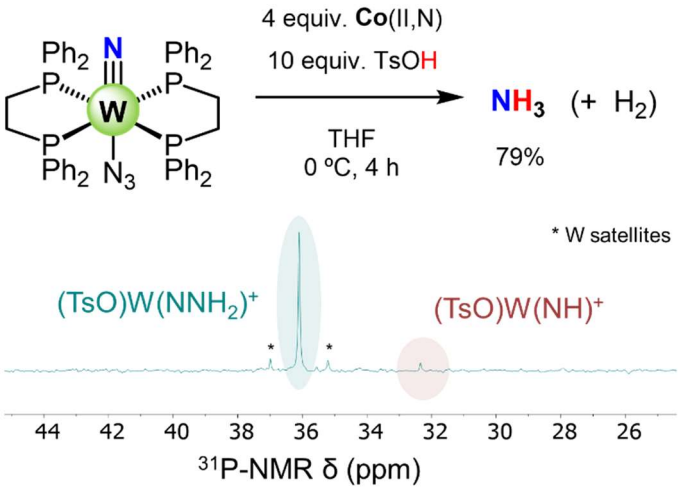

Figure S58. Chemical reaction of 0.5 mM (N_3)**W**(N) in THF with 4 equiv **Co**(II,N) in the presence of excess acid and the corresponding ^{31}P-NMR spectrum. The TsOH was added prior to the addition of **Co**(II,N) for the formation of (TsO)**W**$(NH)^+$. These results evidence the capability of **Co**$(II,NH)^+$, formed after rapid protonation of **Co**(II,N), to reduce the (TsO)**W**$(NH)^+$ intermediate, formed by in situ protonation of (N_3)**W**(N), towards formation of ammonia, and regeneration of **W**$(N_2)_2$, which then undergoes protonation with the excess of acid to form (TsO)**W**$(NNH_2)^+$.

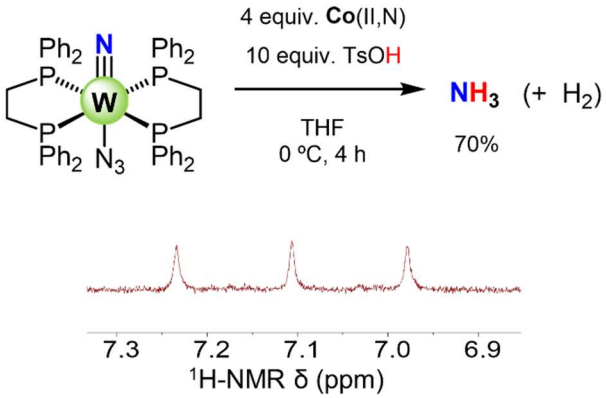

Figure S59. Chemical reaction of 0.5 mM (N_3)**W**(N) in THF with 4 equiv **Co**(II,N) in the presence of excess acid and the corresponding ^{1}H-NMR spectrum after work up for the quantification of NH_3 produced. The TsOH was added previous to the addition of **Co**(II,N) for the formation of (TsO)**W**$(NH)^+$. These results show the capability of **Co**$(II,NH)^+$, formed after rapid protonation of **Co**(II,N), to reduce the (TsO)**W**$(NH)^+$ intermediate (formed by previous protonation of (N_3)**W**(N)) towards formation of ammonia.

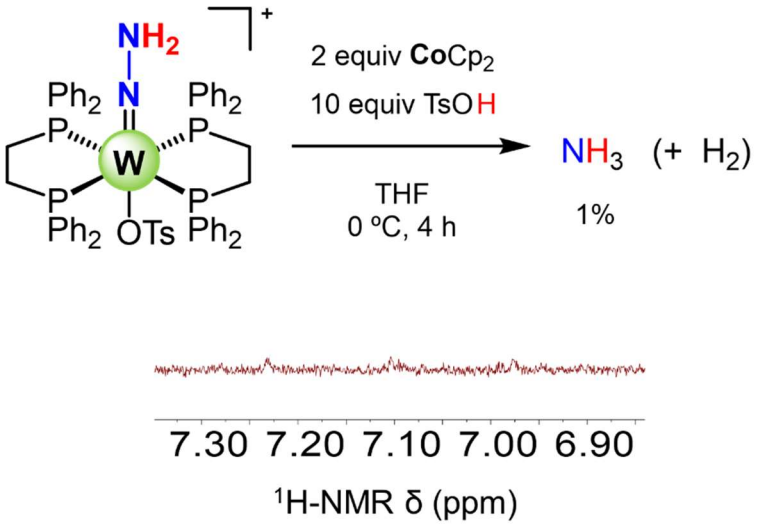

Figure S60. Chemical reaction of 0.5 mM (TsO)W(NNH$_2$)$^+$ in THF with 2 equiv CoCp$_2$ in the presence of excess acid and the corresponding ^{1}H-NMR spectrum after work up for the quantification of NH$_3$ produced.

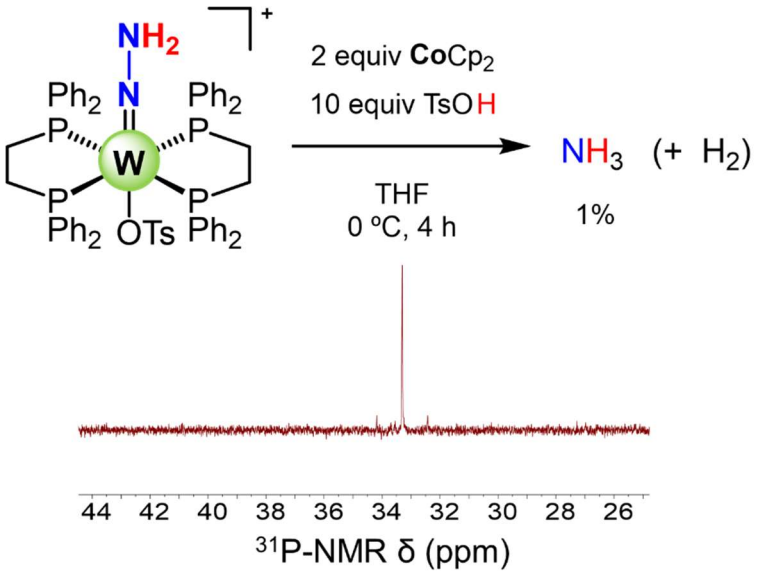

Figure S61. Chemical reaction of 0.5 mM (TsO)W(NNH$_2$)$^+$ in THF with 2 equiv CoCp$_2$ in the presence of excess acid and the corresponding ^{31}P-NMR spectrum after work up for the quantification of NH$_3$ produced.

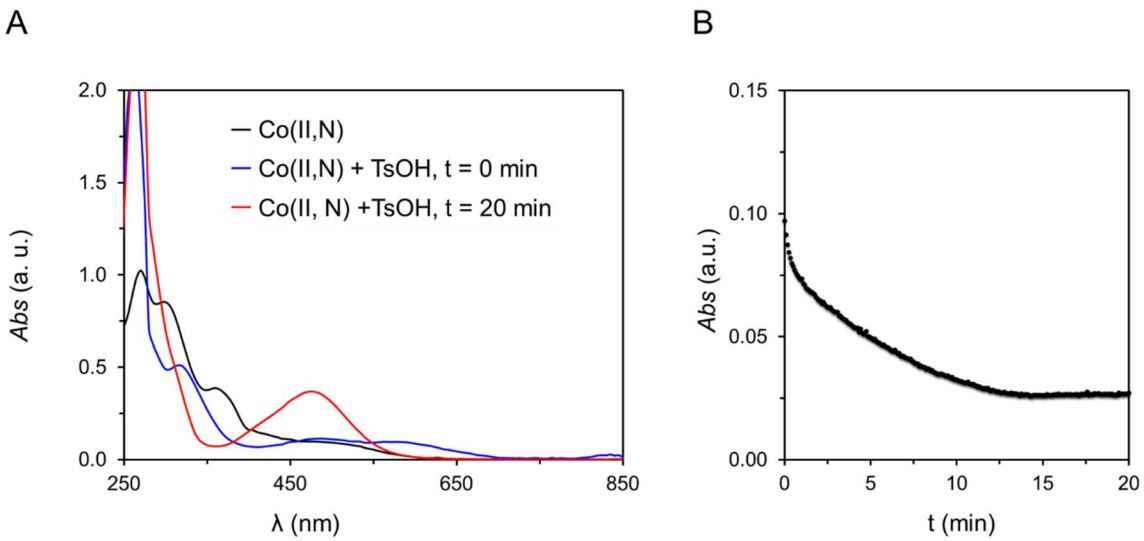

Figure S62. (A) UV-vis analysis at room temperature of the evolution of a DME solution containing 0.05 mM Co(II,N) upon addition of 5 equiv of TsOH. (B) Plot of the absorbance at 580 nm over time corresponding to the protonated $Co(II,NH)^{+}$ species, demonstrating its decay due to bimolecular H_2 elimination over the course of 20 mins.

S11. Mechanistic analysis via cyclic voltammetry:

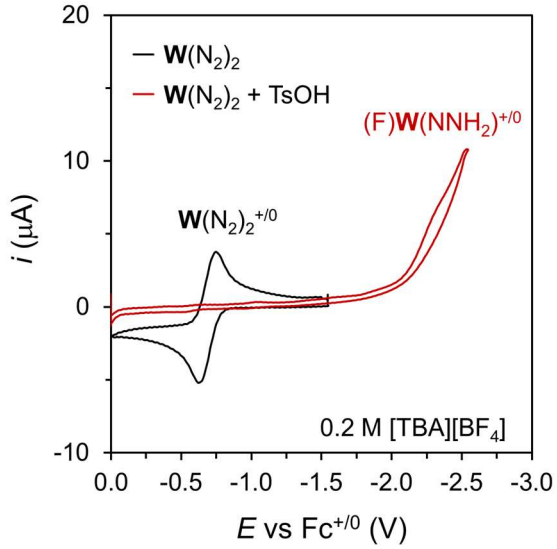

Figure S63. CV at 100 $mV \cdot s^{-1}$ of a 0.2 M [TBA][BF_4] THF solution containing 0.5 mM **W**(N_2) before (black trace) and after (red trace) addition of 2 equiv of TsOH showing the formation of (F)**W**(NNH_2)$^+$.

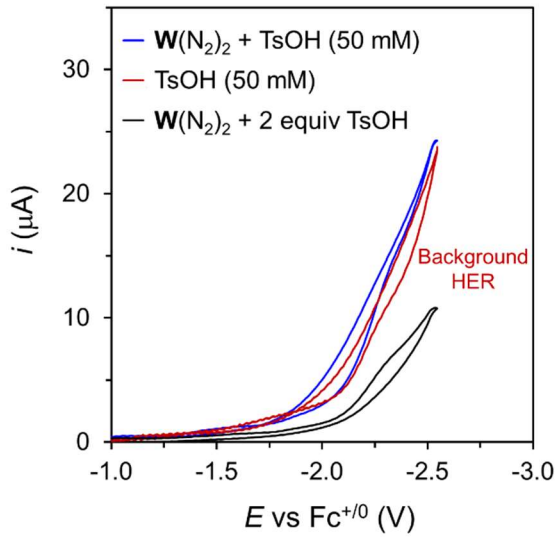

Figure S64. CV at 100 $mV \cdot s^{-1}$ of a 0.2 M [TBA][BF_4] THF solution containing 0.5 mM **W**(N_2) and 2 equiv of TsOH (black trace), 0.5 mM **W**(N_2) and 50 mM TsOH (blue trace), and only 50 mM TsOH (red trace). These results show the similar electrochemical response with excess TsOH in the presence and absence of **W**(N_2) consistent with dominant electrocatalytic HER mediated by the electrode under these conditions.

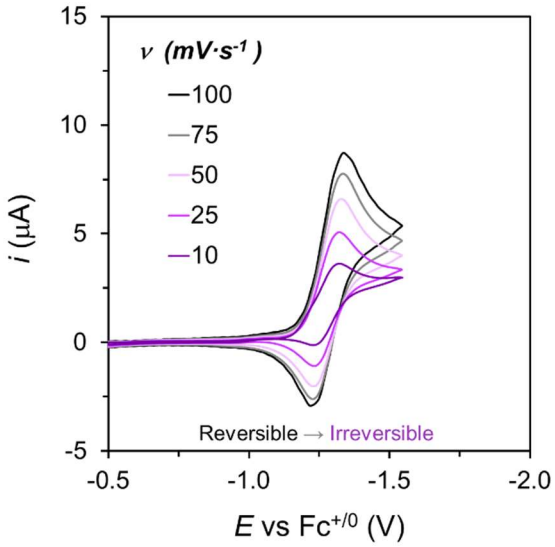

Figure S65. Variable scan rate CVs of a 0.2 M [TBA][BF_4] THF solution containing 0.5 mM **Co**(III,N)$^+$, 0.5 mM **W**(N_2) and 50 mM TsOH showing how at the slower scan rates the reversibility decreases, consistent with a catalytic process coupled to the reduction of in situ generated **Co**(III,NH)$^{2+}$ to **Co**(II,NH)$^+$.

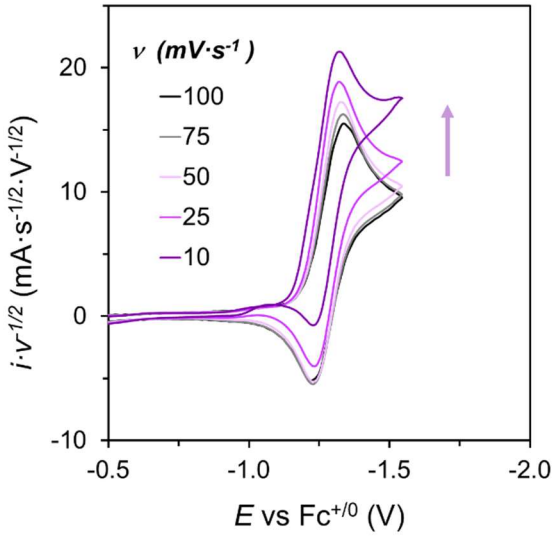

Figure S66. CVs normalized by the scan rate of a 0.2 M [TBA][BF_4] THF solution containing 0.5 mM **Co**(III,N)$^+$, 0.5 mM **W**(N_2) and 50 mM TsOH. These results show how at slower scan rates the reversibility decreases and the normalized current increases, consistent with a catalytic process coupled to the reduction of in situ generated **Co**(III,NH)$^{2+}$ to **Co**(II,NH)$^+$.

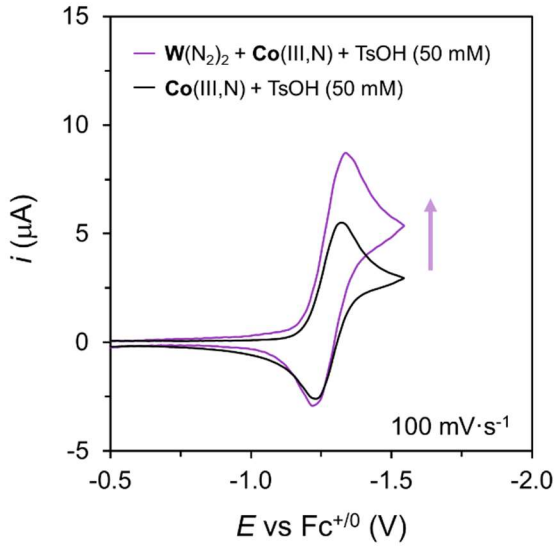

Figure S67. CVs at 100 $mV \cdot s^{-1}$ of a 0.2 M [TBA][BF_4] THF solution containing 0.5 mM **Co**(III,N)$^+$ and 50 mM TsOH with (purple trace) and without (black trace) 0.5 mM **W**(N_2). These results show the increase in the current associated with the reduction of **Co**(III,NH)$^{2+}$ to **Co**(II,NH)$^+$, consistent with tandem electrocatalysis.

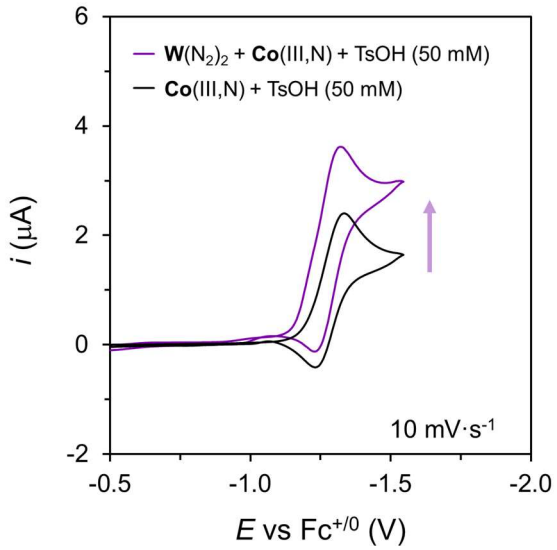

Figure S68. CVs at 10 $mV \cdot s^{-1}$ of a 0.2 M [TBA][BF_4] THF solution containing 0.5 mM **Co**(III,N)$^+$ and 50 mM TsOH with (purple trace) and without (black trace) 0.5 mM **W**(N_2). These results show an increase in the current associated with the reduction of **Co**(III,NH)$^{2+}$ to **Co**(II,NH)$^+$, consistent with tandem electrocatalysis.

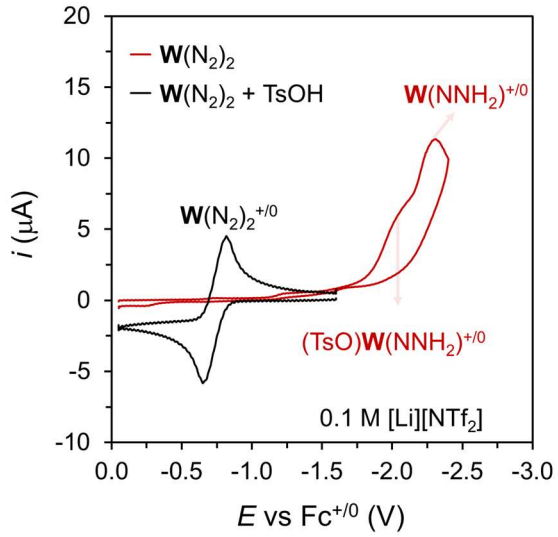

Figure S69. CV at 100 $mV \cdot s^{-1}$ of a 0.1 M [Li][NTf_2] THF solution containing 0.5 mM **W**(N_2) before (black trace) and after (red trace) addition of 2 equiv of TsOH, showing the formation of (OTs)**W**(NNH_2)$^+$.

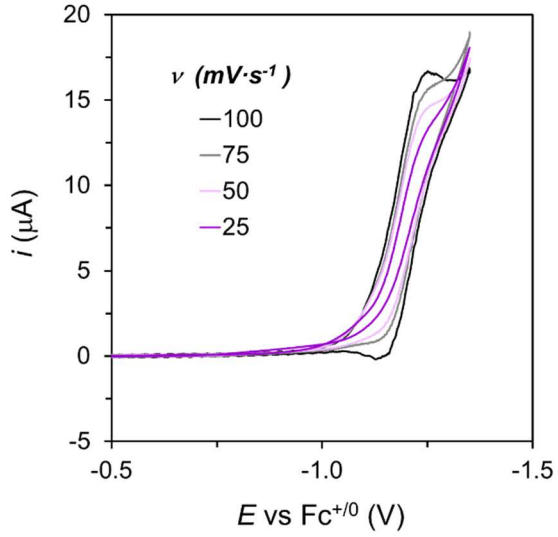

Figure S70. Variable scan rates CVs of a 0.1 M [Li][NTf_2] THF solution containing 0.5 mM **Co**(III,N)$^+$, 0.5 mM **W**(N_2) and 50 mM TsOH, showing an irreversible electrocatalytic response as compared to the one electron wave of **Co**(III,NH)$^+$. The irreversibility increases as the scan rate decreases.

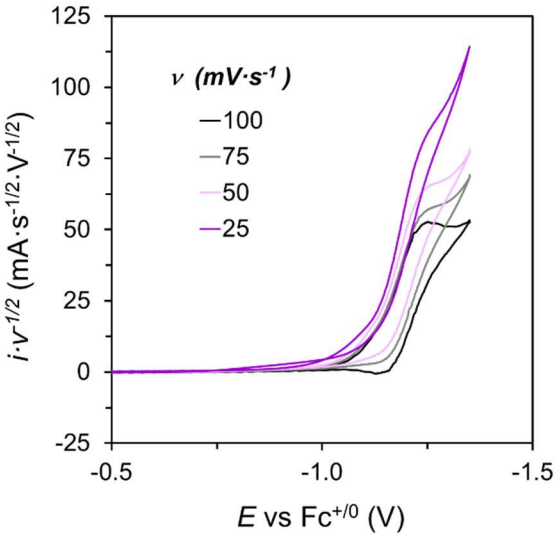

Figure S71. CVs normalized by the scan rate of a 0.1 M [Li][NTf_2] THF solution containing 0.5 mM **Co**(III,N)$^+$, 0.5 mM **W**(N_2) and 50 mM TsOH. These results show that at slower scan rates the reversibility decreases and the normalized current increases, consistent with a catalytic process coupled to the reduction of in situ generated **Co**(III,NH)$^{2+}$ to **Co**(II,NH)$^+$.

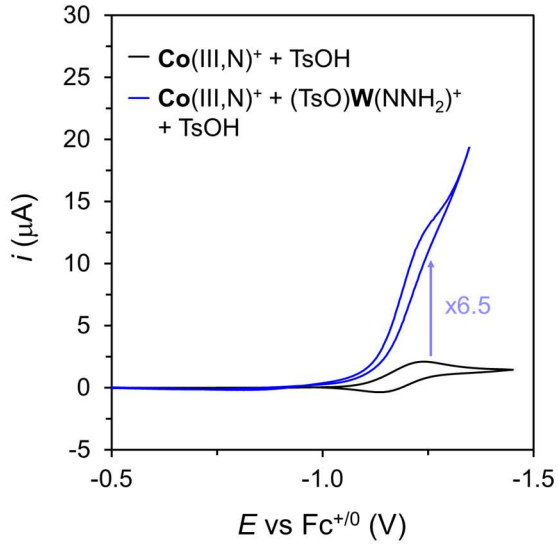

Figure S72. CVs of a THF solution containing 0.1 M [Li][NTf_2], 50 mM TsOH and 0.5 mM Co(III,N)$^+$ with (blue trace) and without (black trace) 0.5 mM (TsO)W(NNH_2)$^+$. CVs were performed at 25 mV·s^{-1} with a BDD working electrode.

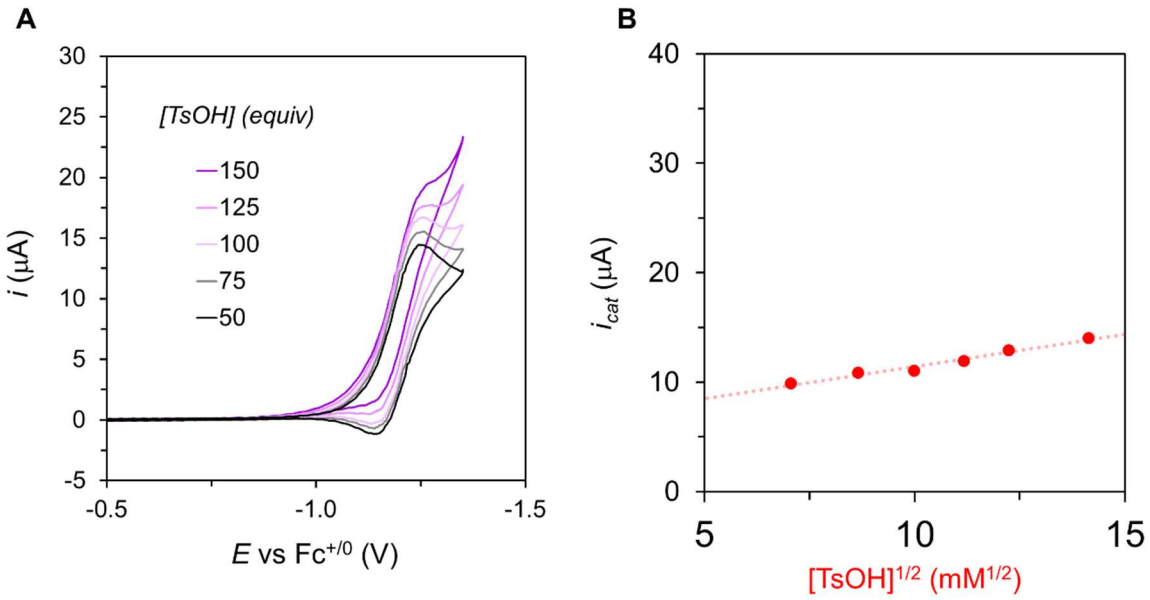

Figure S73. (**A**) CVs at 100 $mV \cdot s^{-1}$ of a 0.1 M [Li][NTf_2] THF solution containing 0.5 mM **Co**(III,N)$^+$, 0.5 mM **W**(N_2) and increasing concentrations of TsOH, evidencing a partial positive order in acid for the electrocatalytic process. (**B**) Dependence of the catalytic current extracted from background corrected CVs with the concentration of TsOH, reflecting the partial positive order in acid of the electrocatalytic process.

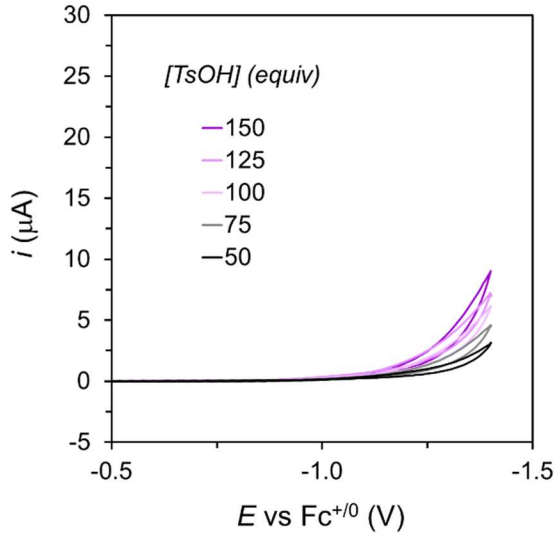

Figure S74. Background CVs at 100 $mV \cdot s^{-1}$ of a 0.1 M [Li][NTf_2] THF solution containing increasing concentrations of TsOH, showing an increase in the background HER electrocatalysis mediated by the electrode.

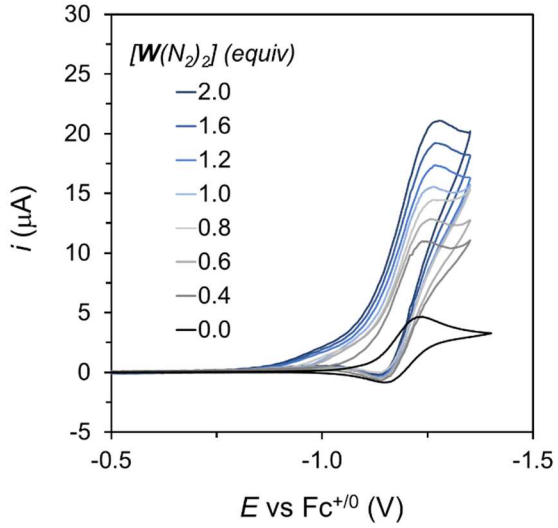

Figure S75. CVs at 100 mV·s^{-1} of a 0.1 M [Li][NTf$_2$] THF solution containing 0.5 mM **Co**(III,N)$^+$, 50 mM TsOH and increasing concentrations of **W**(N$_2$), evidencing a partial positive order in **W**(N$_2$) for the electrocatalytic process.

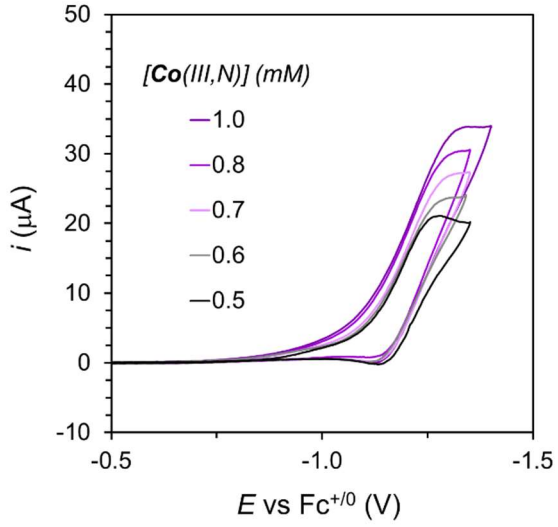

Figure S76. CVs at 100 mV·s^{-1} of a 0.1 M [Li][NTf$_2$] THF solution containing 0.5 mM **W**(N$_2$), 50 mM TsOH and increasing concentrations of **Co**(III,N)$^+$, evidencing a partial positive order in **Co**(III,N)$^+$ for the electrocatalytic process.

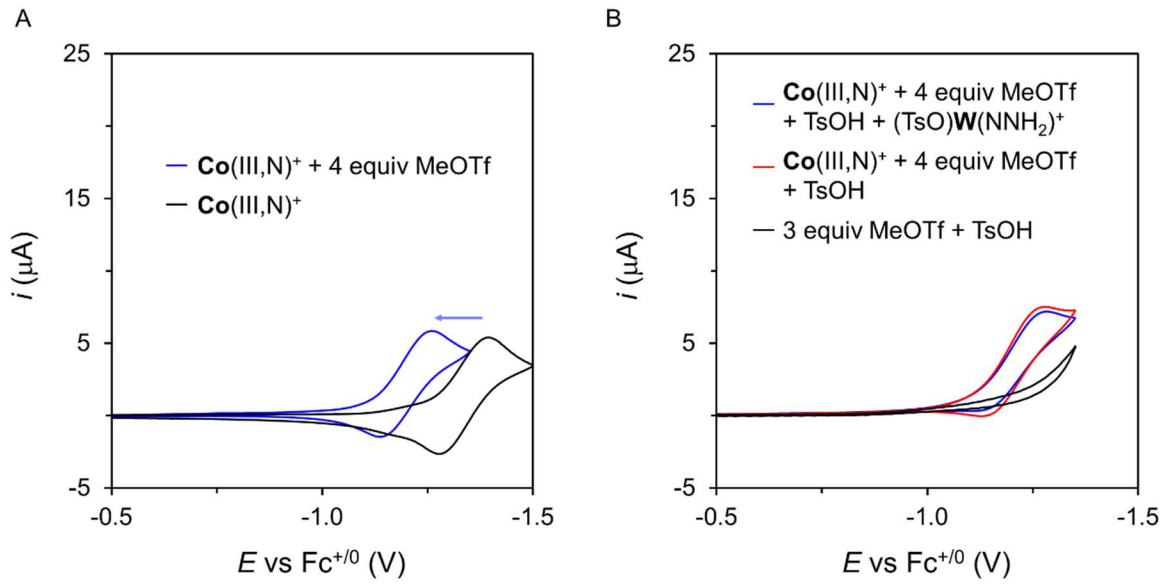

Figure S77. (A) CVs of a THF solution containing 0.1 M [Li][NTf_2] and 0.5 mM $Co(III,N)^+$ with (blue trace) and without (black trace) 4 of equiv MeOTf. (B) CVs of a THF solution containing 0.1 M [Li][NTf_2], 0.5 mM $Co(III,N)^+$ 4 of equiv MeOTf and 100 equiv of TsOH with (blue trace) and without (red trace) 0.5mM $(TsO)W(NNH_2)^+$; the black trace shows the background reduction of MeOTf in the presence of TsOH. CVs performed at 100 $mV \cdot s^{-1}$ with a BDD working electrode.

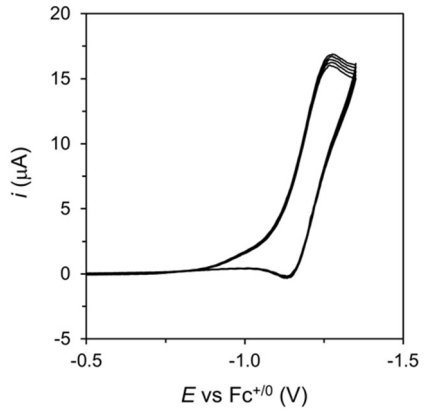

Figure S78. Consecutive scans from a CV of a THF solution containing 0.1 M [Li][NTf_2], 50 mM TsOH 0.5 mM $Co(III,N)^+$; and 0.5 mM $(TsO)W(NNH_2)^+$ at 100 $mV \cdot s^{-1}$ on a BDD working electrode.

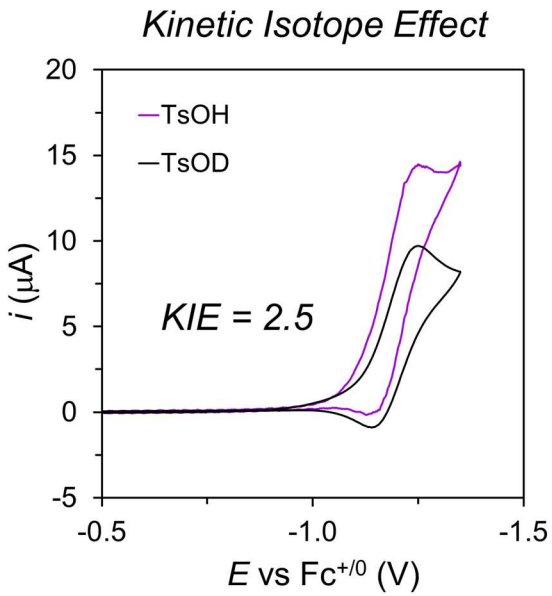

Figure S79. CV of 0.5 mM **Co**(III,N)$^{+}$/(TsO)**W**(NNH$_2$)$^{+}$ with either 50 mM TsOH (purple) or TsOD (black), performed at 100 mV·s^{-1} in 0.1 M [Li][NTf$_2$] THF solution using a BDD disk as the working electrode, Pt disk as the counter electrode and Ag/AgOTf (5mM) as the reference electrode.

S12. Rotating Ring Disk Electrode (RRDE) experiment:

To confirm the viability of the RRDE experiment a series of linear sweep voltammograms (LSVs) were performed (Figure S81A). LSVs of the electrolyte with the Pt ring electrode in the presence of added NH_4OTf show an oxidative feature at 0.5 V compared to a LSV of the blank electrolyte, demonstrating that NH_4^+ can be oxidized at this (or higher) potentials. A further LSV with added $Co(III,N)^+$ and $W(N_2)_2$ (Figure S81A, blue trace) show some oxidative features that plateau at 0.2 V. Therefore, at potentials below 0.3 V, only Co- and W-based intermediates will be oxidized at the Pt ring, and at potentials above 0.5 V ammonia will also be oxidized. In the RRDE experiment a LSV is performed at the glassy carbon (GC) disk electrode that is surrounded by the Pt ring electrode. Thus, by scanning reductively at the GC disk and monitoring the current at the Pt electrode either at 0.3 V or at 0.8 V, we can detect if NH_4^+ is formed on the LSV time scale. In LSV experiments at slow scan rate (10 $mV \cdot s^{-1}$), increased current is observed at the Pt electrode when it is held at 0.8 V vs 0.3 V starting from a potential of -1.2 V at the GC disk. This is consistent with NH_3 formation at the electrode on the LSV time scale mediated by Co and W.

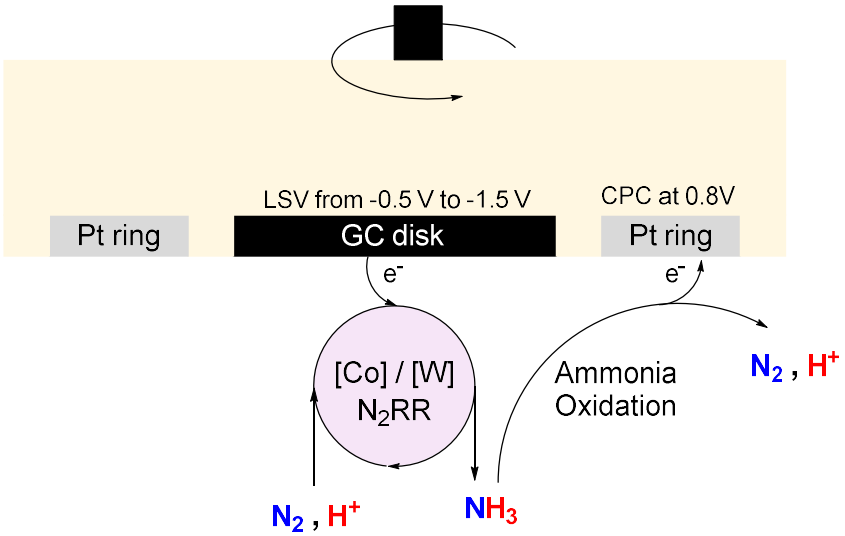

Figure S80. Schematic representation of the rotating ring disk electrode experiment for the detection of electrochemically generated ammonia.

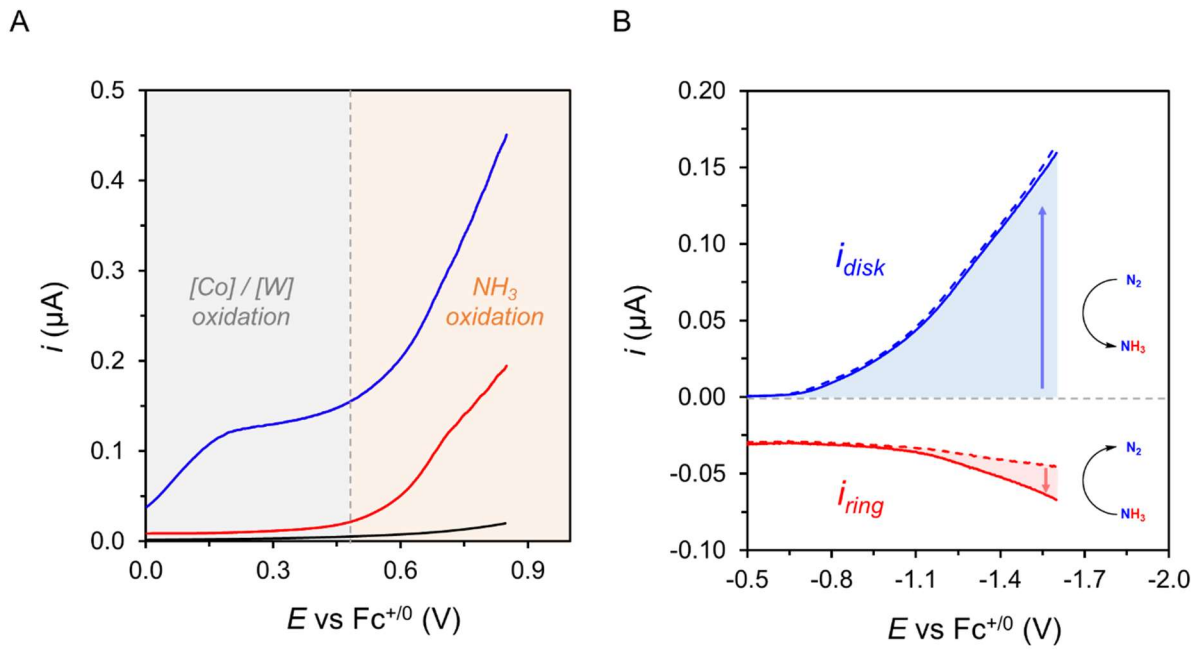

Figure S81. (A) Linear sweep voltammograms (LSVs) performed at the Pt ring electrode of THF solution containing 0.1 M [Li][NTf_2] and 50 mM TsOH (black trace) and with addition of 5 mM of NH_4OTf first (red trace) and 0.5 mM $Co(III,N)^+$ and $(TsO)W(NNH_2)^+$ second (blue trace). (B) RRDE experiment performed using a THF solution containing 0.1 M [Li][NTf_2], 50 mM TsOH, 0.5 mM $Co(III,N)^+$, and 0.5 mM $(TsO)W(NNH_2)^+$ at 10 $mV \cdot s^{-1}$. The plot shows the LSV performed at the disk electrode (blue traces) and current monitored at the Pt ring electrode (red traces) upon applying a reduction potential at the latter of 0.3 V (dashed line) or 0.8 V (solid line).

S13. Nature of the PCET step:

A proton-coupled electron transfer (PCET) step, such as that occurring between **Co**(II,NH)$^+$ and **W**(NNH$_2$)$^+$ species, can follow different pathways: electron transfer followed by proton transfer (ET-PT), proton transfer followed by electron transfer (PT-ET) or concerted proton-electron transfer (CPET). As extensively discussed in the literature, reliable elucidation of the degree of concertedness of PCET steps is challenging. However, several studies have used available data and associated arguments to point to a specific pathway.[31,32,33]

S12.1. Thermodynamic exclusionary arguments

One of the most common approaches to excluding stepwise ET-PT or PT-ET pathways, as compared to a concerted PCET step (i.e., CPET) derives from their differing thermodynamic requirements. At the same time that an overall CPET step can be thermoneutral or downhill, the initial ET or PT steps can be significantly uphill. In such cases, the uphill nature of the initial ET or PT (k_1) means that the backreaction (k_{-1}) would be facile. By evaluating the observed kinetic rate of the overall process (k_{PCET}), a physically meaningful value for the backreaction (k_{-1}), or lack thereof, can be used to evaluate the physical meaningfulness of a stepwise process.

Calculation of k_{PCET} based on UV-vis kinetics:

We have identified the PCET step between **Co**(II,NH)$^+$ and (TsO)**W**(NNH$_2$)$^+$ to be a rate determining step in the electrocatalytic process. We have calculated a value of k_{PCET} for this reaction based on UV-vis kinetics by monitoring the decay of the band at 580 nm, associated with **Co**(II,NH)$^+$, under pseudo first order conditions using excess of (TsO)**W**(NNH$_2$)$^+$ and TsOH (Figure S82). These experiments have been performed at 0 ºC for an accurate evaluation of the kinetic data, as well as to minimize the influence of off-path bimolecular **Co**(II,NH)$^+$ decay to form H$_2$. These data thus represent a lower limit for the value of k_{PCET} (and in turn a lower limit for the forward, k_1, and backreaction, k_{-1}). Moreover, to validate that the chemical reaction is zeroth order in acid, these experiments have been performed at different acid concentrations. The data are fully consistent with the measured rate k_{PCET} representing only the PCET process between **Co**(II,NH)$^+$ and **W**(NNH$_2$)$^+$. The observed rate of k_{PCET} is 8.4 $M^{-1}\cdot s^{-1}$ at 0 ºC. This rate is significantly enhanced by the addition of electrolyte, as expected for a reaction in a low-dielectric medium between two electrostatically-repulsed, positively-charged moieties. Thus, a similar kinetic experiment performed in the presence of 100 equiv. of [Li][NTf$_2$] provides a significantly larger k_{PCET} of 93.3 $M^{-1}\cdot s^{-1}$ (Figure S83). The latter rate still represents a lower limit, because the electrolyte concentration and the temperature remain lower than that used in the electrocatalytic set-up. Nevertheless, these values correlate well with the approximated value obtained from CV experiments (*vide infra*).

Calculation of k_{PCET} based on CV experiments:

An estimated kinetic rate for the PCET step between **Co**(II,NH)$^+$ and (TsO)**W**(NNH$_2$)$^+$ can also be extracted from the CV experiments at different scan rates using similar conditions to those represented in Fig. 3b (Figure S84). The wave at −1.2 V vs $Fc^{+/0}$ corresponding to the reduction of **Co**(III,NH)$^{2+}$ to **Co**(II,NH)$^+$ is followed by a chemical step involving the PCET reaction to reduce (TsO)**W**(NNH$_2$)$^+$ and regenerate **Co**(III,N)$^+$. Therefore, this process can be modelled as an EC mechanism where E stands for electron transfer and C for chemical reaction (**Eq. S9**).[34] The plot of the peak potential versus the ln(1/ν) at slow scan rates (20-5 $mV\cdot s^{-1}$) shows a slope of around

0.011, close to the theoretical value of 0.012 corresponding to pure kinetic control. In this case, the value of the observed kinetic constant $k_{obs} = k_{PCET}[W]$ can be extracted from the intercept of the linear fit, providing a value of 498 $M^{-1}\cdot s^{-1}$.[21] This value is about a factor of 5 larger than that discussed above using electrolyte at 0 ºC via the UV-vis experiments, and given the different ionic strengths and temperature used, lends confidence to our estimate for k_{PCET} being of the order ≈ 10^2 – 10^3 $M^{-1}\cdot s^{-1}$ during electrocatalysis at room temperature.

$$E_p = E^0 - 0.78\frac{RT}{F} + \frac{RT}{2F}\ln\left(\frac{RT}{F}\frac{k_{obs}}{\nu}\right) \quad \textbf{(Eq. 9)}$$

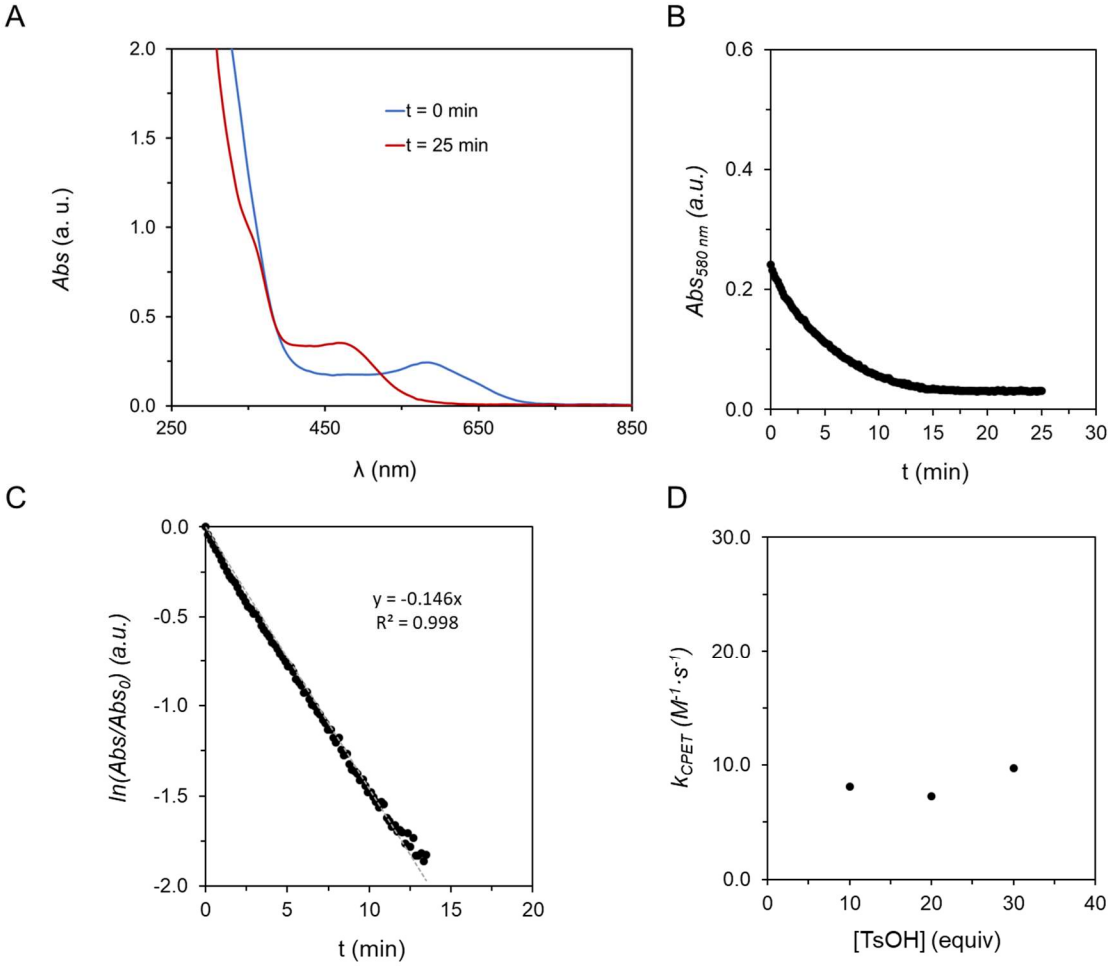

Figure S82. (A) UV-vis spectra of a THF solution containing 0.05 mM **Co**(II,N), 5 equiv of (TsO)**W**$(NNH_2)^+$ and 30 equiv of TsOH at 0 and 25 min after the addition of **Co**(II,N). (B) Decay of the absorbance band at 580 nm associated to **Co**$(II,NH)^+$. (C) Pseudo first order plot for the calculation of k_{PCET}. (D) Plot of the k_{PCET} calculated at different concentrations of TsOH showing the zeroth order dependence of this reaction on acid concentration.

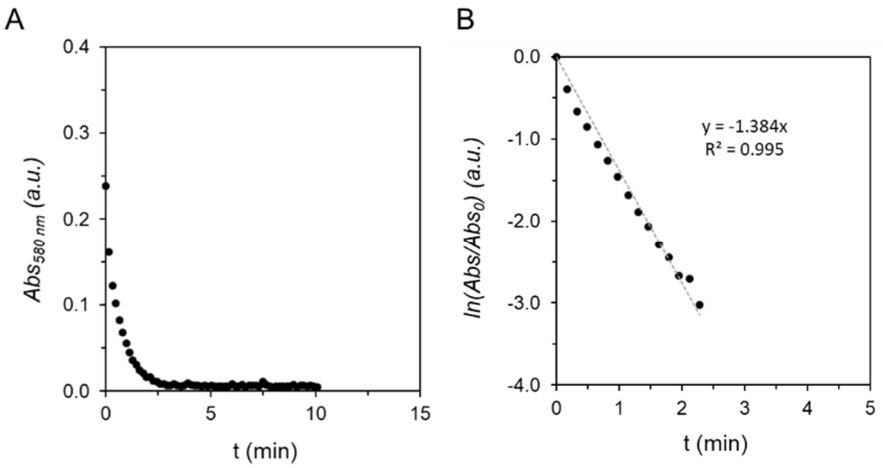

Figure S83. (A) Decay of the absorbance at 580 nm corresponding to **Co**(II,NH)$^+$ in a solution containing 0.05 mM **Co**(II,N), 5 equiv of (TsO)**W**(NNH_2)$^+$, 10 equiv of TsOH and 100 equiv of [Li][NTf_2]. (B) Pseudo first order plot for the calculation of k_{PCET}.

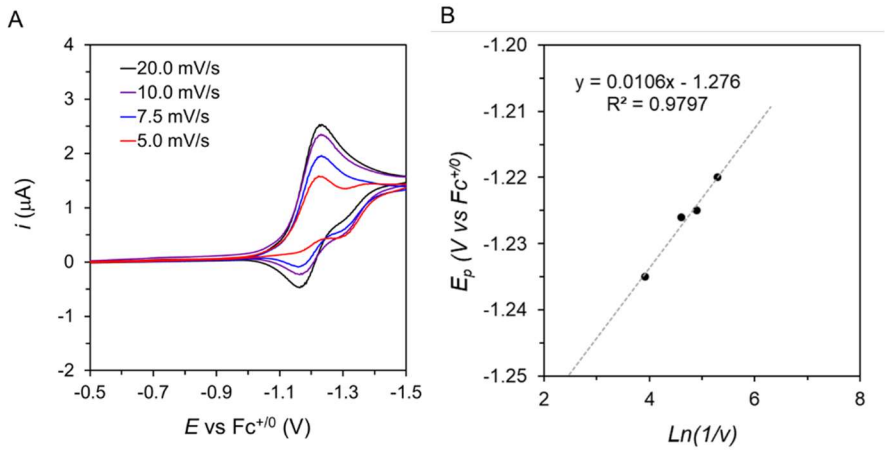

Figure S84. (A) Cyclic voltammetry experiments at different scan rates of a THF solution containing 0.5 mM **Co**(II,NH)$^+$/(TsO)**W**(NNH_2)$^+$ and 0.1 M [Li][NTf_2]. (B) Plot of the cathodic peak potential vs the ln(1/v) for the calculation of k_{PCET}.

Calculation of upper limit of pK_a for (TsO)W(NNH_2)$^+$:

(TsO)**W**(NNH_2)$^+$ has been shown in the literature to be stable to strong acids such as HBr.[35] In order to stablish an upper limit for its pK_a we have studied this complex in the presence of excess triflic acid (TfOH, pK_a(MeCN) = 0.7) using UV-vis and ^{31}P NMR spectroscopy. The complex is stable to protonation under these conditions; expectedly, substitution of the apical TsO^- ligand by a TfO^- occurs, as confirmed by comparison of spectra obtained via the protonation of **W**(N_2)$_2$ by tosic acid in the presence of excess [TBA][OTf].

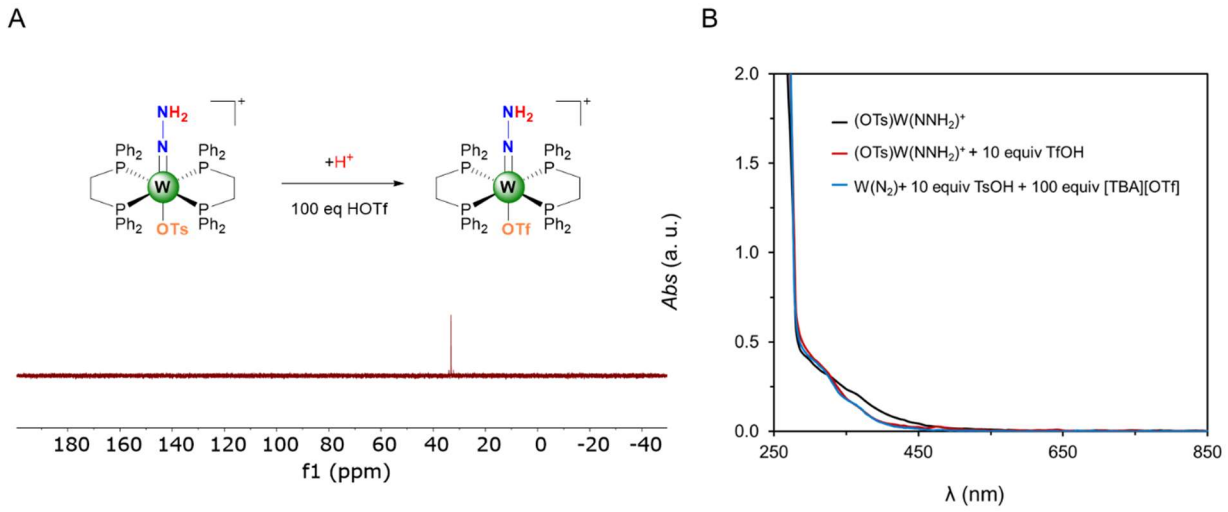

Figure S85. (A) ^{31}P NMR of a THF solution containing 0.5 mM (TsO)**W**$(NNH_2)^+$ and 10 equiv. of TfOH. (B) UV-vis spectra of a solution containing 0.05 mM (TsO)**W**$(NNH_2)^+$ with and without 10 equiv. of TfOH compared to a solution containing 0.05 **W**(N_2), 10 equiv TsOH and 100 equiv. [TBA][OTf].

Thermodynamics of ET-PT pathway:
The relevant redox potentials for the cobalt mediator and (TsO)**W**$(NNH_2)^+$, obtained from CV and DPV experiments, are −1.2 V and −1.9 V, respectively, providing a ΔG^o_{ET} = 0.7 eV. This value involves an equilibrium constant (K) for an initial ET step (K_{ET}): $K_{ET} = k_{ET}/k_{-ET} \approx 10^{-12}$. Considering a rate limiting ET process, then $k_{ET} = k_{PCET}$. Assuming a conservative value of $k_{PCET} \approx 10^2$ $M^{-1}\cdot s^{-1}$ (see above), a value for $k_{-1(ET)}$ of at least 10^{14} $M^{-1}\cdot s^{-1}$ is required, which is significantly higher than the diffusion-limited rate and therefore not physically meaningful. Thus we disfavor an ET-first pathway (ET-PT). Considering instead a PT-ET mechanism leads to similar conclusions. In this case, $\Delta G^o_{PT} > 14.1$ kcal/mol based on the pK_a values of both species, resulting in $K_{PT} = k_{PT}/k_{-PT} \approx 5\cdot 10^{-11}$. A rate limiting PT step would involve a $k_{-1(PT)}$ of at least 10^{13} $M^{-1}\cdot s^{-1}$, which again is physically not meaningful under diffusion-controlled conditions.

The above considerations are relevant to a diffusion-limited reaction. However, an alternative pre-equilibrium pathway may be possible. In such a case the pre-association of the reactants and post-association of the products involved in the PCET process becomes more challenging to analyze, due to the unknown stability of the W-product of the PCET reaction; estimate of an equilibrium constant for the PCET step is then more difficult. Still, using an upper bound for the equilibrium constant for a hypothetical (not experimentally observed under the conditions studied) pre-associated complex of ≈ 1 M^{-1},[32,36] and a conservative equilibrium constant for the reaction of **Co**(II,NH)$^+$ and (TsO)**W**$(NNH_2)^+$ of ≈ 1 M^{-1}, a K for the initial step is required to be ≈ 10^{-11}. This value assumes an upper limit for k_{-ET} or k_{-PT} of 10^{13} $M^{-1}\cdot s^{-1}$ and the k_{PCET} previously calculated. This is an order of magnitude higher than the K_{ET} calculated based on the ΔG^o_{ET}. However, it is similar to the K_{PT} calculated from ΔG^o_{PT}. Therefore, a PT-ET mechanism relying on pre-association of **Co**(II,NH)$^+$ and (TsO)**W**$(NNH_2)^+$ cannot be summarily rejected based on thermodynamic/kinetic arguments. Still, our intuition is that such a mechanism will be disfavored due to difficulty with respect to association of the reactants. Such a pre-equilibrium step would

likely rely on favorable intermolecular hydrogen bonding interactions, which we anticipate will be disfavored due to the significant difference in the respective pK_a values of **Co**(II,NH)$^+$ and (TsO)**W**$(NNH_2)^+$ (11 versus < 0.7); the positive charge of both species should also lead to electrostatic repulsion. As a final point of note, the conservative assumptions made in these calculations provide only a lower-limit value of k_{PCET}. Moreover, although there are exceptions,[37] equilibrium protonation reactions typically feature low KIE values (< 2),[32] smaller than that observed in this work (> 2, see below). Also, protonation reactions tend to occur at very high rates when involving electronegative elements (such as N),[38] disfavoring rate limiting proton transfers in such cases, again arguing against a rate-determining PT in the present system.

S.12.2. Kinetic isotope effect:

We have further determined a KIE for the chemical PCET reaction between **Co**(II,NH)$^+$ and (TsO)**W**$(NNH_2)^+$ via UV-vis kinetics to disentangle any potential effect of rate limiting proton transfer steps during catalysis. The reactions were performed in the presence of either TsOH and (TsO)**W**$(NNH_2)^+$ or TsOD and (TsO)**W**$(NND_2)^+$. The results shown in Figure S86 reveal a KIE value of 2.7, similar to but slightly higher than the one obtained from CV under electrocatalytic conditions (2.5), lending further support to the use of this stoichiometric reaction as a proxy for the rate of the overall catalysis under electrocatalytic conditions. While these KIE values are consistent with a concerted PCET process, they do not demand one.

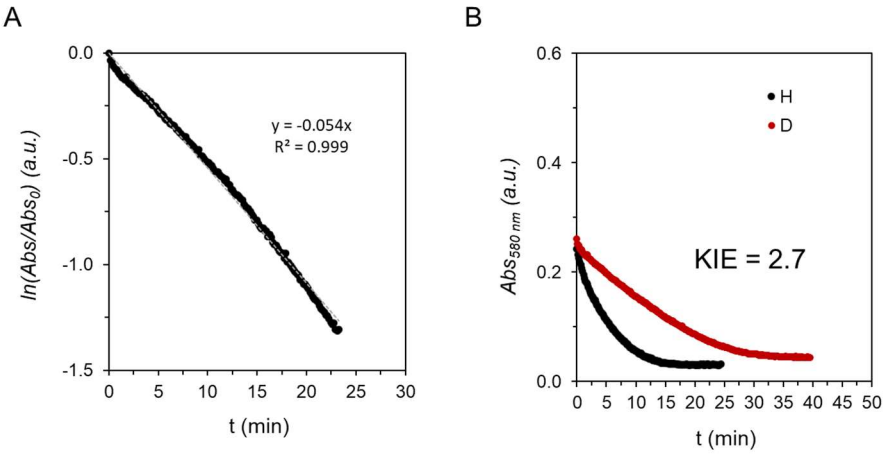

Figure S86. (A) Decay of the absorbance at 580 nm corresponding to **Co**(II,NH)$^+$ in a solution containing 0.05 mM **Co**(II,N) and either 5 equiv of (TsO)**W**$(NNH_2)^+$ and 30 equiv of TsOH or 5 equiv of (TsO)**W**$(NND_2)^+$ and 30 equiv of TsOD. (B) Pseudo first order plot for the calculation of k_{PCET} in deuterated conditions.

To conclude this section, while we currently favor a concerted PCET step playing a role in the operative mechanism of the N_2RR electrocatalysis described in this study, consistent with simpler electrocatalytic reduction reactions (e.g., acetophenone reduction) using this same cobalt mediator,[1] we acknowledge an inherent degree of uncertainty in such an assignment. We have provided similar data and associated thermodynamic/kinetic arguments akin to those used by others in support of a CPET assignment,[31,32,33] but future studies involving theory and possibly additional experiments (e.g., variation of the driving force as a function of k_{PCET}), beyond the scope of this work, are warranted to further test our working CPET model.

S14. Electrocatalysis with N_2RR catalysts:

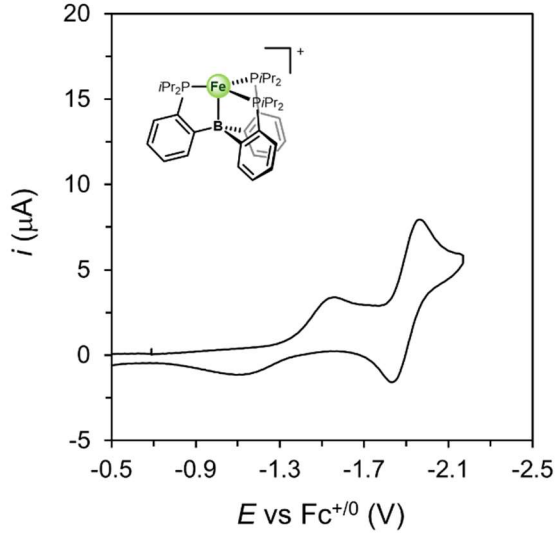

Figure S87. CV at 100 $mV \cdot s^{-1}$ of a 0.1 M [Li][NTf_2] THF solution containing 0.5 mM [(TPB)Fe][$BAr^F{}_4$], showing the subsequent, reversible, one-electron reduction to **Fe**(N_2) (complex **6)** and **Fe**$(N_2)^-$, at around −1.3 V and −2 V vs $Fc^{+/0}$, respectively.

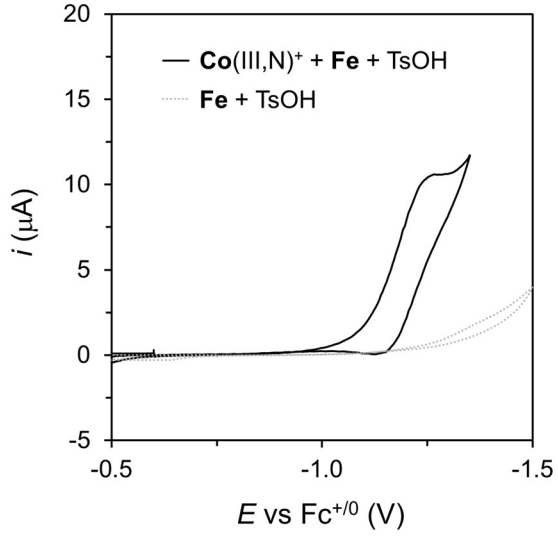

Figure S88. CV at 100 $mV \cdot s^{-1}$ of a 0.1 M [Li][NTf_2] THF solution containing 0.5 mM [(TPB)Fe][$BAr^F{}_4$] and 50 mM TsOH with (black trace) and without (gray trace) 0.5 mM **Co**$(III,N)^+$.

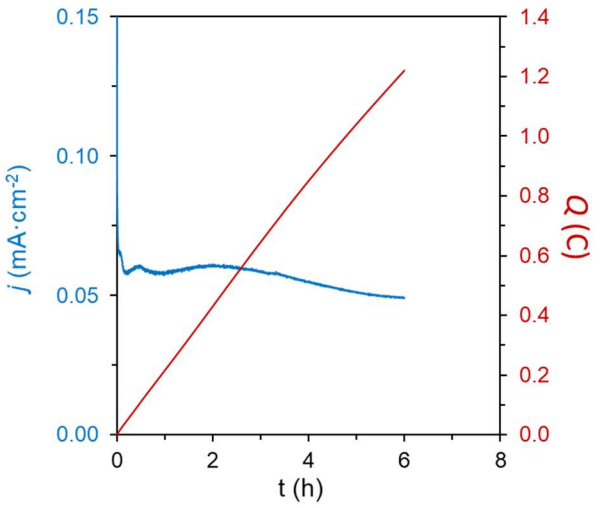

Figure S89. Current and charge profile for a CPC at −1.35 V vs $Fc^{+/0}$ in 0.1 M [Li][NTf_2] DME solution containing 0.05 mM **Co**(III,N)$^+$, 0.05 mM [(TPB)Fe][$BAr^F{}_4$] and 5 mM TsOH, using a BDD plate working electrode.

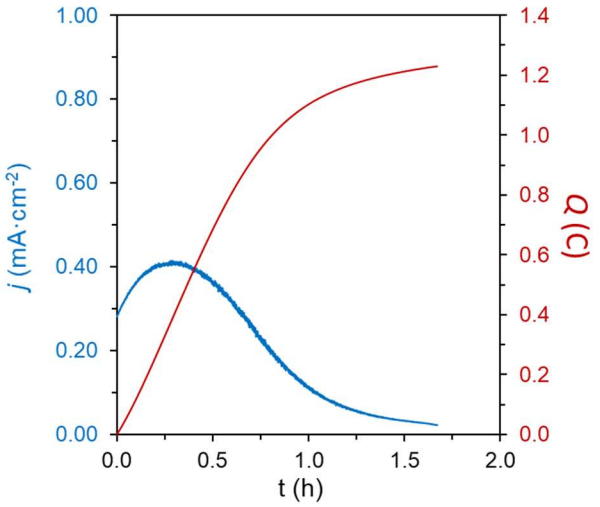

Figure S90. Current and charge profile for a CPC at −1.45 V vs $Fc^{+/0}$ in 0.1 M [Li][NTf_2] DME solution containing 0.05 mM **Co**(III,N)$^+$, 0.05 mM [(TPB)Fe][$BAr^F{}_4$] and 5 mM TsOH, using a BDD plate working electrode.

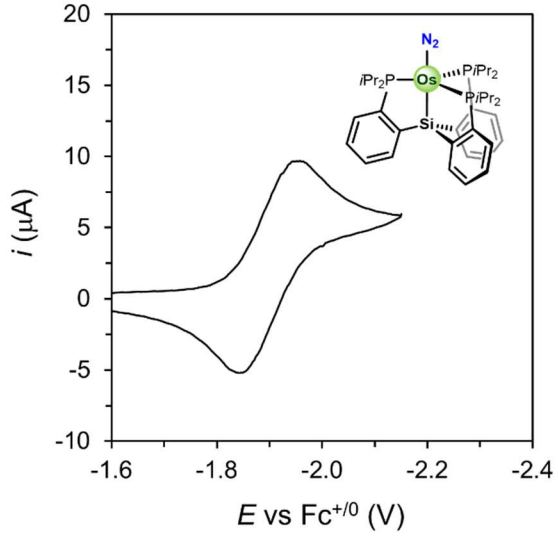

Figure S91. CV at 100 mV·s^{-1} of a 0.1 M [Li][NTf_2] THF solution containing 0.5 mM **Os**(N_2) complex **5** showing the reversible, one-electron reduction to **Os**(N_2)$^-$ at around −1.9 V vs $Fc^{+/0}$.

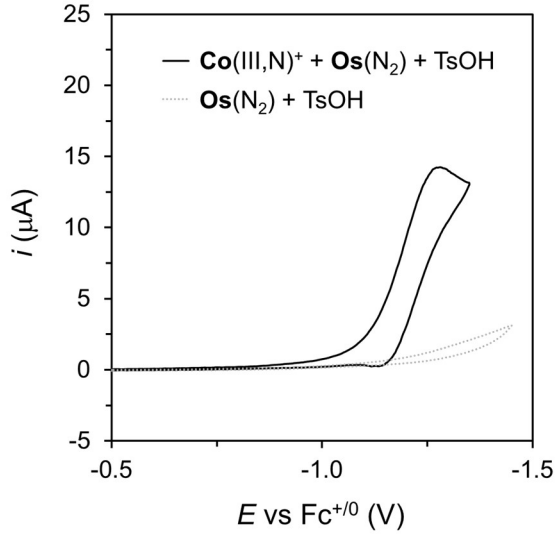

Figure S92. CV at 100 mV·s^{-1} of a 0.1 M [Li][NTf_2] THF solution containing 0.5 mM **Os**(N_2) and 50 mM TsOH with (black trace) and without (gray trace) 0.5 mM **Co**(III,N)$^+$.

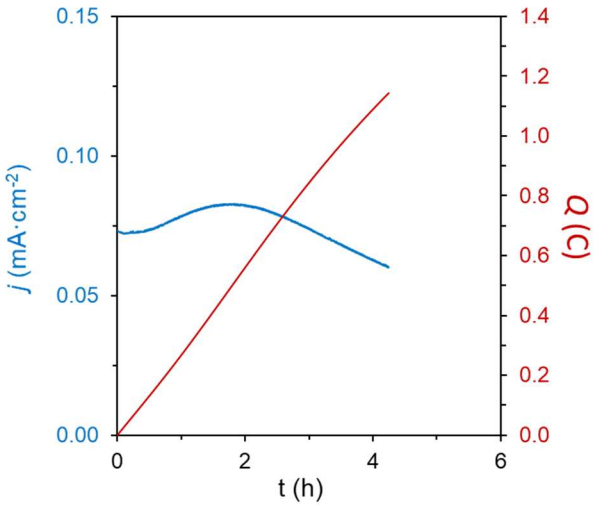

Figure S93. Current and charge profile for a CPC at −1.35 V vs $Fc^{+/0}$ in 0.1 M [Li][NTf_2] DME solution containing 0.05 mM **Co**(III,N)$^+$, 0.05 mM **Os**(N_2) and 5 mM TsOH, using a BDD plate working electrode.

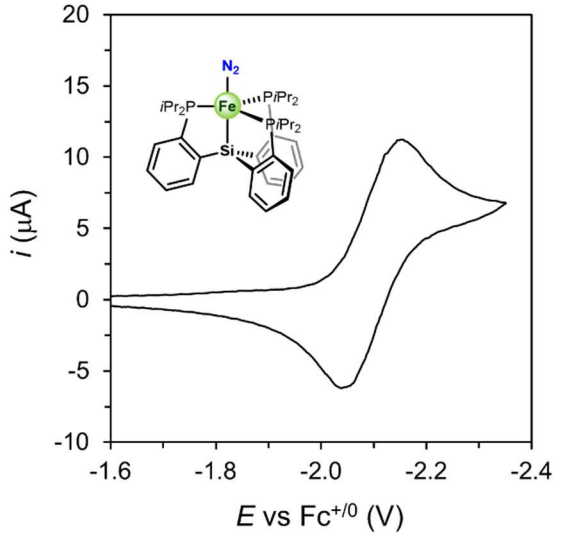

Figure S94. CV at 100 $mV \cdot s^{-1}$ of a 0.1 M [Li][NTf_2] THF solution containing 0.5 mM (SiP_3)Fe(N_2) complex **7** showing the reversible, one-electron reduction to (SiP_3)Fe(N_2)$^-$ at around −2.1 V vs $Fc^{+/0}$.

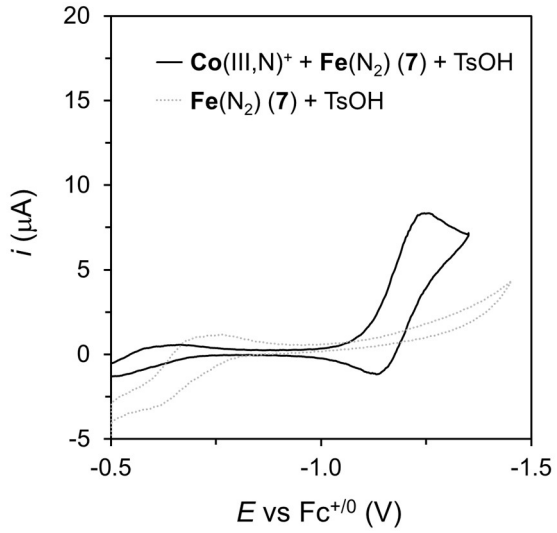

Figure S95. CV at 100 $mV \cdot s^{-1}$ of a 0.1 M [Li][NTf_2] THF solution containing 0.5 mM (SiP_3)Fe(N_2) and 50 mM TsOH with (black trace) and without (gray trace) 0.5 mM **Co**(III,N)$^+$.

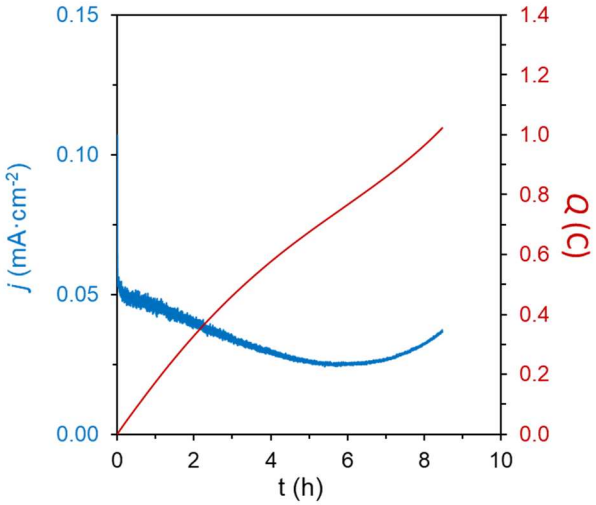

Figure S96. Current and charge profile for a CPC at −1.35 V vs $Fc^{+/0}$ in 0.1 M [Li][NTf_2] DME solution containing 0.05 mM **Co**(III,N)$^+$, 0.05 mM **Fe**(N_2) and 5 mM TsOH, using a BDD plate working electrode.

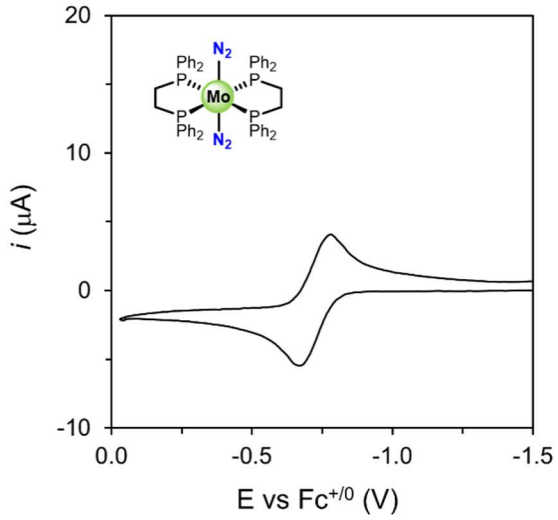

Figure S97. CV at 100 mV·s^{-1} of a 0.1 M [Li][NTf$_2$] THF solution containing 0.5 mM the **Mo**(N$_2$)$_2$ complex **1** showing a reversible, one-electron redox couple at around −0.7 V vs Fc$^{+/0}$.

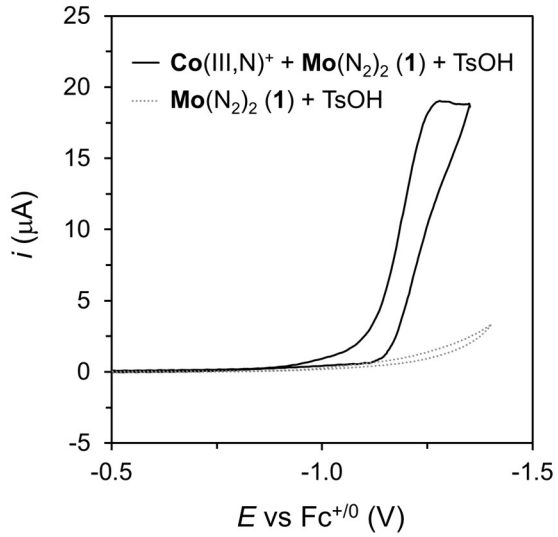

Figure S98. CV at 100 mV·s^{-1} of a 0.1 M [Li][NTf$_2$] THF solution containing 0.5 mM of the **Mo**(N$_2$)$_2$ complex **1** and 50 mM TsOH with (black trace) and without (gray trace) 0.5 mM **Co**(III,N)$^+$.

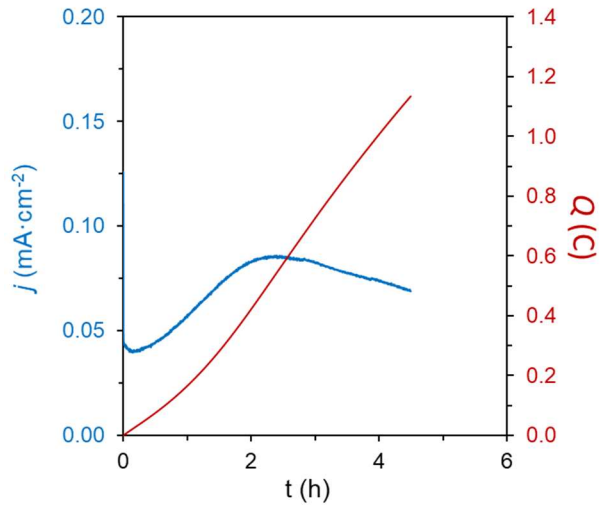

Figure S99. Current and charge profile for a CPC at −1.35 V vs $Fc^{+/0}$ in 0.1 M [Li][NTf_2] DME solution containing 0.05 mM **Co**(III,N)$^+$, 0.05 mM **Mo**(N_2)$_2$ complex **1** and 5 mM TsOH, using a BDD plate working electrode.

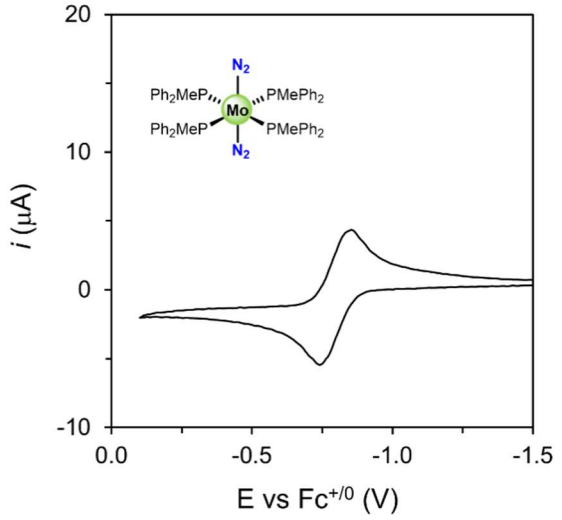

Figure S100. CV at 100 mV·s^{-1} of a 0.1 M [Li][NTf_2] THF solution containing 0.5 mM the **Mo**(N_2)$_2$ complex **2** showing a reversible, one-electron redox couple at around −0.6 V vs $Fc^{+/0}$.

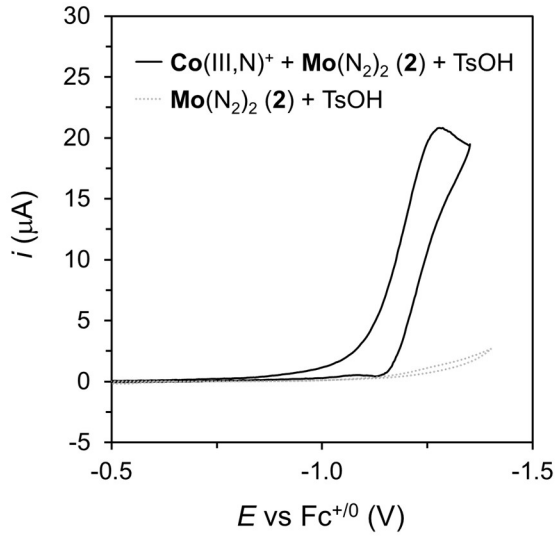

Figure S101. CV at 100 mV·s^{-1} of a 0.1 M [Li][NTf_2] THF solution containing 0.5 mM of the **Mo**(N_2)$_2$ complex **2** and 50 mM TsOH with (black trace) and without (gray trace) 0.5 mM **Co**(III,N)$^+$.

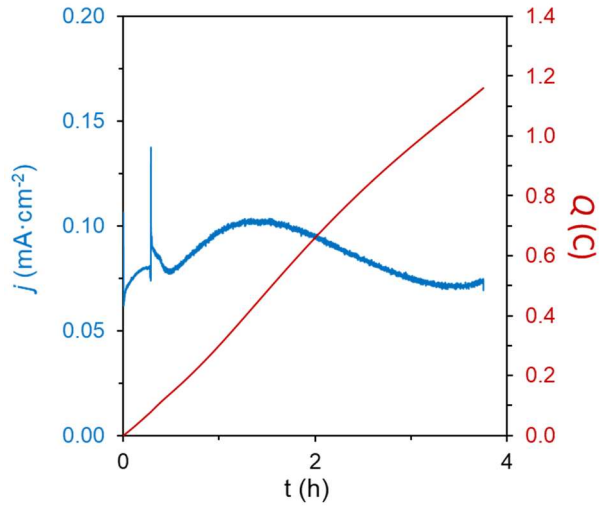

Figure S102. Current and charge profile for a CPC at −1.35 V vs $Fc^{+/0}$ in 0.1 M [Li][NTf_2] DME solution containing 0.05 mM **Co**(III,N)$^+$, 0.05 mM **Mo**(N_2)$_2$ complex **2** and 5 mM TsOH, using a BDD plate working electrode.

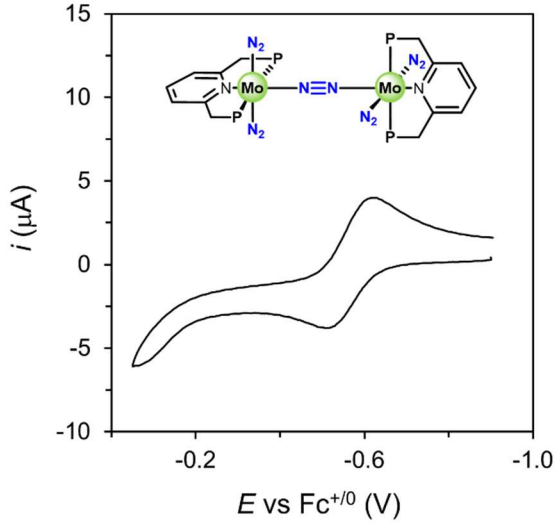

Figure S103. CV at 100 mV·s^{-1} of a 0.1 M [Li][NTf_2] THF solution containing 0.5 mM the Mo complex **3** showing a reversible, one-electron redox couple at around −0.6 V vs $Fc^{+/0}$.

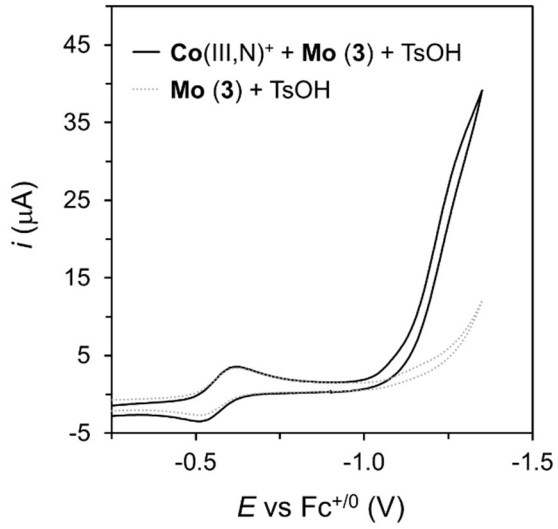

Figure S104. CV at 100 mV·s^{-1} of a 0.1 M [Li][NTf_2] THF solution containing 0.5 mM of the Mo complex **3** and 50 mM TsOH with (black trace) and without (gray trace) 0.5 mM **Co**(III,N)$^+$.

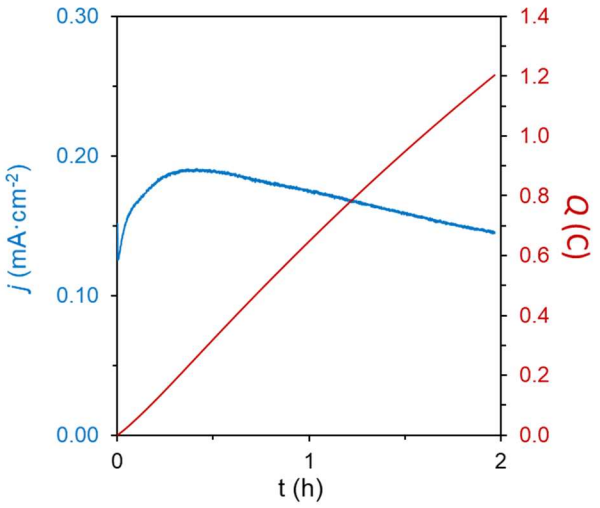

Figure S105. Current and charge profile for a CPC at −1.35 V vs $Fc^{+/0}$ in 0.1 M [Li][NTf_2] DME solution containing 0.05 mM **Co**(III,N)$^+$, 0.05 mM Mo complex **3** and 5 mM TsOH, using a BDD plate working electrode.

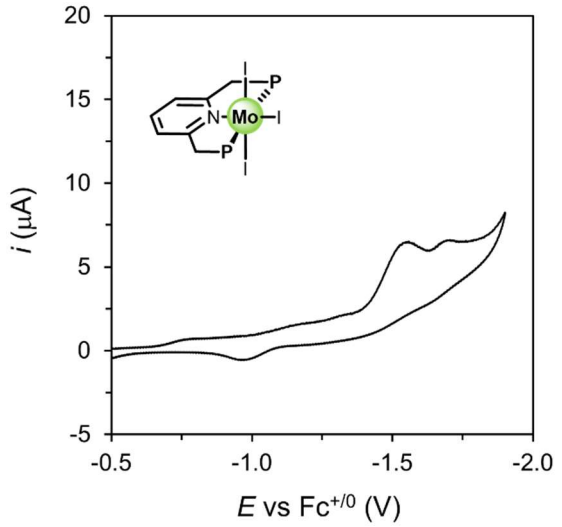

Figure S106. CV at 100 $mV \cdot s^{-1}$ of a 0.1 M [Li][NTf_2] THF solution containing 0.5 mM the Mo complex **4** showing two irreversible, one-electron reduction waves below −1.5 V vs $Fc^{+/0}$.

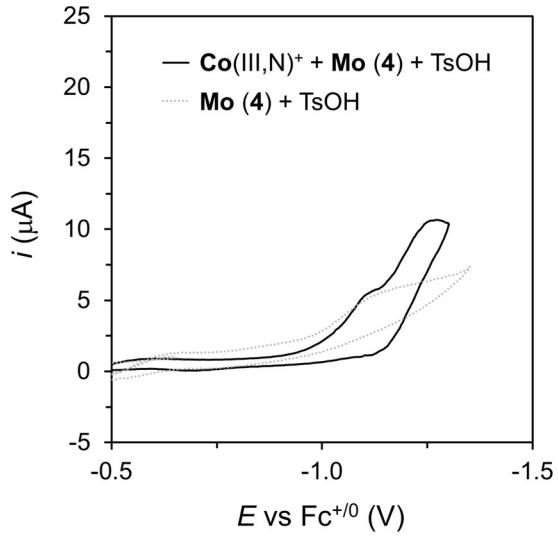

Figure S107. CV at 100 mV·s^{-1} of a 0.1 M [Li][NTf$_2$] THF solution containing 0.5 mM of the Mo complex **4** and 50 mM TsOH with (black trace) and without (gray trace) 0.5 mM **Co**(III,N)$^+$.

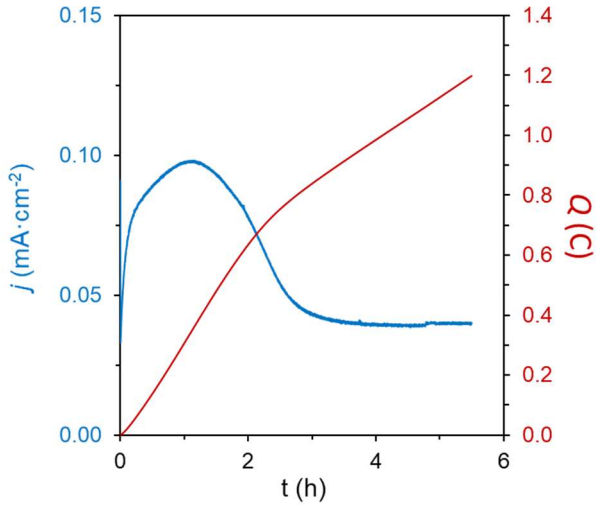

Figure S108. Current and charge profile for a CPC at −1.35 V vs Fc$^{+/0}$ in 0.1 M [Li][NTf$_2$] DME solution containing 0.05 mM **Co**(III,N)$^+$, 0.05 mM Mo complex **4** and 5 mM TsOH, using a BDD plate working electrode.

S15. References:

1. Chalkley, M. J., Garrido-Barros, P. & Peters, J. C. A molecular mediator for reductive concerted proton-electron transfers via electrocatalysis. *Science* **369**, 850–854 (2020).
2. Pickett, C. J. & Talarmin, J. Electrosynthesis of ammonia. *Nature* **317**, 652–653 (1985).
3. Lane, J. D. & Henderson, R. A. Mechanism of the reaction between trans-$[W(NNH_2)(p\text{-}MeC_6H_4SO_3)(Ph_2PCH_2CH_2PPh_2)_2]^+$ and NEt_3: the influence of the metal on the rates of proton transfer of hydrazido(2–)-ligands. *J. Chem. Soc., Dalton Trans.* 197–200 (1987).
4. Bevan, P. C., Chatt, J., Dilworth, J. R., Henderson, R. A. & Leigh, G. J. The preparation and reactions of azidobis[1,2-bis(diphenylphosphino)-ethane]nitridotungsten(IV). *J. Chem. Soc., Dalton Trans.* 821–824 (1982).
5. Becker, J. Y. & Avraham (Tsarfaty), S. Nitrogen fixation: Part III. Electrochemical reduction of hydrazido ($-NNH_2$) Mo and W complexes. Selective formation of NH_3 under mild conditions. *J. Electroanal. Chem. Interf. Electrochem.* **280**, 119–127 (1990).
6. Ning, Y., Sarjeant, A. A., Stern, C. L., Peterson, T. H. & Nguyen, S. T. One-pot synthesis of Mo^0 dinitrogen complexes possessing monodentate and multidentate phosphine ligands. *Inorg. Chem.* **51**, 3051–3058 (2012).
7. Arashiba, K., Miyake, Y. & Nishibayashi, Y. A molybdenum complex bearing PNP-type pincer ligands leads to the catalytic reduction of dinitrogen into ammonia. *Nat. Chem.* **3**, 120–125 (2010).
8. Arashiba, K. *et al.* Catalytic nitrogen fixation via direct cleavage of nitrogen–nitrogen triple bond of molecular dinitrogen under ambient reaction conditions. *Bull. Chem. Soc. Jpn.* **90**, 1111–1118 (2017).
9. Takaoka, A., Gerber, L. C. H. & Peters, J. C. Access to well-defined ruthenium(I) and osmium(I) metalloradicals. *Angew. Chem. Int. Ed.* **49**, 4088–4091 (2010).
10. Anderson, J. S., Rittle, J. & Peters, J. C. Catalytic conversion of nitrogen to ammonia by an iron model complex. *Nature* **501**, 84–7 (2013).
11. Whited, M. T., Mankad, N. P., Lee, Y. H., Oblad, P. F. & Peters, J. C. Dinitrogen complexes supported by tris(phosphino)silyl ligands. *Inorg. Chem.* **48**, 2507–2517 (2009).
12. Del Castillo, T. J., Thompson, N. B. & Peters, J. C. A synthetic single-site Fe nitrogenase: high turnover, freeze-fuench ^{57}Fe Mössbauer data, and a hydride resting state. *J. Am. Chem. Soc.* **138**, 5341–5350 (2016).
13. Brown, T. J., Weber, D., Gagné, M. R. & Widenhoefer, R. A. Mechanistic analysis of gold(I)-catalyzed intramolecular allene hydroalkoxylation reveals an off-cycle bis(gold) vinyl species and reversible C–O bond formation. *J. Am. Chem. Soc.* **134**, 9134–9137 (2012).
14. Suryanto, B. H. R. *et al.* Nitrogen reduction to ammonia at high efficiency and rates based on a phosphonium proton shuttle. *Science* **372**, 1187 (2021).
15. Hodgetts, R. Y. *et al.* Refining universal procedures for ammonium quantification via rapid ^{1}H NMR analysis for dinitrogen reduction studies. *ACS Energy Lett.* **5**, 736–741 (2020).
16. Macpherson, J. V. A practical guide to using boron doped diamond in electrochemical research. *Phys. Chem. Chem. Phys.* **17**, 2935–2949 (2015).
17. Costentin, C. & Savéant, J.-M. Multielectron, multistep molecular catalysis of electrochemical reactions: benchmarking of homogeneous catalysts. *ChemElectroChem* **1**, 1226–1236 (2014).
18. Kolen, M., Smith, W. A. & Mulder, F. M. Accelerating ^{1}H NMR detection of aqueous ammonia. *ACS Omega* **6**, 5698–5704 (2021).

19. Nielander, A. C. *et al.* A versatile method for ammonia detection in a range of relevant electrolytes via direct nuclear magnetic resonance techniques. *ACS Catal.* **9**, 5797–5802 (2019).
20. Pickett, C. J., Ryder, K. S. & Talarmin, J. Electron-transfer reactions in nitrogen fixation. Part 2. The electrosynthesis of ammonia: identification and estimation of products. *J. Chem. Soc., Dalton Trans.* **7**, 1453–1457 (1986).
21. Al-Salih, T. I. & Pickett, C. J. Electron-transfer reactions in nitrogen fixation. Part 1. The electrosynthesis of dinitrogen, hydride, isocyanide, and carbonyl complexes of molybdenum: intermediates, mechanisms, and energetics. *J. Chem. Soc., Dalton Trans.* 1255–1264 (1985).
22. Geri, J. B., Shanahan, J. P. & Szymczak, N. K. Testing the push–pull hypothesis: Lewis acid augmented N_2 activation at iron. *J. Am. Chem. Soc.* **139**, 5952–5956 (2017).
23. Bendix, J. & Bøgevig, A. Synthesis and characterization of a stable trans-dioxo tungsten(IV) complex and series of mono-oxo molybdenum(IV) and tungsten(IV) complexes. structural and electronic effects of π-bonding in trans-$[M(O)(X)(dppe)_2]^{+/0}$ systems. *Inorg. Chem.* **37**, 5992–6001 (1998).
24. Xu, K. Nonaqueous liquid electrolytes for lithium-based rechargeable batteries *Chem. Rev.* **104**, 4303–4418 (2004).
25. Andersen, S. Z. *et al*. Increasing stability, efficiency, and fundamental understanding of lithium-mediated electrochemical nitrogen reduction. *Energy Environ. Sci.* **13**, 4291-4300 (2020).
26. Low, M. J. D., Ramasubramanian, N. & Rao, V. V. S. Reactions of ammonia with porous glass surfaces. *J. Phys. Chem.* **71**, 1726-1734 (1967).
27. Lehnert, N. & Tuczek, F. The reduction pathway of end-on coordinated dinitrogen. I. Vibrational spectra of Mo/W–N_2, –NNH, and –NNH_2 complexes and quantum chemistry assisted normal coordinate analysis. *Inorg. Chem.* **38**, 1659–1670 (1999).
28. A. Henderson, R. The mechanism of formation of hydrazido(2—)- and hydrido-complexes by the reaction of dinitrogen complexes with acids in tetrahydrofuran. *J. Chem. Soc., Dalton Trans.* **0**, 917–925 (1982).
29. Kireev, N. V. *et al.* Steric and acidity control in hydrogen bonding and proton transfer to trans-$W(N_2)_2(dppe)_2$. *Inorg. Chem.* **57**, 1656–1664 (2018).
30. Chatt, J., Pearman, A. J. & Richards, R. L. Conversion of dinitrogen in its molybdenum and tungsten complexes into ammonia and possible relevance to the nitrogenase reaction. *J. Chem. Soc., Dalton Trans.*1852-1860 (1977).
31. Tyburski, R., Liu, T., Glover, S. D. & Hammarström, L. Proton-coupled electron transfer guidelines, fair and square. *J. Am. Chem. Soc.* **143**, 560-576 (2021).
32. Rhile, I. J. *et al*. Concerted proton-electron transfer in the oxidation of hydrogen-bonded phenols. *J. Am. Chem. Soc.* **128**, 6075-6088 (2006).
33. Darcy, J. W., Koronkiewicz, B., Parada, G. A. & Mayer, J. M. A continuum of proton-coupled electron transfer reactivity. Acc. *Chem. Res.* **51**, 2391-2399 (2018).
34. Costentin, C.; Saveant, J. M.́ Elements of Molecular and Biomolecular Electrochemistry: An Electrochemical Approach to Electron Transfer Chemistry, 2nd ed.; John Wiley & Sons: Hoboken, NJ, 2006
35. Chatt, J., Heath, G. A., & Richards, R. L. Diazene-N-(di-imide) and hydrazido-(2–)N-(aminoimido) complexes: the addition of acids to dinitrogen complexes. *J. Chem. Soc., Dalton Trans.* 2074-2082 (1974).

36. Marcus, R. A., Sutin, N. Electron transfers in chemistry and biology *Biochim. Biophys. Acta* **811**, 265-322 (1985)
37. Caldin, E. F. Tunneling in proton-transfer reactions in solution. *Chem. Rev.* **69**, 135-156 (1969)
38. Bell, R. P. The Proton in Chemistry; Cornell University Press: Ithaca, NY, 1973.